Modeling Electrical Properties of Neural Tissue Using a Cellular Composite Approach

Omid Monfared

Submitted in total fulfilment of the requirements of the degree of

Doctor of Philosophy

Department of Electrical and Electronic Engineering
THE UNIVERSITY OF MELBOURNE

June 2017

Abstract

THIS research develops a framework for modeling the electrical properties of neural tissue based on its cellular constituents. This has application to modeling of electrical stimulation of neural tissue, including for therapeutic purposes. It also has application to the modeling and interpretation of intrinsic electrical signals in the brain such as spiking, multi-unit activity, local field potential and electroencephalogram (EEG). Standard volume conductor models of neural tissue approximate the electrical properties of tissue with a locally homogeneous conductivity. This is despite the fact that realistic neural tissue is composed of cells with different geometries, orientations and electrical properties. The framework presented here suggests that these cellular level properties have a profound effect on the bulk electrical properties of tissue that cannot be captured by a simple conductivity. The membrane lipid bilayer structure behaves as a capacitance that relates the applied current density to the extracellular potential at previous times. Also, the cells within tissue are tightly packed causing higher resistance in the extracellular space compared with the wider intracellular space, which creates different current paths for the passage of electrical current flow in these spaces.

In this mathematical and computational study, we replace the conductivity of tissue in the standard volume conductor approach with an admittivity which depends on spatial and temporal frequencies. Our expressions for bulk tissue admittivity, are derived from single cell properties by using a mean-field approach. The temporal frequency dependence arises through the capacitance of the membrane lipid bilayer and is related to the membrane time constant. The spatial frequency arises due to the passage of current from the highly confined extracellular space into the less confined intracellular space of a neuron and is related to the electrotonic length constant of neurites.

Expressions for the admittivity are calculated for tissue consisting of a variety of morphological cell types. These include fiber bundles, layered structures in which the dendrites are confined to a plane and tissue composed of cells with a stellate morphology. Finally, these morphological types are combined in model of cortical grey matter that include the effect of glia as well as neurons on the tissue admittivity.

The results show that the effective admittivity changes depending on whether tissue is in the near-, intermediate- or far-field regions relative to a stimulating electrode. The definition of the limits of these regions depends on both spatial and temporal frequencies being applied. The magnitude of the admittivity is smaller in the near-field than the far-field. It is also shown how anisotropic tissue responds to the electrical stimulation depending on the distance of fibers from an electrode. Anisotropic behavior is more prevalent in the far-field region compared to the near-field range in cases where the distribution of fiber orientations shows a bias. The effect of pulse width on tissue response is also investigated and our results demonstrate that for longer pulse widths the transition between near-field to far-field is displaced away from the electrode compared to shorter pulse widths. These results are all explained in details in Chapters 3 and 4 of the thesis. The glia influence on shaping the admittivity response of tissue based on their population is considered in Chapter 5.

The new, more realistic model will facilitate a more accurate application of electrical stimulation to any neural tissue and specifically the brain. More accurate stimulation will improve emerging neurological therapies, such as deep brain stimulation for epilepsy and Parkinson's disease.

Declaration

This is to certify that

1. the thesis comprises only my original work towards the PhD,
2. due acknowledgement has been made in the text to all other material used,
3. the thesis is less than 100,000 words in length, exclusive of tables, maps, bibliographies and appendices.

Omid Monfared, June 2017

Acknowledgements

First and foremost, I would like to express my sincere gratitude to my supervisor Dr. Hamish Meffin for the continuous support of my Ph.D. study and related research, for his patience, motivation, and immense knowledge. His guidance helped me in all the time of research and writing of this thesis.

Besides my supervisor, I would like to thank the rest of my thesis committee: Prof. David Grayden, Prof. Dragan Nesic, and Dr. Dean Freestone, for their insightful comments and encouragement, but also for the hard questions which motivated me to widen my research from various perspectives. My sincere thanks also goes to Dr. Bahman Tahayori for his unlimited support and contribution throughout this project.

I thank my fellow colleagues in electrical engineering department for the stimulating discussions, for the sleepless nights we were working together before deadlines, and for all the fun we have had in the last four years.

I gratefully acknowledge the funding sources that made my Ph.D. work possible. I was funded by National ICT Australia (NICTA) for four years.

Last but not the least, I would like to thank my family: my parents, my brother and my grandmother for supporting me unconditionally throughout my Ph.D. and my life in general.

To my parents, my brother and my grandmother

Contents

List of Figures

List of Tables

Chapter 1
Introduction

THE brain, as a part of the central nervous system, plays an important role in our everyday activities. From reaction to sensory inputs, such as visual and auditory stimuli, to perception and thought or controlling our limbs, almost every activity requires an involvement of the brain. However, if some of these functions are lost due to structural changes, such as a death of cells due to disease, or signaling miscommunication as a result of neurological disorders, such as epilepsy, a burden is put on the life of an individual. The brain is electrically active tissue and passes electrical signals between its constituent neurons. We can record a variety of electrical signals to obtain information from the brain and electrically stimulate to affect brain activity. Therefore, understanding the bulk electrical properties of brain tissue is important. Artificial electrical stimulation attempts to partially restore the lost functions of cells in neural tissue or provide treatment to disabling neurological symptoms. Models of electrical stimulation provide a better understanding of the underlying mechanism of nerve excitation and the effect of stimulating parameters on the neural response. In this thesis, we have studied the macroscopic electrical properties of tissue based on the microscopic cellular constituents.

1.1 Motivation

Neuroprosthetic devices and the intrinsic signals of the brain operate over a range of spatial and temporal frequency ranges. The temporal frequency of electrical stimulation is usually over 1 kHz whereas the intrinsic signals of the brain such as alpha, beta, gamma activities, etc operate on temporal frequency ranges of smaller than 1 kHz. The spatial

frequency range of electrical stimulation is usually less than 1 cycle $/\mu$m. This is while the spatial frequency for the brain structures can extend up to 500 cycles $/\mu$m. Classical models of brain tissue trivialize this by assuming a simple conductivity that has no spatial or temporal frequency dependence. Neural tissues contain microscopic inhomogeneities such as extremely confined extracellular space (around 50 nm) and high impedance membrane that affect the spatiotemporal pattern of electrical stimulation. This thesis will build on the recent theoretical results, that imply that the microscopic cellular structure of neural tissue imbues with admittivity that has spatial and temporal frequency dependence. It is built on theoretical approaches to elucidate the form and consequences of that spatial and temporal frequency dependence.

As mentioned, neuroprosthetic devices work over a range of spatial and temporal frequencies. The spatial frequency range is dictated by the spacing between the electrodes in an electrode array. The temporal frequency depends on the applied pulse-width and temporal pattern of the input signal, i.e., a monophasic or a biphasic pulse. These devices are designed to substitute sensory or motor disability. Examples include cochlear implants or bionic eye devices [Kasi et al., 2011, Tombran-Tink et al., 2007, Martins and Sousa, 2009, Clark, 2006, Niparko, 2009, Shepherd et al., 2013] or deep brain stimulation for treatment of epileptic seizure or Parkinson's disease [Benabid, 2003, Montgomery Jr, 2010]. The bionic devices contain an array of electrodes to activate neural cells in tissue. A good model of electrical stimulation improves our understanding of electrical stimulation parameters and their effects on tissue response. However, standard models of electrical stimulation consider a simplistic assumption that tissue is purely conductive, thus ignoring the microscopic cellular composition of tissue. This can be problematic as the extracellular electrical stimulation works over different ranges of temporal and spatial frequencies. In addition to the external electrical stimulation, there are intrinsic electrical signals in the brain with variety of spatial and temporal characterization. Therefore, understanding spatiotemporal frequency-dependent tissue admittivity will aid in understanding and interpreting these signals.

An example of where models of electrical stimulation are beginning to be employed to improve neural prostheses is neural control engineering. Control engineering aims to

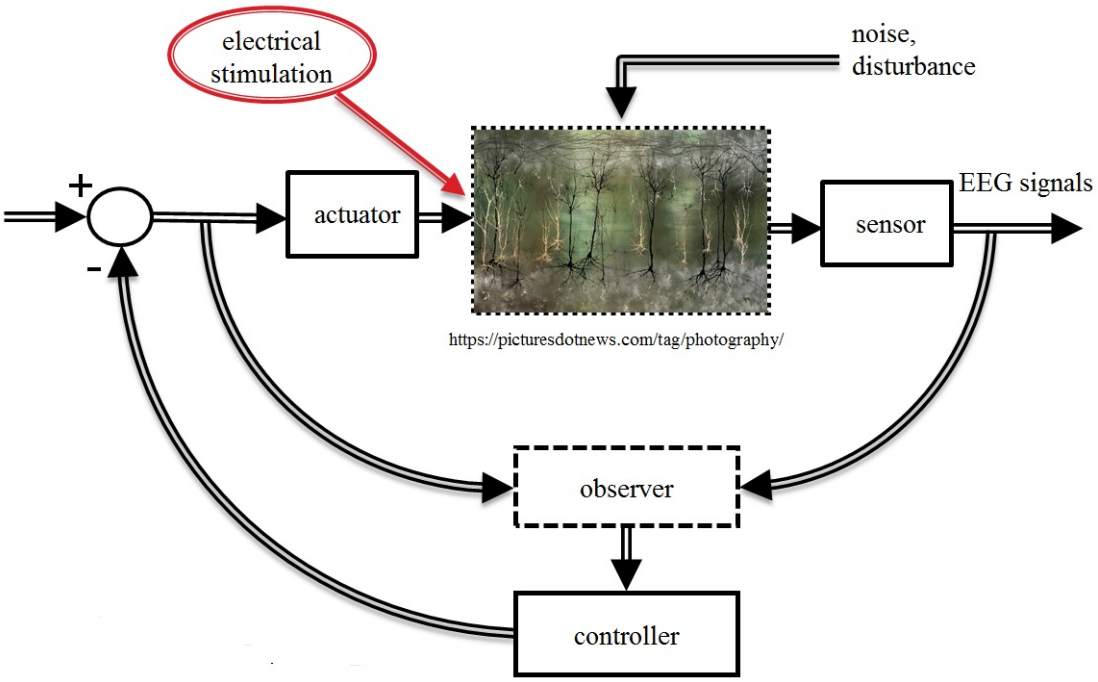

Figure 1.1: Closed-loop control strategy.

manipulate physical systems in order to force them to behave in a particular way. Neural control engineering takes advantage of control strategies to control or treat epileptic seizures or Parkinson's disease [Schiff, 2012]. Figure 1.1 summarizes a closed-loop control strategy and provides a better picture of how important a mathematical model is for control purposes. In Figure 1.1, our proposed model positions between the sensor and actuator. The closed-loop control strategy works by continuously measuring the EEG signals from the brain through the sensors. Based on these data and the measured input signals, which are electrical pulses, the parameters of the model are tuned for each patient [Nelson et al., 2011]. The controller unit receives the output measurements and as soon as any abnormality occurs, a control signal will be passed to the input electrical pulse and a correction signal will be applied to the brain through the actuator unit to control the behavior. This summarizes how control engineering tools can be applied in a real life situation.

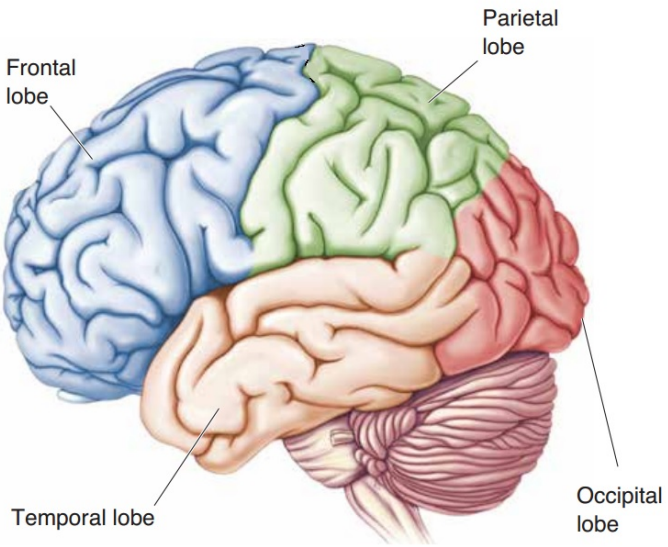

Figure 1.2: The lobes of the human cerebrum [Bear et al., 2015].

1.2 Overview of the Brain and its Cellular Constituents

The brain is the center of the nervous system. It is composed of three main parts: the cerebrum, the cerebellum, and the brain stem. The cerebral cortex is the largest part of the human brain associated with higher brain function, such as interpreting sensory inputs and actions. This structure is divided into specific functional areas called "lobes"; the frontal lobe, the parietal lobe, the occipital lobe and the temporal lobe. This is shown in Figure 1.2. Each of these lobes has been associated with a variety of function-specific tasks. For example, the frontal lobe is associated with reasoning and planning. The parietal lobe is associated with movement and orientation. The occipital lobe is associated with visual processing. The temporal lobe is associated with auditory and visual memories and speech.

The brain is made up of two main classes of cells: neurons and glia. Neurons are the primary units of the central and peripheral nervous system. Morphologically, neurons consist of three regions: cell body (soma), dendrite and axon, as shown in Figure 1.3. The soma is around 20μm diameter and contains the nucleus within which the genetic material exists. Dendrites are branches that extend from the soma and receive signals from

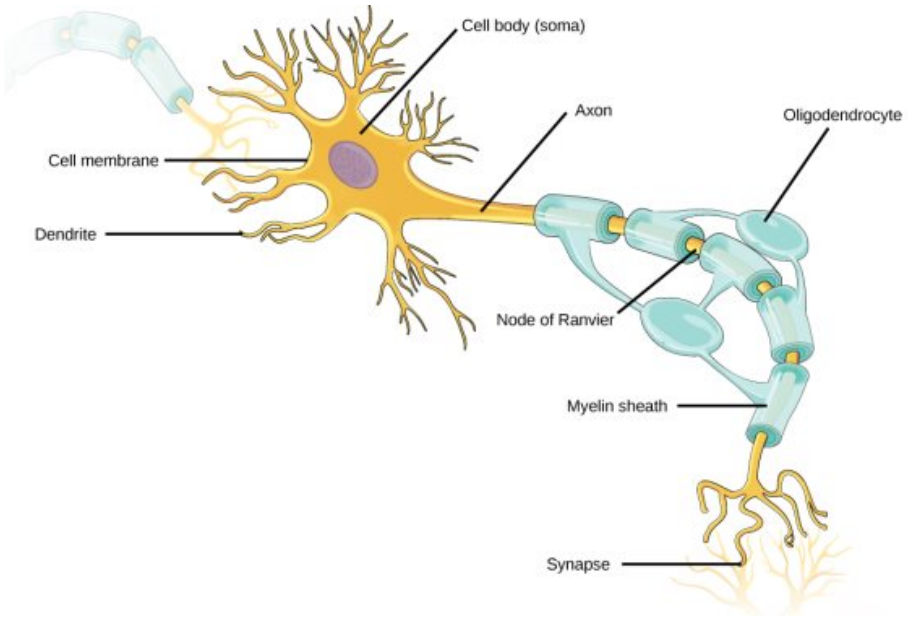

Figure 1.3: Structure of a neuron with myelinated axon. A synapse to a neighboring cell is also shown. www.boundless.com/biology/.

other neurons primarily through some chemical messengers at synapses. There are also gap junctions that make direct electrical contact between cells. The axon is a structure only found in neurons and is specialized for the transfer of information over distances using electrical pulses called action potentials. The axon can extend from less than 1mm to over 1m long [Bear et al., 2015, Kandel et al., 2000]. Most axons are myelinated via a type of glial cell (Oligodendrocyte in Figure 1.3) providing an insulating sheath (myelin sheath) around the axon which results in faster and more reliable nerve impulse. For example, the white matter of the cortex comprises axons that connect regions of the cortex to each other as well as other parts of the brain. There are also many axons in the body that are not myelinated, including axons in the gray matter and the axons of retinal ganglion cells [Kandel et al., 2000]. These cells are unmyelinated to allow the light to reach the photoreceptors without being distorted or scattered. In Figure 1.3, there are some segments between the myelin sheaths which are called nodes of Ranvier. In these gaps, the axon membrane is exposed to the extracellular space. These nodes play an important role in the propagation of neural impulse signals (action potentials) as they are conductive of ions.

Glial cells form connective tissues of the nervous system which play different roles depending on their location. The primary contribution of glia to brain function is supporting neuronal activities [Bear et al., 2015]. Glial cells in the central nervous system outnumber neurons [Herculano-Houzel, 2014]. Some of their roles include

- nutrition delivery to neurons,
- ionic regulation of the extracellular fluid,
- supporting synapses,
- removing toxic material and dead cells,
- provide insulation (myelin sheath).

Other roles of glial cells include immune response [Milligan and Watkins, 2009] and more recently thought to have a role in signaling [Bear et al., 2015].

In the following sections, we will occasionally use the term neurite which refers to any projection from the cell body. This could be either an axon or a dendrite of a cell.

Our account of tissue admittivity based on cellular constituents will incorporate two main aspects: cellular morphology and passive electrical properties of the membrane. These will be explained in details in the following sections. Throughout this thesis, we will use the cerebral cortex as an example of neural tissue to explain the concepts but the modeling framework is not restricted to this.

1.2.1 Morphology of the Main Cellular Subtypes

The cortical gray matter is made up of a variety of neuronal and glial cell types. The unmyelinated axons, neuronal cell bodies, glial cells, and capillaries form the gray matter of the cortex. According to Markram et al. [2015], there are 55 different neuronal morphologies in the cortex. These do not include the various morphologies for glial cells. Their classification was based on the location of the soma and their anatomical and electrical features. The most common type of neurons is the pyramidal cell which is excitatory and is shown in Figure 1.4 a. Pyramidal cells have a cone-shaped cell body with one large dendrite at the apex reaching toward the cortical surface (an apical dendrite)

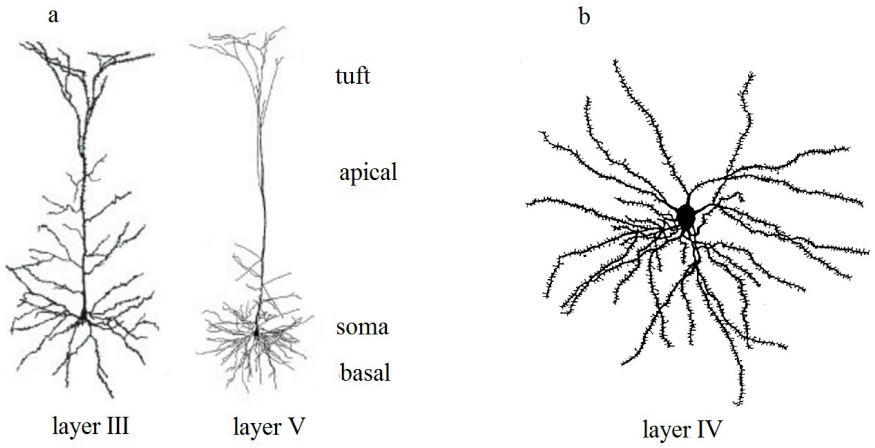

Figure 1.4: Examples of excitatory cells in the cortex. a) Pyramidal cells in different layers of cortex. b) Stellate in layer IV [White and Keller, 1989].

and can be tufted or untufted. Other dendrites that radiate from the base of the soma are called basal dendrites. Pyramidal cell axons originate from the base of the cone and project to the white matter and branch out to nearby cortex [White and Keller, 1989]. Another common neuronal morphological subtype is stellate, which has a star-like shape and is excitatory. These cells have an apical dendrite with one or a few branches with a radial length similar to basal dendrites, Figure 1.4 b.

Inhibitory cells constitute around 20 percent of cortical neurons. Their function varies according to the arrangement of their axons and dendrites. For instance, basket cells send axon terminals to the bodies of pyramidal and stellate cells, whereas the chandelier cells give rise to processes that wrap around the initial segment of pyramidal cell axons. These cells are shown in Figure 1.5.

Neuroglia cells can be categorized as follows.

Astrocytes: These are the most numerous glia in the brain. Their main role is to regulate the chemical content of the extracellular space. Their morphology is similar to basal dendrites or stellate cells. Figure 1.6 contains an astrocyte cell with its connection to other cells.

Oligodendrocytes and Schwann cells: These cells provide a layer of membrane that isolates axons which are called a myelin sheath, as depicted in Figures 1.3 and 1.6. The

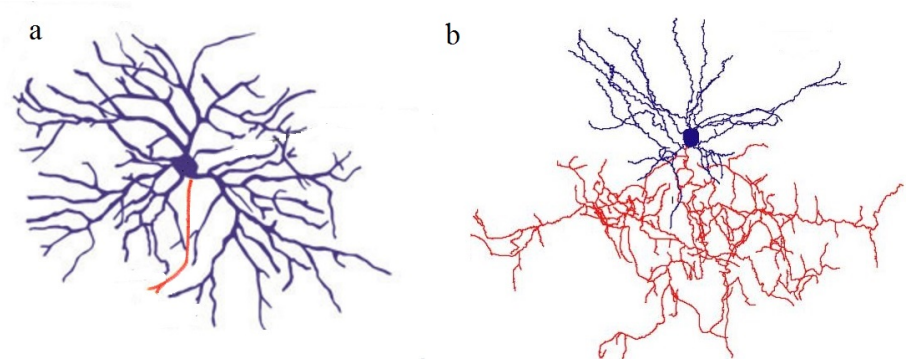

Figure 1.5: Examples of inhibitory cells in the cortex. a) Basket cell with single axon shown in red b) Chandelier cell with red color being the axon arbor [White and Keller, 1989].

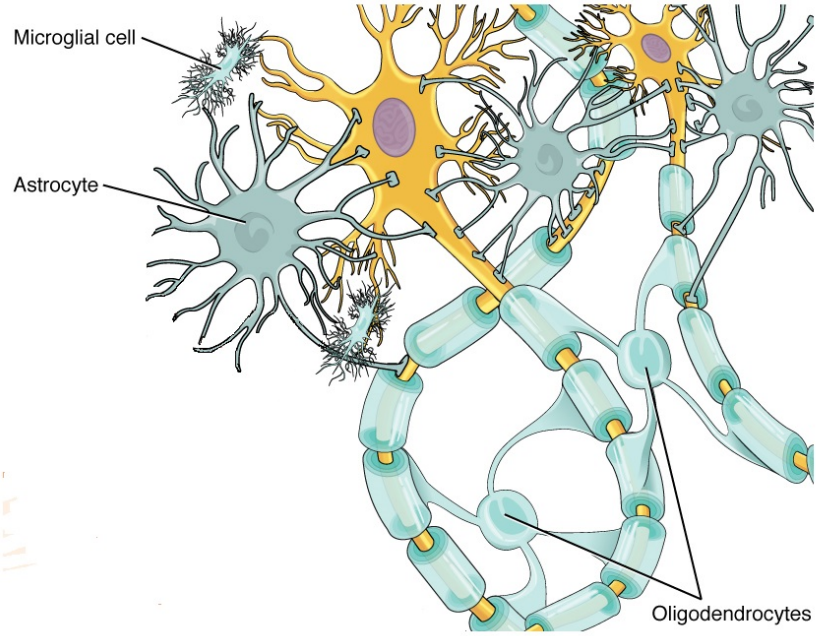

Figure 1.6: Glial cell. Astrocytes and microglia cells have a similar morphology to stellate cells. Oligodendrocytes provide myelin sheath around axons. www.boundless.com.

myelin sheath serves to speed the propagation of nerve impulses down the axon.

Microglia: The main role of these cells is to remove debris left by dead or degenerating neurons and glia. The morphology of these cells is similar to astrocytes, as shown in Figure 1.6.

Neurons and glial cells are organized in a laminar structure in the cortex. Six layers are generally recognized in the neocortex (if excepting the olfactory cortex). These layers are labeled from the surface layer to the deep layer close to the white matter as I to VI. The list of the layers and their cell types are as follows.

Layer I This is a molecular layer which provides feedback connections between cortical areas as it contains apical dendrites of pyramidal neurons and many axon terminations.

Layers II and III These layers mainly contain small pyramidal cells, some inhibitory neurons (bipolar and double bouquet cells), and apical dendrites of pyramidal cells of layers V and VI.

Layer IV This layer is the principal recipient of input from the thalamus. Neurons in this layer, which include spiny stellate and a variety of inhibitory cells are strongly coupled. The output of this layer projects to the superficial layers.

Layers V and VI. The majority of the cells in this layer are large pyramidal cells that project axons to the thalamus and the white matter. There are also a few inhibitory cells such as Chandelier cells and Martinotti cells. Martinotti cells make long axonal projections across all layers of neocortex while Chandelier cells synapse to the axon initial segment of the pyramidal cells.

1.2.2 Electrical Properties of the Cell Subtypes

Cells have a lipid bilayer membrane that controls the exchange of ions between the inside and the outside of the cell. The lipid bilayer, shown in Figure 1.7, provides a good insulating layer that has very high impedance while being sufficiently thin so as to have considerable capacitance (1 μF.cm^{-2}). At rest, there is an excessive concentration of positive charges on the outside and an excessive concentration of negative charges on the

inside. The unequal distribution of positively charged ions (such as Na^+ and K^+) on either side of the membrane is established by Na^+-K^+ pumps. Apart from this, electrically charged ions can cross the membrane through specialized channels, namely ion channels. Various ion channels respond to different stimuli to open/close in order to allow the passage of specific ions. The stimuli may be an electrical signal that activates those voltage-gated ion channels, or can be a chemical binding to activate ligand-gated ion channels. There are also passive leak channels that allow passage of ions without stimulation. Comparing neuron and glia membrane, it is found that glial cell membrane is leakier than the nerve cell membrane [Trachtenberg and Pollen, 1970]. In other words, glia membrane has smaller resistance and conducts more ions compared to neuron membrane. The membrane time constant of a glial cell is between $217\mu s - 630\mu s$ which is on average less than one-twentieth of neuron time constant [Trachtenberg and Pollen, 1970]. The measured specific resistance of glia cell membranes is very low which is consistent with the observation that these cell bodies are more conductive compared to neurons. Also, in terms of size glia cells are smaller around $10\mu m$ in diameter in contrast with $30\mu m - 40\mu m$ for neurons [Alvarez-Maubecin et al., 2000]. All these differences lead to different responses over various spatial and temporal frequency ranges for glia and neurons.

1.3 Mechanism of Excitation of the Neurons (Synaptic Excitation)

Excitation of neurons occurs through their membranes. The membrane properties are modeled by electrical elements (e.g. the work by Hodgkin and Huxley, which will be explained shortly). For instance, the lipid bilayer membrane offers properties similar to a passive capacitance as it provides an insulation layer with very high resistance that maintains charge separation across its boundaries (capacitance definition is $C = Q/V$ where Q is charge separation and V is the voltage difference). The resting ion channels, however, causes leakage of ions across the membrane which is modeled by a linear, passive conductance. Finally, the effect of voltage-gated and ligand-gated ion channels are

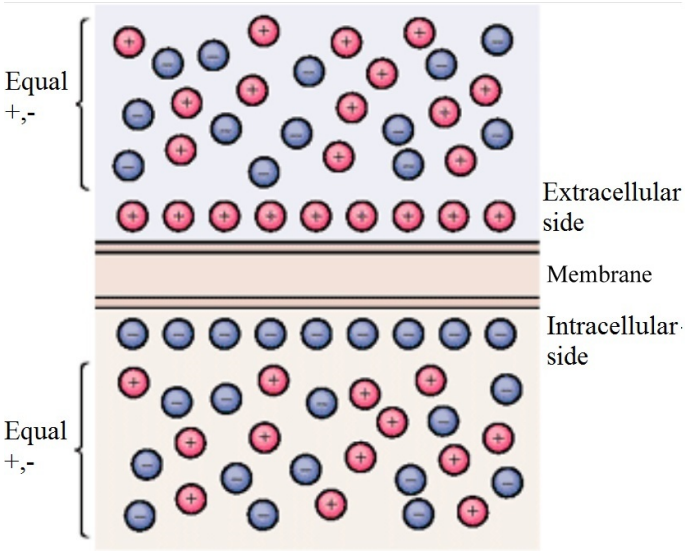

Figure 1.7: Charge separation across the lipid bilayer membrane. When the membrane is at rest there is an equal amount of positive (cation) and negative (anion) ions [Kandel et al., 2000].

modeled by nonlinear conductance elements. This is shown in Figure 1.8.

The membrane potential is defined as

$$V_{\mathrm{m}} = V_{\mathrm{in}} - V_{\mathrm{out}}, \tag{1.1}$$

where V_{in} is the potential inside and V_{out} is the potential outside the cell. The membrane potential at rest is typically in the range of -60mV to -70mV, and is called the resting membrane potential.

The dynamical behavior of a neuron depends on the change in the membrane potential. If the voltage difference across the membrane reaches a threshold, a neuron produces an action potential. This phenomenon happens when the current flow into and out of the cell disturbs from its resting state [Kandel et al., 2000].

An input signal, such as a synaptic potential to the cell, causes a flow of ions into or out of the cell. This leads to a disturbance in charge distribution, and hence, the membrane potential is altered. Depolarization, shown in Figure 1.9, occurs if the charge separation changes the membrane potential from negative to positive (or less negative). Conversely, if the membrane potential drops to a more negative value the neuron goes to

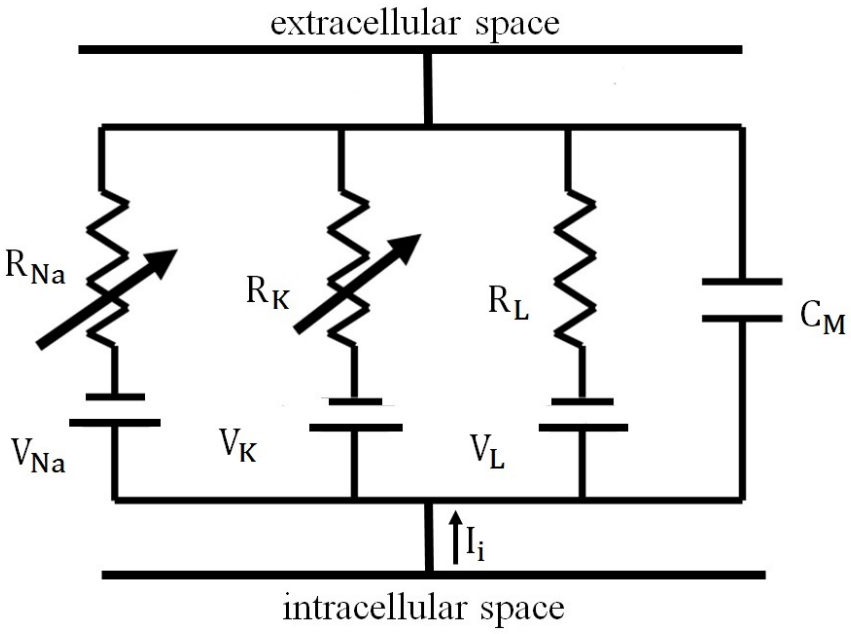

Figure 1.8: Hodgkin and Huxley model of the membrane. C_M is the membrane capacitance per unit area, R_L is the leak resistance per unit area. R_{Na} and R_K are the time-dependent resistances as a model of voltage-gated sodium and potassium channels respectively.

a hyperpolarized state.

The natural process to transfer information in the nervous system is through an all-or-none event called action potentials. An action potential is the dynamics of the electrical behavior of the membrane that occurs by a flow of ions through voltage-gated channels. During this process the membrane potential reaches a depolarization threshold, around -55 mV and rapidly increases. During an action potential, sodium ion channels open and sodium ions enter the cell (depolarization state). In the meantime, the potassium channels also open to permit the exit of potassium ions from inside the cell. At the peak of the action potential, sodium channels inactivate while the potassium channels remain open and potassium ions continue to leave the cell. The outflow of the potassium ions decreases the membrane potential further (hyperpolarization state) Figure 1.9. After-hyperpolarization, which last for a few milliseconds, occurs after an action potential and reduces the ability of a neuron to generate another action potential. The refractory pe-

riod is the period when voltage-gated Na channels are deactivated and typically lasts for about 1 ms.

Note that this section lacks some of the minute details on the process that we do not elaborate on because they are not particularly relevant to the thesis.

The underlying ionic process in the generation of an action potential was first described by the Hodgkin and Huxley (HH) model. They modeled the process involved in the excitation of nerve fiber through an electrical circuit shown in Figure 1.8.

The equation describing Figure 1.8 is the Kirchhoff's current law

$$\begin{aligned} I_{\mathrm{m}} =& C_M \frac{dV_{\mathrm{m}}}{dt} + I_i \\ =& C_M \frac{dV_{\mathrm{m}}}{dt} + I_{\mathrm{Na}} + I_{\mathrm{K}} + I_{\mathrm{L}} \\ =& C_M \frac{dV_{\mathrm{m}}}{dt} + g_{\mathrm{Na}}(V_{\mathrm{m}} - V_{\mathrm{Na}}) + g_{\mathrm{K}}(V_{\mathrm{m}} - V_{\mathrm{K}}) + g_{\mathrm{L}}(V_{\mathrm{m}} - V_{\mathrm{L}}), \end{aligned} \tag{1.2}$$

where I_{m} and I_i are the total membrane and the ionic current density respectively. C_M is a passive property of the membrane corresponding to the capacity per unit area. g_{Na} and g_{K} are the sodium and potassium conductances per unit area, respectively. V_{Na} and V_{K} are the sodium and potassium reversal potentials, respectively, and g_{L} and V_{L} are the leak conductance per unit area and leak reversal potential, respectively [Hodgkin and Huxley, 1952].

This model describes the qualitative relationship between the current and voltage of a piece of a membrane over time. The whole propagating process of nerve signals is only possible because the conductance of the membrane to ionic currents caused by sodium and potassium ions depends essentially on the voltage-gated ion channels.

1.4 Mechanism of Electrical Stimulation of Neurons

External electrical stimulation is done by placing an electrode in or around neural tissue and applying a current or voltage to induce the flow of ions in tissue to set up an electrical potential, Figure 1.10. Typically, this is a biphasic pulse with a pulse duration in the range of 10 μs - 1000 μs. Electrical stimulation sets up an extracellular potential dif-

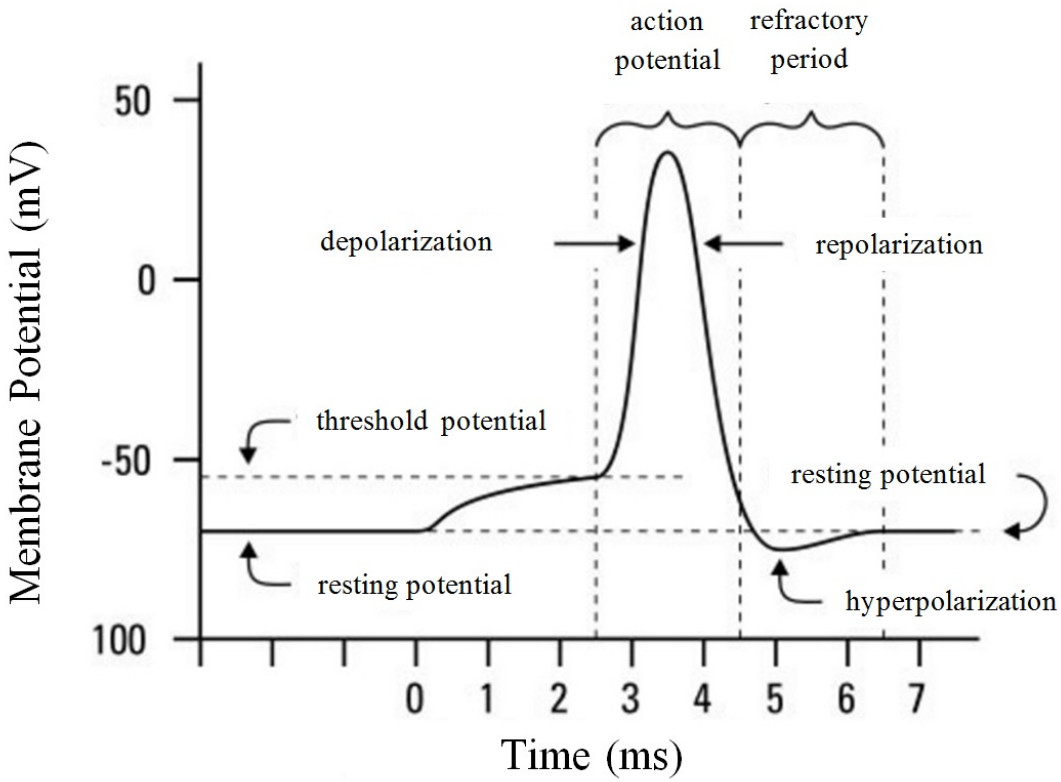

Figure 1.9: Diagram of an action potential. Source: www.dummies.com.

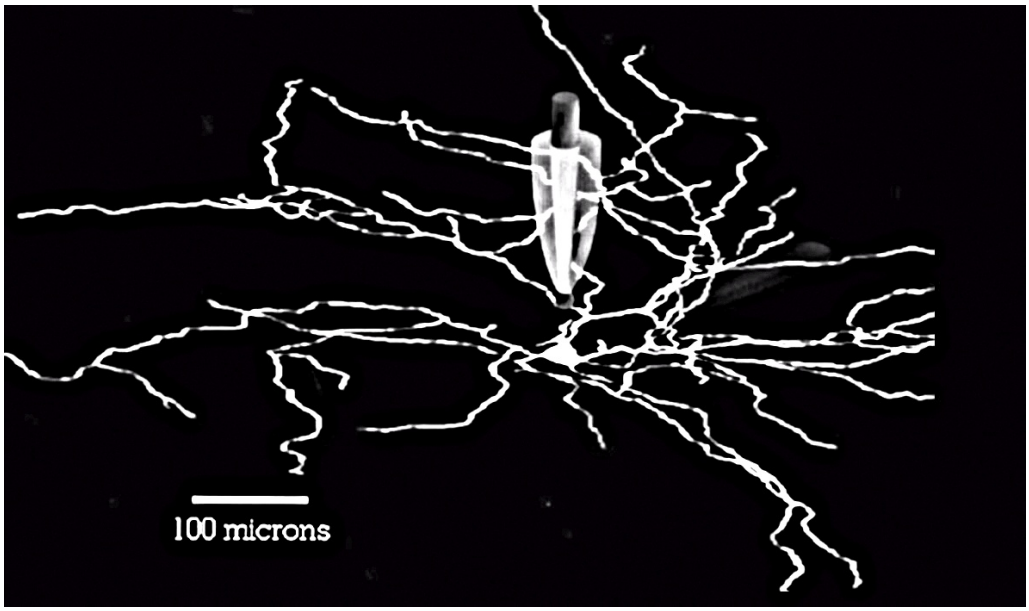

Figure 1.10: Electrical stimulation configuration [Greenberg et al., 1999].

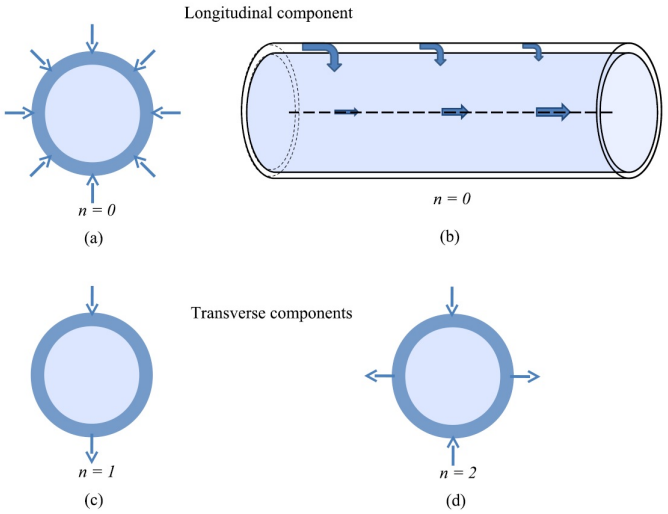

Figure 1.11: Different modes of stimulation characterized by an integer, n. (a) $n = 0$ corresponds to the rotationally symmetric component of the field. (b) Three-dimensional view of the longitudinal mode of stimulation. (c) Transverse component for n = 1. (d) Transverse component for n = 2. Photo is taken from [Meffin et al., 2012].

ference which depolarizes the membrane. The depolarization either occurs by an inward current flow along the neurite axis or flow of current across the neurite. These pathways are known as the longitudinal and transverse modes of stimulation, respectively and are shown in Figure 1.11. This depolarization causes voltage-gated sodium channels to open and depolarize the membrane. Models of electrical stimulation of neural tissue look at the fundamental mechanism of excitation of neurons, in a distance from an electrode with certain polarity and pulse-width. Electrical stimulation affects cells differently based on their geometry and orientation with respect to the electrode. In addition, different parts of the brain, such as gray matter, white matter, and cerebrospinal fluid, have different electrical properties that can influence the current flow pattern in different areas. As explained earlier in this section, stimulating neural tissue usually leads to excitation of different modes of stimulation. The dominance of each mode relies on the orientation of axon and cell body with respect to the stimulating source. For example, Ranck [1975] explains that, for an axon, the component of voltage along its main axis is more important and probably more dominant. These parameters differentiate the mechanism of excitation with electrical stimulation from synaptic stimulation. The synaptic input mechanism of excitation has been studied very well for a long time [Wilson and

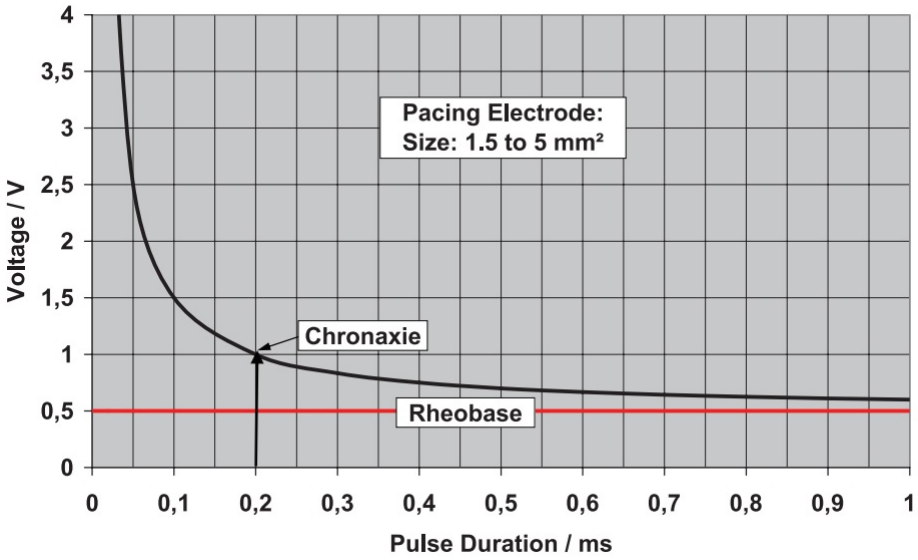

Figure 1.12: A strength-duration curve [Irnich, 2010].

Cowan, 1972, Zetterberg, 1973, Jansen and Rit, 1995]. However, despite a good body of research on electrical stimulation modeling [McNeal, 1976, Rattay, 1986, Rattay, 1989, Altman and Plonsey, 1988], work needs to be done to improve their outcome. These models are fundamental to the operation of neuroprosthetic devices such as cardiac pace makers, cochlear implants, some prosthetics limbs, bionic eyes, and deep brain stimulation for the treatment of Parkinson's disease or epilepsy. What we are going to do, that sets our work apart from others, is a more accurate modeling of tissue admittivity to better predict changes in the extracellular potential, which influences membrane excitability.

1.5 Basics of Electrical Stimulation in Experiments

There have been many experimental studies [Nowak and Bullier, 1996, Histed et al., 2009, Ozen et al., 2010, Anastassiou et al., 2010, Joucla and Yvert, 2012] alongside the theoretical work introduced earlier aimed at understanding the effect of electrical stimulation on neurons. One of the major analyses in these studies rests on strength-duration curves. A strength-duration curve, as shown in Figure 1.12, is one of the measures that show the effect of stimulus strength and duration on the threshold for activation of a neuron. In order to compare the effects of different stimuli through the strength-duration curves, the

terms rheobase and chronaxie are used. Rheobase is the minimum current amplitude of infinite duration that is required to excite a neuron. Chronaxie is the duration of a current pulse that gives double the stimulus strength of the rheobase. These characteristics are influenced by physical and physiological parameters [Irnich, 1980].

Note the strength and duration variables are inversely related. This means a stronger current requires less duration to stimulate the cell and vice versa [Boinagrov et al., 2010].

Chapter 2

Models of Electrical Stimulation of Neural Tissue

THIS chapter includes two sections. The first section provides an overview of the studies necessary to introduce a relevant background on existing models of electrical stimulation. In the second section, detailed mathematical description of two significant models, the volume conductor and the cellular composite models, that are central to the work of this thesis will be given.

2.1 Literature Review

Mathematical modeling of electrical stimulation has received considerable of attention in recent years. Two common approaches in modeling extracellular electrical stimulation are: 1. volume conductor models and 2. bidomain models. In what follows both modeling approaches are reviewed.

Volume Conductor Models

The volume conduction model describes the transmission of an electric field from an electric source through biological tissues. The modeling process can be broken down into the calculation of the extracellular potential due to a set of electrodes at one step and application of that result to calculate the membrane potential in a second step. The second step itself i.e., modeling the membrane potential, can be divided into two different categories. The studies that considered depolarization of the membrane along the fiber length [Mc-

Neal, 1976,Rattay, 1986,Ganapathy and Clark, 1987,Rattay, 1999,Coburn, 1988,Greenberg et al., 1999, Tuckwell, 1988, Reilly and Diamant, 2011]; and those that considered depolarization through the component of the applied field that is perpendicular to the fiber axis [Boinagrov et al., 2010, Krassowska and Neu, 1994, Pavlin et al., 2002, Palanker et al., 2005, Pourtaheri et al., 2009, Wenger et al., 2011, Wongsarnpigoon and Grill, 2012].

Extracellular Potential

In modeling the extracellular potential, many studies [McNeal, 1976, Rattay, 1986, Rattay, 1989] have considered the simple case of a point source electrode in an isotropic medium for the first step

$$V_{\mathrm{e}} = \frac{I}{4\pi\sigma R} \tag{2.1}$$

where I is the injected current, R is the distance from the electrode and σ is the conductivity of the extracellular space. However, more complex models have also been considered [Bossetti et al., 2007].

Membrane Potential Modeling: Longitudinal Mode

To model the membrane potential, many authors based their modeling on the neuronal cable equation [McNeal, 1976, Rattay, 1986, Schnabel and Struijk, 2001]. This equation is a partial differential equation that describes the spatiotemporal distribution of membrane voltage along the nerve fiber. This corresponds to the longitudinal mode of stimulation as the inward current causes depolarization at one point and hyperpolarizes the fiber further down through an outward current.

One of the seminal contributions in this regard is McNeal's model of excitation of a myelinated nerve fiber [McNeal, 1976]. The model involves a distributed resistor-capacitor (RC) circuit as represented in Figure 2.1. This figure shows a fiber membrane model through capacitors, C_m, conductors, G_m and resting potential voltage sources, V_r. Since this is a myelinated fiber model the internodal conductances, G_a were also considered to model the resistance for nodes of Ranvier.

McNeal's model assumes that the fiber is in an isotropic medium, is infinitely long,

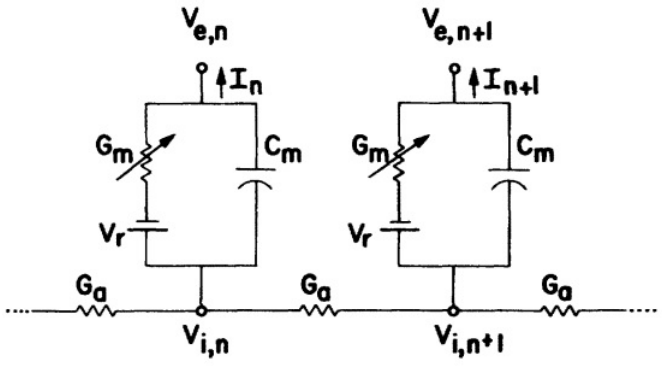

Figure 2.1: McNeal's electrical circuit modeling of a myelinated nerve fiber, McNeal [1976].

and has regularly spaced nodes. These nodes either represent the nodes of Ranvier for a myelinated fiber or arbitrary points on an unmyelinated fiber. It also assumes that the fiber does not distort the external electrical field. Based on these assumptions, the current across the membrane at node n was described as

$$C_m \frac{dV_n}{dt} + I_{i,n} = G_a(V_{i,n-1} - 2V_{i,n} + V_{i,n+1}), \tag{2.2}$$

which is essentially the Kirchhoff's current law (KCL) at node n. In this equation, V_n is the membrane potential minus the resting potential, $V_{i,n}$ is the intracellular potential at node n and $V_{e,n}$ is the extracellular potential at node n. C_m and G_a are the nodal capacitance and axial internodal conductance, respectively.

In a subthreshold regime prior to the excitation via voltage-gated ion channels, the membrane passive conductance is constant. Therefore,

$$I_{i,n} = G_m V_n, \tag{2.3}$$

where G_m is the membrane conductance and represented as

$$G_m = g_m \pi d l, \tag{2.4}$$

in which g_m is the membrane conductance per unit area, d is the axon diameter and l is

the nodal gap width.

Replacing equations (2.3) and (2.4) into equation (2.2) gives an infinite set of first order differential equation

$$\begin{aligned} \frac{dV_n}{dt} &= \frac{1}{C_m}\left[G_a(V_{n-1} - 2V_n + V_{n+1} + V_{e,n-1} - 2V_{e,n} + V_{e,n+1}) - G_m V_n\right], \\ n &= \ldots, -2, -1, 0, 1, 2, \ldots, \end{aligned} \tag{2.5}$$

where $V_n = V_{i,n} - V_{e,n} - V_r$ and the initial conditions are all $V_n(0) = 0$ (if the neuron is assumed to be at rest). This is due to the capacitance shunting each node.

McNeal calculated V_n assuming an applied extracellular field and initial conditions.

Following McNeal's model, Rattay [1986] developed a model of discretized axon. Rattay defined the ionic current using the Hodgkin-Huxley model (presented in Chapter 1, equation (1.2))

$$I_i = i_{Na} + i_K + i_L, \tag{2.6}$$

which contains sodium, potassium and leakage currents. The internodal conductance is defined as $G_a = \dfrac{\pi d^2}{4\rho_i \Delta x}$, where ρ_i is the intracellular resistivity and Δx is the internodal distance.

Substituting equation (2.6) and G_a into equation (2.2) leads to

$$\begin{aligned} \frac{dV_n}{dt} = \frac{1}{c_m}\Bigg[\frac{d}{4\rho_i}\left(\frac{V_{n-1} - 2V_n + V_{n+1}}{\Delta x^2} + \frac{V_{e,n-1} - 2V_{e,n} + V_{e,n+1}}{\Delta x^2}\right) \\ - (i_{Na} + i_K + i_L)_n\Bigg], \end{aligned} \tag{2.7}$$

where $c_m = \dfrac{C_m}{\pi d \Delta x}$ is the capacitance per cm^2.

Equation (2.7) describes a time-dependent behavior of an unmyelinated axon in an electrical field or more specifically discretized model of the cable equation. The equation for myelinated axon was also derived in a similar fashion by Rattay [1986]. The main contribution of Rattay [1986] was an introduction of the concept of an activating function. The activating function is the second derivative of the external potential in the direction of the axon. This term is responsible for the activation of the fiber using the extracellular

stimulation [Rattay, 1986, Rattay, 1989] and is defined as

$$f_n(t) = \frac{V_{e,n-1} - 2V_{e,n} + V_{e,n+1}}{\Delta x^2}. \tag{2.8}$$

If $\Delta x^2 \to 0$, then

$$f(x,t) = \frac{\partial^2 V_e}{\partial x^2}, \tag{2.9}$$

where x is the coordinate along the main axis of the fiber. Rattay [1989] also provided that the calculation of the activation function itself can tell a lot about the excitation of the fiber without even solving the equations for the extracellular potential.

Rattay also used the model of activation functions to investigate the influence of multiple point source electrodes on tissue and the effect of parameters, such as fiber diameter and distance from the source. The 1989 work was then extended to multi-compartmental neuron models [Rattay, 1999]. In the multi-compartmental model, a neuron is divided into different segments. Each segment responds differently to stimulation with some parts, such as axons, being highly excitable and other parts, such as soma, being comparatively hard to excite. The modeling framework was still very similar to the activation function method presented previously. However, the activation function, in this case, was of a more complex form that had a dependence on each parameter of each compartment.

In a separate effort, Rubinstein and Spelman [1988] developed a passive cable model of an unmyelinated fiber with an arbitrary time-varying external electrical field. This was to identify the excitation location and the tendency to excite as a function of the spatial and temporal frequencies of the applied electric field for an unmyelinated neuron. They took a system approach in which the input was an arbitrary time-varying electrical field and the output was the membrane polarization. The relationship between the input and the output was defined as a system that described the behavior of a passive fiber.

Developed on the basis of McNeal's cable model configuration, [Rubinstein and Spelman, 1988] derived a partial differential equation to describe the whole fiber . Defining the membrane potential as $V_m = V(x,t) - \Psi(x,t)$ with $V(x,t)$ and $\Psi(x,t)$ being the in-

tracellular potential and the applied field, respectively, the following relationships hold

$$\begin{aligned} i_m =& c_m \frac{\partial V_m}{\partial t} + \frac{V_m}{r_m}, \\ \frac{\partial i_a}{\partial x} =& - i_m, \\ \frac{\partial V}{\partial x} =& - i_a r_a, \end{aligned} \tag{2.10}$$

where i_m is the membrane current per unit area (A/cm^2), i_a ia the axial current, $r_m = R_m/2\pi a$, $c_m = 2\pi a C_m$, and $r_a = R_a/\pi a^2$. By combining these equations, the cable equation describing the intracellular potential was derived as

$$-\lambda^2 \frac{\partial^2 V}{\partial x^2} + \tau \frac{\partial V}{\partial t} + V = \tau \frac{\partial \Psi}{\partial t} + \Psi, \tag{2.11}$$

where λ and τ are the space and time constants, respectively. These are defined as $\lambda = \sqrt{r_m/r_a}$ and $\tau = r_m c_m$.

By solving equation (2.11) in the Fourier domain and using the relationship between V and V_m, the membrane potential was calculated using a quasi-static approximation. In this approximation it is assumed that the extracellular space is purely resistive. Through this model, Rubinstein and Spelman [1988] explained the effect of spatial frequencies along the fiber and temporal frequencies of stimuli on the activation of fibers. More specifically, the authors explained that the fibers responding to stimuli with rich high spatial frequencies are less sensitive to increased temporal frequency. This means that increasing the temporal frequency of a stimulus increases the threshold of distant fibers more than the threshold of near fibers. This is because the fiber, when polarized, behaves like a spatial high-pass and temporal low-pass filter of the external electrical stimulation source.

The depolarization was, in general, described by either a discretized or continuous cable equation. In all of the mentioned studies, the modeling processes were based on the assumption that the depolarization occurs as the current travels along the main axis of the fiber. However, as discussed in Chapter 1, current can also cross the fiber in a transverse direction to its axis. This has led some researchers to an alternative modeling

approach for the membrane potential.

Membrane Potential Modeling: Transverse Mode

The second approach in modeling depolarization of the membrane using the volume conductor approach takes into account the transverse current path i.e., the path that is perpendicular to the fiber axis. In this approach, the current that crosses the membrane causes depolarization at one site while the other site hyperpolarizes. There are only a few articles that have provided an equation describing this mode in a similar way to the cable equation. In some ways it may be considered reasonably trivial that the extracellular potential across this fiber is divided across the membrane (like a voltage divider) with no drop across the intracellular space. This is a reasonable approximation in many but not all cases and is addressed in Meffin et al. [2012].

Schnabel and Struijk [2001] described the transverse effect through modifying the cable equation. This was done by appending an extra term to the activation function of Rattay [1986] to account for the electric field that is perpendicular to the fiber axis. The argument was if the extracellular potential is not rotationally symmetric, such as in the case of bipolar stimulation where the transverse component to the nerve fiber is large, the cable equation does not predict an accurate model. Therefore, the cable equation (2.9) was modified to

$$f_m(x) = \frac{\partial^2 V_e}{\partial x^2} + 2bE_\perp, \tag{2.12}$$

where b is the radius of the extracellular space (assuming it has a cylindrical form) and

$$E_\perp = \frac{\partial V_e}{\partial r}|_{r=0}. \tag{2.13}$$

where $r = 0$ is the position of the fiber in a cylindrical coordinates (r, θ, z).

A criticism of this modification is that the transverse stimulation does not depolarize the neurite the same on all sides; but it is a more localized effect at the site of stimulation. In this sense, Schnabel and Struijk [2001] model is very much an ad hoc approximation that has limited physical validity.

There has been a range of opinion about the relative significance of longitudinal and

transverse modes, with many authors arguing that the longitudinal is the most important, and some others assuming that only the transverse needs to be considered. The studies by Schnabel and Struijk [2001] and Livshitz et al. [2002] compared these modes of stimulation. The comparisons were made for a long cylindrical fiber in a homogeneous medium under a point source electrode stimulation. Based on the analytical derivation of the membrane potential for different modes, both studies found that stimulation condition plays a role in predicting which mode is dominant. For example, they found that the longitudinal mode is dominant in an intermediate range of electrode-fiber separation (although the estimated range differed significantly between these studies).

However, these studies had a number of limitations in comparing the relative magnitude of the two modes of stimulation. First, the assumption of homogeneity and isotropy is not realistic as tissue is typically inhomogeneous both on macro and micro scales [Meffin et al., 2012]. This is while Schnabel and Struijk [2001] assumed there is no feedback from the cell onto the electric field. Realistically, neural tissue is composed of tightly packed cells creating an extremely small extracellular space with high resistance and wider intracellular space with low resistance. The current from the extracellular space has to cross a very high impedance membrane (that has capacitance property) in order to access the intracellular space. This current redistribution occurs over a range of spatial scales described by the length constant and causes an anisotropic effect. Second, most of the previous studies (except [Bossetti et al., 2007]) ignored the dynamics of the membrane (i.e., capacitance and voltage-gating ion channels) and treated the membrane as a resistive environment. Thus, did not consider any anisotropy effect.

Bidomain Model

A second approach in modeling electrical stimulation is a bidomain approach which was originally developed to model cardiac tissue [Tung, 1978, Roth and Wikswo, 1994]. The bidomain model is basically a three-dimensional anisotropic cable model. It consists of two regions, the intracellular and the extracellular spaces, defined as continuums on the same set of coordinates (usually in three spatial dimensions). These are shown by resistor grids in Figure 2.2. These regions are separated by a membrane which is also distributed

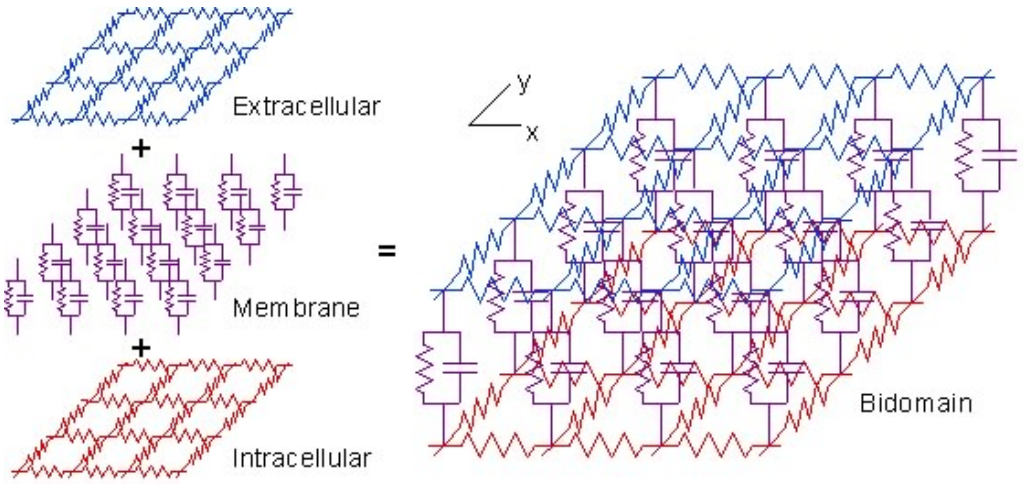

Figure 2.2: Bidomain equivalent electrical circuit. x is the direction of fiber axis and y is perpendicular to the fiber axis.
Source: http://www.scholarpedia.org/article/Bidomain-model.

continuously through the same space and represented by a parallel connection of resistors and capacitors in Figure 2.2. In the bidomain model, tissue microstructure such as cellular geometry is ignored in favor of an averaged property. These models are the result of applying Ohm's law in the intracellular and extracellular domains through the membrane [Altman and Plonsey, 1988, Roth and Wikswo, 1994, Roth, 1991, Meffin et al., 2014]. The relationship between the current density and the potential is given via the following constitutive equations for the intracellular (J_i and V_i) and the extracellular (J_e and V_e) spaces

$$\begin{aligned} J_\mathrm{i} &= -\sigma_\mathrm{i} \nabla V_\mathrm{i}, \\ J_\mathrm{e} &= -\sigma_\mathrm{e} \nabla V_\mathrm{e}, \end{aligned} \tag{2.14}$$

where the conductivities in these spaces are defined, respectively, as

$$\begin{aligned} \sigma_\mathrm{i} &= \begin{bmatrix} 0 & 0 & 0 \\ 0 & 0 & 0 \\ 0 & 0 & \sigma_{\mathrm{i,L}} \end{bmatrix}, \\ \sigma_\mathrm{e} &= \begin{bmatrix} \sigma_{\mathrm{i,T}} & 0 & 0 \\ 0 & \sigma_{\mathrm{i,T}} & 0 \\ 0 & 0 & \sigma_{\mathrm{i,L}} \end{bmatrix}. \end{aligned} \tag{2.15}$$

As can be seen from the matrices (2.15), the effect of the current that would cross the intracellular space is neglected because the nerve and muscle fibers are not connected in this direction [Altman and Plonsey, 1988].

The effective conductivities in the above matrices can be related to the resistivities of the intracellular ρ_{i} and the extracellular ρ_{e} spaces provided $d \ll b$ [Meffin et al., 2014]

$$\begin{aligned} \sigma_{\mathrm{i,L}} &= \frac{1}{\rho_{\mathrm{i}}}, \\ \sigma_{\mathrm{e,L}} &= \frac{2d}{b\rho_{\mathrm{e}}}, \\ \sigma_{\mathrm{e,T}} &= \frac{d}{b\rho_{\mathrm{e}}}. \end{aligned} \tag{2.16}$$

In addition, the conservation of current enforces the current that is lost from one domain to pass through the other domain. Hence, it is required to

$$\begin{aligned} \nabla \cdot J_{\mathrm{i}} &= -J_{\mathrm{m}}, \\ \nabla \cdot J_{\mathrm{e}} &= J_{\mathrm{m}}, \end{aligned} \tag{2.17}$$

where J_{m} is the transmembrane current density per unit volume.

Note that, the bidomain model takes into account the spatiotemporal frequency dependence of the admittivity. This is because it has a spatially extended intracellular and extracellular space separated by an membrane with capacitive and resistive properties. However it has a limited capacity to do this because , they it is difficult apply to situations with crossing fibers. Each different fiber direction requires a new intracellular domain, which become intractable beyond just a few different orientations.

So far we introduced the two main models of electrical stimulation; the two-stage approach called the volume conductor and the bidomain approach. In Meffin et al. [2014], it was proven that these two modeling approaches are mathematically equivalent. Therefore, we continue our study of the literature with the two-stage modeling approach, discuss some of their deficiencies as well as a recent approach to model tissue physical properties more accurately.

As it was described earlier, one of the issues that the volume conductors do not ad-

equately describe is the transverse effect through an equation that uses reduced set of coordinates similar to the cable equation.

The second issue was that the microscale inhomogeneities, such as tightly packed cells, different cell types i.e., neurons and glial cells and the high impedance membrane, were ignored. These inhomogeneities can restrict the extracellular current flow and cannot be described by the volume conductor approach.

Meffin and Tahayori et al. [Meffin et al., 2012, Tahayori et al., 2012, Meffin et al., 2014, Tahayori et al., 2014] recently addressed these limitations in a modeling approach called the cellular composite. This is a two-stage modeling approach that is similar to the volume conductors. The equations describing the cellular composite models will be discussed in the upcoming sections as these are fundamental to this thesis. Apart from that, we will make an in-depth comparison between the cellular composite and the volume conductor models.

2.2 Introduction to Models of Electrical Stimulation

This section reviews the fundamental equations describing the standard volume conductor [McNeal, 1976, Rattay, 1986, Ganapathy and Clark, 1987, Coburn, 1988, Greenberg et al., 1999, Tuckwell, 1988] and the cellular composite models [Meffin et al., 2012, Meffin et al., 2014]. These approaches are used to model extracellular electrical potential of neural tissues though the underlying assumptions of the models differ. While standard volume conductor models treat tissue as a purely conductive and homogeneous medium [Altman and Plonsey, 1988], the cellular composite model considers the microscopic inhomogeneities by replacing the conductivity of tissue with an admittivity that is non-local, non-instantaneous and anisotropic. The non-local effect is the result of the passage of current through the intracellular and the extracellular pathways. The admittivity is non-instantaneous as it models a passive capacitance property of the membrane that relates extracellular current density to the extracellular potential with some delay.

In these modeling approaches, a neurite (an axon or dendrite of a neuron) is approximated by an ideal cylinder with infinite length [Coburn, 1988, Cartee and Plonsey,

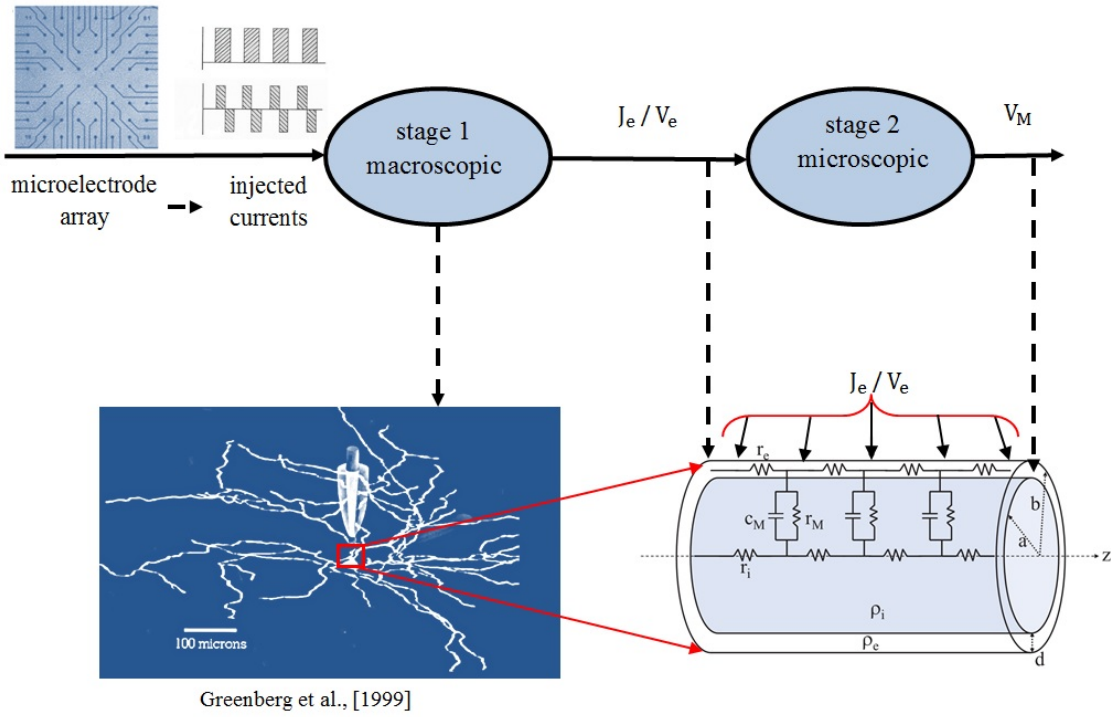

Figure 2.3: Two-stage modeling approach. Stage 1: Calculation of the extracellular potential or current density from the extracellular point source stimulation. Stage 2: The result of stage 1 is used to calculate the membrane potential, V_M.

1992, Einziger et al., 2005, Emertrout and Terman, 2009]. Both volume conductor and cellular composite models use a two-stage approach. The first stage calculates the extracellular potential arising from stimulation by a set of electrodes (macroscopic scale). The second stage applies the calculated extracellular potential from the first stage to determine the membrane potential of the neurite (microscopic scale). Figure 2.3 graphically shows the two-state approach. As depicted, stage 1 involves the stimulation of tissue with an array of electrodes. The injected current, commonly monophasic or biphasic pulses, from the electrodes into the extracellular space sets up a potential and current density in tissue. On the boundary of the thin extracellular sheath (the outer cylinder), the stimulus takes certain values that can be framed as a current density $\mathbf{J}_e$ or voltage V_e. The neurite membrane is modeled by distributed RC elements. The specified boundary conditions are used in conjunction with a relevant equation to obtain the membrane potential. The membrane potential can either be expressed as a partial differential equation, namely the

cable equation [McNeal, 1976,Rattay, 1986,Ganapathy and Clark, 1987,Coburn, 1988,Rattay, 1999] if the current direction is along the axis of the neurite, (the z-direction in Figure 2.4 (a)); or an ordinary differential equation if the current pathway is perpendicular to the neurite axis [Meffin et al., 2012]. This effect is shown in Figure 2.4 (b) and (c) where the current causes depolarization as it enters the cell (red) and causes hyperpolarization while exiting from another side (blue).

2.3 Volume Conductor Models

Strictly speaking, the volume conduction method that has traditionally been used is only relevant to stage 1; that is to describe the conduction of current through a volume to set up potential. Stage 2 is not a volume conductor. However, in this thesis, we have categorized these models under the two-stage volume conductor approach to contrast them with the recent two-stage approach, the cellular composite model.

In the standard volume conductor approach, neural tissue is described by its bulk conductivity, which is smooth and homogeneous on the microscale. In the macroscopic stage, the current density, $\mathbf{J}_\mathrm{e}$, and the extracellular potential, V_e, are related via the set of equations

$$\begin{aligned} \mathbf{J}_\mathrm{e} &= -\sigma \nabla V_\mathrm{e}, \quad \text{constitutive equation,} \\ \nabla \cdot \mathbf{J}_\mathrm{e} &= 0, \qquad\qquad \text{continuity equation,} \end{aligned} \tag{2.18}$$

which are derived from Maxwell's equations. The constitutive equation, relates the extracellular current density to the extracellular potential via a constant conductivity, σ. The continuity equation ensures the conservation of the current density and is a consequence of Kirchhoff's current law. Combining these equations leads to the Laplace's equation, $\nabla^2 V_\mathrm{e} = 0$. Solving this equation using the boundary conditions yields the extracellular potential. The extracellular potential from this stage is used in stage 2 for the calculation of the membrane potential in the longitudinal mode of stimulation. However, one of the limitations of this method is that it ignores transverse current flow. This is described by an ordinary differential equation [Meffin et al., 2012].

There are more limitations of standard volume conductor models. Figure 2.5 shows

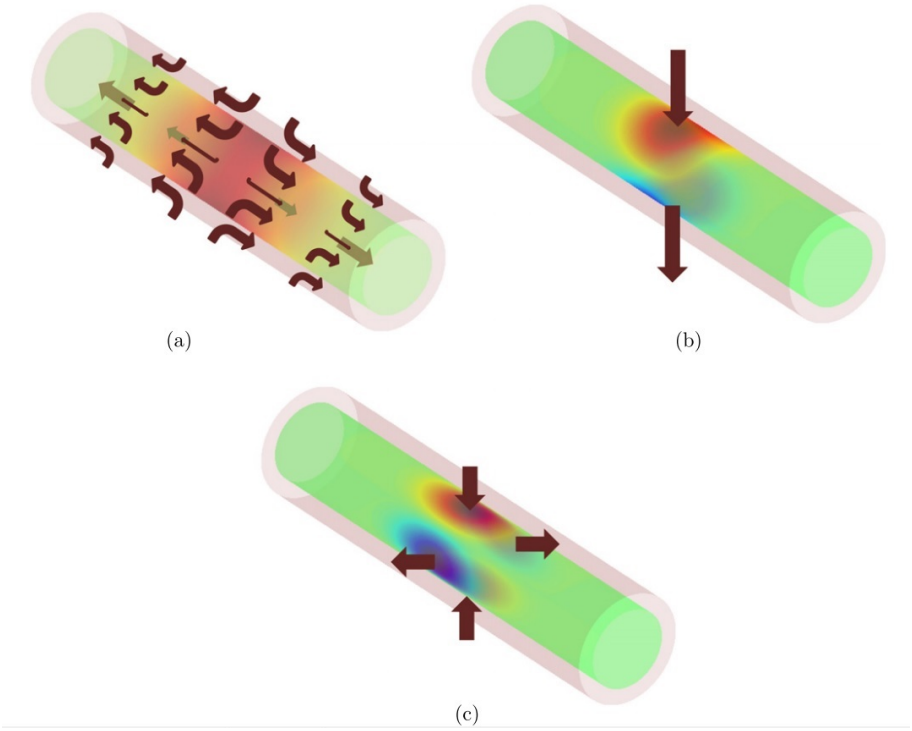

Figure 2.4: Different modes of stimulation. (a) The longitudinal mode of stimulation in which current passes along the main axis of the cylinder. (b) The transverse mode of stimulation in which current enters the neurite on one side (depolarization shown in red) perpendicular to the main axis and exits on the other side (hyperpolarization shown in blue). (c) The transverse mode where current crosses the neurite causing depolarization at two sites (red) and hyperpolarization at two other sites (blue).

one such limitation where the microscale inhomogeneities that exist in neural tissue is ignored in standard volume conductor models (Note the volume conductors only consider quasi-static state where the tissue is purely conductive.). These inhomogeneities include the long lengths of neurite within neural tissue of the order of hundreds to thousands of micrometers, as shown in Figure 2.5(a). Furthermore, neurons and other cells are tightly packed resulting in highly confined extracellular space, with widths of the order of 50 nm. The red lines in the electron microscopic image in Figure 2.5(b) show the extracellular space while the white areas are intracellular space. Furthermore, each cell has membrane capacitance due to the highly insulating phospholipid bilayer membrane, leading to the frequency dependence of the impedance between the extracellular and intracellular spaces. These microstructure inhomogeneities influence the current pathway in the

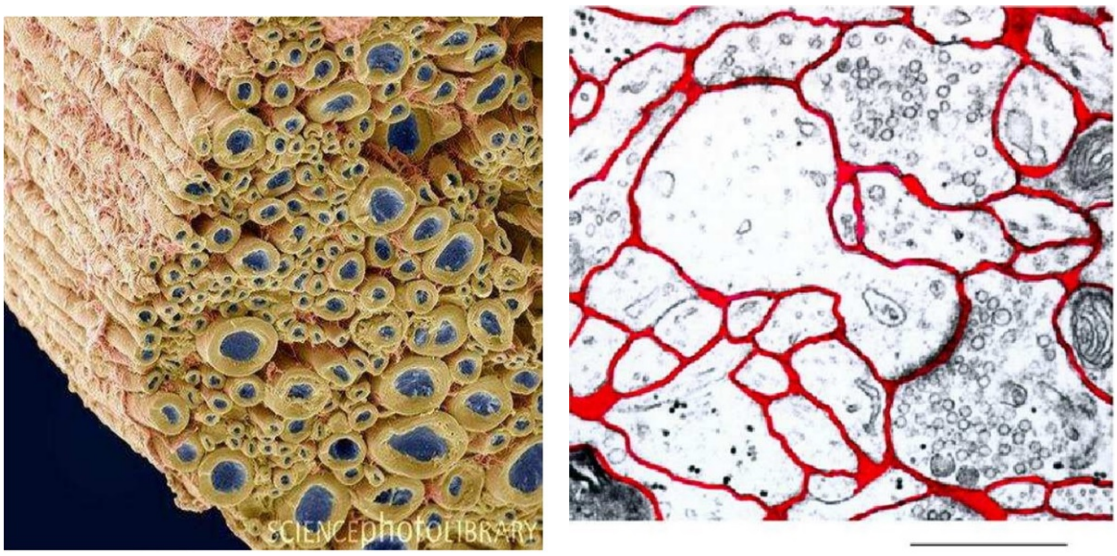

(a) (b)

Figure 2.5: (a) An electron micrograph of a fiber bundle (photo is taken from Science Photo Library). (b) An electron microscope image of neural tissue. Red lines represent the confined extracellular space that separates the intracellular parts of the neuron. The scale bar represents 1 μm [Meffin et al., 2012].

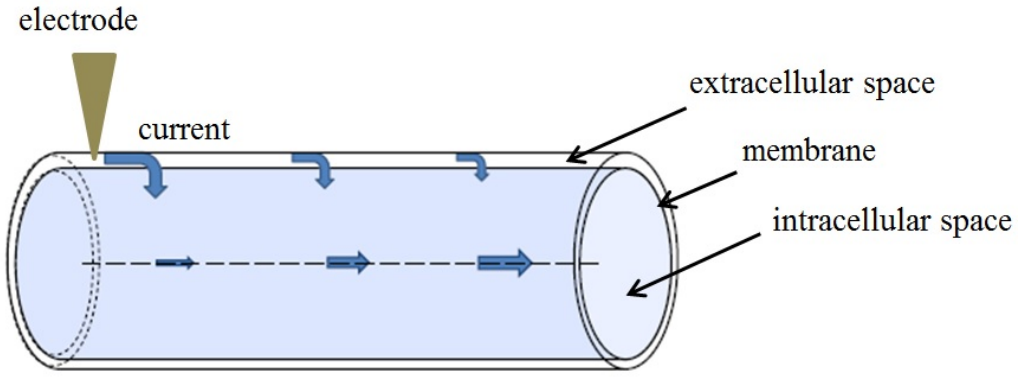

Figure 2.6: Current paths in neural tissue. The arrows show the weight of the current that passes through different spaces over the spatial scale λ.

extracellular and intracellular spaces. As depicted in Figure 2.6, closer to the electrode current is forced to pass through the extracellular space due to the fact that the membrane impedance is very high. However, further away from the electrode the membrane acts as a simple resistor that allows most of the current to pass through the membrane to access the intracellular pathway. This current redistribution occurs over spatial scales dictated

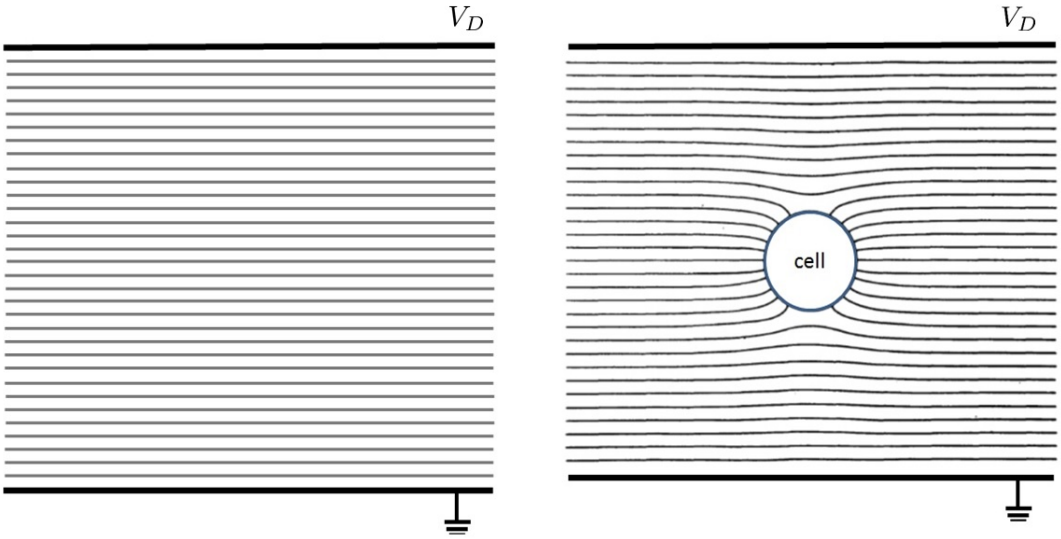

Figure 2.7: Effect of a cell in a volume conductor. (a) Stage 1 of the volume conductor ignores the effect of the cell (b) The cell in a volume conductor can change the shape of equipotential lines between V_D and the ground.

by the electrotonic length constant, λ.

Stage 1 of standard volume conductor models ignores the effect of the inhomogeneity of the neural tissue, in particular, the presence of the neurite within the volume conductor. This leads to an inconsistency between the solutions derived under current density or voltage boundary conditions. This is illustrated in Figure 2.7 which shows that the presence of a cell in the volume affects the equipotential lines within the volume conductor. If the effect of the cell is not taken into account an inconsistency may result between the membrane potentials that are calculated with the different boundary conditions. Meffin et al. (2014) developed trans-impedance equations in the cellular composite model that resolves this inconsistency.

2.4 Cellular Composite Model

In this modeling approach, the aim is to take into account the cellular composition of tissue, especially the microscale inhomogeneities, in a way that is self-consistent between stages 1 and 2. This requires understanding how tissue impacts on the neurite and a neu-

rite impacts on tissue. This is achieved by calculating how the bulk electrical properties of tissue arise from the electrical properties of its cellular constituents. It is important to note that there are also other self-consistent modeling approaches in the literature such as the hybrid finite element model by [Ying and Henriquez, 2007, Joucla et al., 2014] and the whole finite element modeling approach by [Joucla et al., 2014]. The main criticism of the hybrid modeling approach is that they are computationally expensive. The whole finite element modeling approach is a variation of the bidomain models. It takes into account the geometry of the cell and builds two domains corresponding to the extracellular and the intracellular spaces. These domains are linked via a thin film model of a membrane. However, this approach does not reflect the effect of an actual tissue on the neuron as the cell is isolated. This means the effect of neighboring cells and thus the admittivity of tissue was not taken into account. Note there might be a criticism that this effect can be taken into account by a whole finite element model if such a model includes several cells. However, the existence of several cells can cause current spread around those cells that cannot be explained by a whole finite model.

To address this problem, in the cellular composite model first, stage 2 calculations of the trans-impedance of single neurite are performed to recover the cable equation for the longitudinal mode on the way. Similarly, the equivalent equations for the transverse mode are also derived. By matching the impedance of the neurite to that of the surrounding tissue, the expression for the tissue admittivity is obtained that captures the properties of the cellular constituents and is self-consistent.

2.4.1 Cellular Composite Model Configuration

Figure 2.8 illustrates the cellular composite geometry and parameters. A neurite with a thin extracellular sheath is modeled as concentric cylinders. The thin extracellular sheath is one of the microscopic inhomogeneities that is taken into account here and restricts the extracellular current flow. The inner cylinder has a radius a, modeling the intracellular space, and is confined within another cylinder with radius b, modeling the extracellular space with thickness $d = b - a$, where $d \ll a$. The membrane is modeled with distributed passive electrical elements, conductance, and capacitance [Meffin et al., 2014].

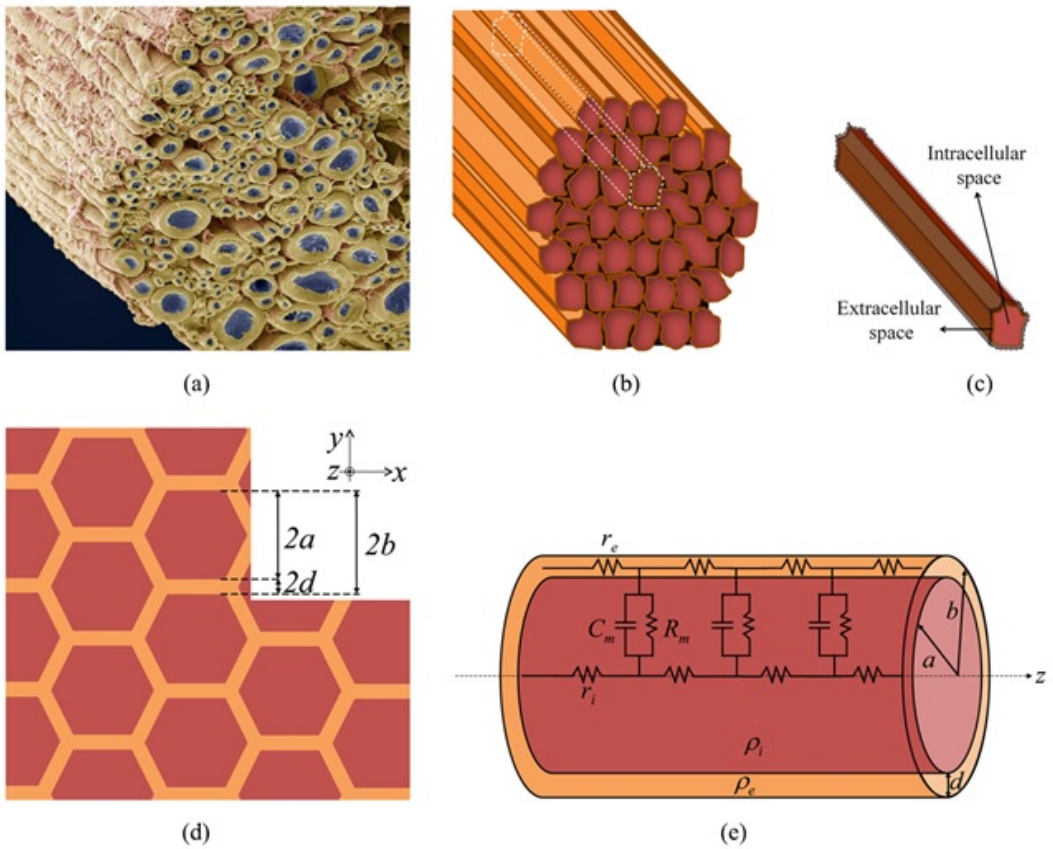

Figure 2.8: (a) An electron micrograph of a fiber bundle; (b) a conceptualized model of a fiber bundle consisting of parallel neurites with thin extracellular sheath; (c) A neurite with its extracellular space separated from the bundle; (d) Cross-section of an idealized fiber bundle for illustration purposes; (e) An approximation of a neurite with cylindrical intracellular and extracellular spaces and a passive RC model of membrane [Meffin et al., 2014].

An assumption of the model is that the extracellular and intracellular spaces are purely conductive and specified by their conductivities ρ_i and ρ_e.

A summary of the parameters of the cellular composite model is given in Table 2.1.

2.4.2 Stage 2: Membrane Potential Calculation

As shown in Figure 2.3, the membrane of a neurite is modeled as a distributed RC circuit and is defined as the voltage difference between the intracellular and the extracellular potentials $V_{\mathrm{m}} \triangleq V_{\mathrm{i}} - V_{\mathrm{e}}$.

Table 2.1: Parameters of the cellular composite model

Parameter	Description	Unit
a	Neurite radius	m
b	Outer cylinder radius	m
d	Width of the extracellular sheath, $d = b - a$	m
ρ_i	Intracellular space resistivity	Ω·m
ρ_e	Extracellular space resistivity	Ω·m
r_i	Intracellular resistance per unit length, $r_i = \rho_i / \pi a^2$	Ω·m^{-1}
r_e	Extracellular resistance per unit length, $r_e = \rho_e / \pi(b^2 - a^2)$	Ω·m^{-1}
R_M	Membrane unit area resistance	Ω·m^2
r_m	Membrane unit length resistance, $r_m = R_M / 2\pi a$	Ω·m
C_M	Membrane capacitance per unit area	Fm^{-2}
c_m	Membrane capacitance per unit length, $c_m = 2\pi a C_M$	Fm^{-1}
J_A	Current density on the outer cylinder boundary	Am^{-2}
J_M	Membrane normal current density	Am^{-2}
V_A	Electrical potential on the outer cylinder	V
V_m	Electrical potential difference across the membrane	V
ϕ_i	Electrical potential within intracellular space	V
ϕ_e	Electrical potential within extracellular space	V

Calculations are performed for the different modes of stimulation, namely the longitudinal and the transverse modes [Meffin et al., 2012, Meffin et al., 2014]. The Fourier transform method, as defined in Table 2.2, was used to perform the calculations. The spatial Fourier transform is denoted by $\check{f}(.)$ and the temporal Fourier transform is denoted by $\hat{f}(.)$. In this Table, z and k are the spatial Fourier transform pair and t and w are the temporal Fourier pair.

Longitudinal Mode

Voltage Boundary Conditions. The membrane potential under the voltage boundary condition for the longitudinal mode is given by

$$\lambda_{0V}^2 \frac{\partial^2 V_{\mathrm{m,L}}}{\partial z^2} - \tau_m \frac{\partial V_{\mathrm{m,L}}}{\partial t} - V_{\mathrm{m,L}} = \lambda_{0V}^2 \frac{\partial^2 V_{\mathrm{e}}}{\partial z^2}, \tag{2.19}$$

Table 2.2: Fourier transform (FT) notations

Signal	FT notation	FT equation	Inverse FT equation
$f(z):$	$\check{f}(k) = \mathcal{F}\{f(z)\}(k),$	$\check{f}(k) = \frac{1}{\sqrt{2\pi}} \int_z f(z) e^{-jkz} dz,$	$f(z) = \frac{1}{\sqrt{2\pi}} \int_k \check{f}(k) e^{jkz} dk,$
$h(t):$	$\hat{h}(w) = \mathcal{F}\{h(t)\}(w),$	$\hat{h}(w) = \frac{1}{\sqrt{2\pi}} \int_t h(t) e^{-jwt} dt,$	$h(t) = \frac{1}{\sqrt{2\pi}} \int_t \hat{h}(w) e^{jwt} dt,$

where $V_{\mathrm{m,L}}$ is the membrane longitudinal mode, V_{e} is the applied extracellular potential,

$$\lambda_{0V}^2 = \frac{R_{\mathrm{M}}}{2\pi a r_i} = \frac{r_m}{r_i}, \tag{2.20}$$

is the voltage electrotonic length constant, a is the neurite radius, R_M is the membrane unit area resistance and r_m and r_i are the membrane and intracellular unit length resistances. This equation corresponds to the classical cable equation developed in [Ganapathy and Clark, 1987, Coburn, 1988, Tuckwell, 1988].

Note, in order to calculate the membrane potential for finite-length fibers, an alternative approach is the mirror estimate by Joucla and Yvert, 2009. This provides an approximate solution for the passive cable equation by considering the distance of the fiber from the stimulation source. In fact, the mirror estimate method becomes the correct alternative to the activating function for long pulses. However, calculation of membrane potential is outside the scope of this thesis. Therefore, we refer the readers to [Joucla and Yvert, 2009] for further details.

Applying the Fourier transform to equation (2.19) gives

$$\hat{\mathring{V}}_{\mathrm{m,L}} = -\frac{k_z^2 \lambda_V^2(w)}{1 + k_z^2 \lambda_V^2(w)} \hat{\mathring{V}}_{\mathrm{e}}, \tag{2.21}$$

where

$$\lambda_V^2(w) = \frac{\lambda_{0V}^2}{1 + jw\tau_L}, \tag{2.22}$$

is the frequency dependent voltage electrotonic length constant. This term is the result of the complex impedance of the RC circuit of the membrane, $z_{\mathrm{m}}(w) = (1/r_{\mathrm{m}} + jwc_{\mathrm{m}})^{-1}$. This shows that the solution for V_{m} decays with the frequency-dependent length constant

[Meffin and Kameneva, 2011].

The extracellular potential creates a voltage difference across the membrane that forces the current into the intracellular space. This current passage from the extracellular space to the intracellular space occurs over a spatial scale determined by the voltage electrotonic length constant.

Current Density Boundary Conditions. The neuronal cable equation is recovered from the longitudinal mode of stimulation as

$$\lambda_{0J}^2 \frac{\partial^2 V_{\mathrm{m,L}}}{\partial z^2} - \tau_L \frac{\partial V_{\mathrm{m,L}}}{\partial t} - V_{\mathrm{m,L}} = \lambda_{0J}^2 \frac{\rho_{\mathrm{e}} b}{2d} \frac{\partial \mathbf{J}_{\mathrm{e},z}}{\partial z}, \tag{2.23}$$

where $V_{\mathrm{m,L}}$ is the membrane potential in the longitudinal direction, ρ_e is the extracellular space resistivity, b is the outer cylinder radius, d is the width of the extracellular sheath, $\mathbf{J}_{\mathrm{e},z}$ is the z component of the applied current density $\mathbf{J}_{\mathrm{e}}$ and

$$\lambda_{0J} \triangleq \frac{r_{\mathrm{m}}}{r_{\mathrm{e}} + r_{\mathrm{i}}}, \tag{2.24}$$

and

$$\tau_L \equiv \tau_M \triangleq R_M C_M, \tag{2.25}$$

are the electrotonic length constant and the membrane time constant, respectively. r_{m}, r_{e} and r_{i} are the membrane, the extracellular and the intracellular unit length resistances and are shown in Figure 2.3.

Equation (2.23) is a cable equation similar to equation (2.19) with a different electrotonic length constant and a different activating function.

Equation (2.23) can be expressed in the Fourier domain as

$$\hat{\mathring{V}}_{\mathrm{m,L}} = -\frac{jk_z \lambda_J^2(w)}{1 + k_z^2 \lambda_J^2(w)} \frac{b\rho_{\mathrm{e}}}{2d} \hat{\mathring{\mathbf{J}}}_{\mathrm{e},z}, \tag{2.26}$$

where k_z is the spatial Fourier transform of z and the frequency-dependent electrotonic length constant is defined as

$$\lambda_J^2(w) = \frac{\lambda_{0J}^2}{1 + jw\tau_L}. \tag{2.27}$$

The applied Fourier transformation helps reduce the partial differential equation (2.23) to an algebraic equation in the frequency domain. This equation can be solved numerically.

It is important to note that the voltage electrotonic length constant in equation (2.20) is larger than the current electrotonic length constant in equation (2.24). Physically, this difference arises from the fact that the applied voltage boundary condition clamps the voltage in the extracellular space. Hence, the extracellular resistance does not affect the extracellular potential.

Transverse Mode

Voltage Boundary Conditions. The transverse mode of stimulation under voltage boundary condition can be written as an ordinary differential equation

$$\tau_{T_V} \frac{dV_{\mathrm{m,T}}}{dt} + V_{\mathrm{m,T}} = -V_{\mathrm{e}}, \tag{2.28}$$

where

$$\tau_{T_V} \approx \rho_{\mathrm{i}} b C_M, \tag{2.29}$$

is the membrane time constant in the transverse mode under voltage boundary condition.

Current Boundary Conditions. The membrane potential for the transverse mode is described by an ordinary differential equation

$$\tau_{T_J} \frac{dV_{\mathrm{m,T}}}{dt} + V_{\mathrm{m,T}} = R_{\mathrm{M}} \mathbf{J}_{\mathrm{e,T}}, \tag{2.30}$$

where $V_{\mathrm{m,T}}$ is the transverse membrane potential, $\mathbf{J}_{\mathrm{e,T}}$ denotes the outward normal component of $\mathbf{J}_{\mathrm{e}}$ relative to the membrane surface and

$$\tau_{T_J} = \left(\frac{1}{R_{\mathrm{M}}} + \frac{1}{\rho_i b + \dfrac{\rho_e b^2}{d}} \right)^{-1} C_{\mathrm{M}}, \tag{2.31}$$

is the transverse mode time constant under current density. This is illustrated in Figure

Table 2.3: Summary of membrane potential equations

Longitudinal mode	
current boundary condition	$\lambda_{0J}^2 \frac{\partial^2 V_{\mathrm{m,L}}}{\partial z^2} - \tau_L \frac{\partial V_{\mathrm{m,L}}}{\partial t} - V_{\mathrm{m,L}} = \lambda_{0J}^2 \frac{\rho_{\mathrm{e}} b}{2d} \frac{\partial \mathbf{J}_{\mathrm{e},z}}{\partial z}$
voltage boundary condition	$\lambda_{0V}^2 \frac{\partial^2 V_{\mathrm{m,L}}}{\partial z^2} - \tau_m \frac{\partial V_{\mathrm{m,L}}}{\partial t} - V_{\mathrm{m,L}} = \lambda_{0V}^2 \frac{\partial^2 V_{\mathrm{e}}}{\partial z^2}$
Transverse mode	
current boundary condition	$\tau_{T_J} \frac{dV_{\mathrm{m,T}}}{dt} + V_{\mathrm{m,T}} = R_M \mathbf{J}_{\mathrm{e,T}}$
voltage boundary condition	$\tau_{T_V} \frac{dV_{\mathrm{m,T}}}{dt} + V_{\mathrm{m,T}} = -V_{\mathrm{e}}$

2.4(b) and (c). Meffin et al. (2014) argued that the effects of higher transverse modes, i.e., $n > 1$, on the membrane potential are negligible.

2.4.3 Trans-impedance Calculations

The applied voltage at the boundary of the outer cylinder dictates a certain current density on the boundary and vice versa. This relationship can be expressed by the trans-impedance equation [Meffin et al., 2012].

The equations describing the membrane potential under various boundary conditions are different, as shown in Table 2.3. The source of this difference in the longitudinal mode is the different electrotonic length constants under current density and voltage boundary conditions. For the transverse mode, different time constants apply under different boundary conditions. This inconsistency can be removed by ensuring that the impedance of tissue in stage 1 is matched with the trans-impedance of the neurite plus the thin extracellular sheath in stage 2. This means that $\mathbf{J}_{\mathrm{e}}$ and V_{e} must be related by the trans-impedance equation for self-consistency. The satisfaction of this condition will lead to the same answer for V_{m} regardless of which boundary condition type and equation are

used. If it is assumed that $\rho_e \approx \rho_i$ and $d \ll b$, then the trans-impedance equation for the longitudinal mode of stimulation in the z-direction in the Fourier domain is

$$\hat{\tilde{Z}}_{\mathrm{e}}(k_z, w) = -\frac{2\pi b r_e r_i}{k_z^2(r_e + r_i)} \left(\frac{1 + k_z^2 \lambda_V^2(w)}{1 + k_z^2 \lambda_f^2(w)} \right), \tag{2.32}$$

where r_i and r_e are the intracellular and extracellular resistances per unit length, respectively and b is the radius of the outer cylinder.

The trans-impedance equation in the transverse mode is simpler as it does not have any frequency-dependent components,

$$\hat{\tilde{Z}}_{\mathrm{e}} \approx \frac{\rho_e b^2}{d}, \tag{2.33}$$

where d is the width of the extracellular space.

Equations (2.32) and (2.33) are the key to ensuring consistency between stimulation via current density and voltage boundary conditions. Practically, this is done by matching the tissue admittivity to an equivalent resistivity of the neurite plus thin extracellular sheath.

The trans-impedance equations on the boundary capture all the internal electrical impedance properties of the neurite with the thin extracellular sheath on the boundaries between the fibers [Meffin et al., 2014, Borcea, 2002]. Therefore, the equation for the intracellular and membrane potentials can be replaced by the trans-impedance equations to calculate the extracellular potential in stage 1.

2.4.4 Stage 1: Extracellular Potential Equations

Using the trans-impedance equations introduced in the previous section, we may obtain stage 1 equations that describe the extracellular potential of tissue. In this stage the assumption is that any cylinder of diameter b obeys the trans-impedance equation for a neurite with thin extracellular sheath element of the same dimension. This is an impedance matching process, to make the two-stage model consistent, and has a physical interpretation that the admittivity of tissue is the sum of the individual admittivities

of its components. Given this, the extracellular potential and current density of tissue comprised of identical parallel fibers are

$$\begin{aligned} \mathbf{J}_\mathrm{e} &= -\frac{1}{2\pi}\xi_\mathrm{e}(z,t) \underset{z,t}{*} \nabla V_\mathrm{e}, \quad \text{constitutive equation,} \\ \nabla \cdot \mathbf{J}_\mathrm{e} &= 0, \qquad\qquad\qquad\qquad \text{continuity equation.} \end{aligned} \tag{2.34}$$

The convolution, denoted by '$*$', is a novel aspect of the cellular composite model as opposed to the volume conductor case where the constitutive equation is described by a constant conductivity, $\mathbf{J}_\mathrm{e} = -\sigma\nabla V_\mathrm{e}$. Mathematically, it is derived as the last step inverting the Fourier transform in a mean-field derivation. Physically, it relates the extracellular current density to the extracellular electric field at remote locations and past times. The admittivity kernel is expressed as $\xi_\mathrm{e}(z,t)$, which is

$$\xi_\mathrm{e}(z,t) = \begin{bmatrix} \xi_{\mathrm{e,T}}(z,t) & 0 & 0 \\ 0 & \xi_{\mathrm{e,T}}(z,t) & 0 \\ 0 & 0 & \xi_{\mathrm{e,L}}(z,t) \end{bmatrix}, \tag{2.35}$$

and in the Fourier domain can be expressed as

$$\begin{aligned} \hat{\hat{\xi}}_{\mathrm{e,T}} &= \frac{d}{b\rho_e}, \\ \hat{\hat{\xi}}_{\mathrm{e,L}}(k_z,w) &= \frac{1}{\rho_i}\left(\frac{1+\lambda_J(w)^2k_z^2}{1+\lambda_V(w)^2k_z^2}\right). \end{aligned} \tag{2.36}$$

The solution to equation (2.34) can then be applied to equation (2.19) or (2.23) for the longitudinal mode and to equation (2.28) or (2.30) for the transverse mode of stimulation, depending on the boundary conditions.

2.5 A Note on Electrotonic Length Constants

The electrotonic length constants defined in the longitudinal mode of stimulation describe the spatial impulse response of a neurite to an extracellular stimulus. Depending on the choice of the boundary condition, either the current density electrotonic length

constant, $\lambda_J(w)$ or voltage electrotonic length constant, $\lambda_V(w)$ can be computed. The result of these calculations have already been shown in equations (2.22) and (2.27) respectively. As stated before $\lambda_V(w)$ is larger than $\lambda_J(w)$. This is due to the voltage being clamped in the extracellular space and hence the extracellular resistance does not affect the potential in this space.

$$\frac{\lambda_V(w)}{\lambda_J(w)} = \frac{\lambda_{0_V}}{\lambda_{0_J}} = \sqrt{1 + \frac{r_e}{r_i}} \approx \sqrt{\frac{b\rho_e}{2d\rho_i}} > 1. \tag{2.37}$$

The electrotonic length constants determine the distances over which the extracellular current can access the intracellular space. Details on this will be discussed in the following chapters.

2.6 Summary

The cellular composite model has some properties not shared by the standard volume conductor model with constant conductivity. The cellular composite model takes into account the anisotropy effect through an admittivity which has a tensor form that changes as the extracellular current flow pathway changes. The important point about the anisotropy is that it is related quantitatively to the underlying cellular morphology and electrical properties for the first time through the cellular composite approach. The effect of the membrane capacitance is that it provides a finite memory for the system, which is reflected in the time convolution. The spatial convolution captures the effects of current paths between points in the extracellular spaces via the intracellular spaces which is a non-local effect. These inhomogeneities are not modeled in standard volume conductor models. It was also shown that, if the applied boundary conditions to neural tissue are related to each other with the trans-impedance equations, the membrane potential solutions are self-consistent.

A main purpose of introducing the cellular composite models was to show that neural tissue, specifically those structures in the brain such as cortical gray matter are not simple resistive mediums as they contain components that have spatial and temporal

frequency dependence. However, Logothetis et al. claimed that based on their measurement strategy from monkey visual cortex, the cortical tissue could be modeled as a purely conductive medium [Logothetis et al., 2007]. This allowed for unbiased propagation of any temporal frequency signal. The authors separated their measurement into lateral (tangential) and radial measurements. The measurements in the gray and white matters showed a homogeneity in a tangential direction, while anisotropy and inhomogeneity existed in a radial direction. Their findings in the gray matter revealed that the conductivity of tissue is comparable in all directions, i.e., the conductivity does not depend on the direction of the measurements. This is a point that will be discussed in detail throughout this thesis. We will answer if viewing the gray matter as a purely resistive medium provides a good approximation for modeling purposes or not.

In addition, the cellular composite model has only been applied to neural tissue with parallel fiber arrangements, which is known as a fiber bundle. We are going to apply this technique to more complex structures where fibers may have arbitrary orientations and may not necessarily be parallel to each other. In the following chapters, we introduce tissues with different morphologies and arrangement of fibers and calculate the admittivity and the extracellular potential that are associated with stage 1. Also importantly we are going to explore the repercussions of having a tissue admittivity that has spatial and temporal frequencies dependence.

It is important to note that temporal frequency dependence effects have been incorporated into models by [Bossetti et al., 2007] but their model does not include any spatial frequency dependence. The authors compared the quasi-static solution (an infinite, homogeneous and isotropic volume conductor) from Poissons equation with a solution (included inductive, capacitive and wave propagation effect) from an inhomogeneous Helmholtz equation. Their conclusion was that the inductive and propagation effects are negligible over physiologically relevant distances but this is not true for the conductivity. In our work, we assume the inductive and wave propagation effects are small and thus can be ignored. They also concluded that capacitive effects due to temporal frequency dependence of the admittivity were small ($< 10\%$) and could often be neglected. However, their model was fit to data on the dielectric properties of grey matter obtained from

measurement at low spatial frequencies, much smaller than the inverse of the electrotonic length constant of neurites. The cellular composite model agrees that capacitive effects will be minimal at low spatial frequencies, but predicts that they should be more pronounced at higher spatial frequencies, in the order of the inverse electrotonic length constant.

2.7 Contributions of This Thesis

In the present study, a mathematical framework to calculate the admittivity and the extracellular potential of neural tissue using its cellular constituents is developed. Our methodology is an extension of the cellular composite modeling framework by Meffin and Tahayori and others [Meffin et al., 2012,Tahayori et al., 2012,Meffin et al., 2014,Tahayori et al., 2014].

The admittivity is calculated by considering the cellular composition of neural tissue, such as the thin extracellular space between cells and the high impedance membrane capacitance. These properties cause tissue to appear more inhomogeneous in microscale which is in contrast with standard models of electrical stimulation, i.e., where tissue is assumed homogeneous and purely conductive everywhere. Apart from this, we take into account orientation distribution of fibers within tissue.

Chapter 3, presents neural tissue with stellate distribution of fiber orientations. We will show how the extracellular potential changes given both a uniform and a Gaussian distribution of fibers. This is performed for a monophasic pulse of different pulse-widths to show how parameters of electrical stimulation affect tissue response.

In Chapter 4, we will consider a laminar structure similar to the neocortex or the retina for fiber orientation. We will show how anisotropy and various pulse-widths influence neural response. An extension to double layer inhomogeneous tissue, as well as a Gaussian distribution of fiber orientation, is also presented mathematically.

Chapter 5, presents neural tissue consist of glia and neurons. We will assume a different distribution of fiber orientations based on the common morphologies of these cells in the brain. Glial cells morphology is assumed more isotropic similar to stellate cells. For

neurons, a combination of laminar structure, resembling tufted dendrites of pyramidal cells, and a single fiber, as a model of apical dendrite or axon, is considered. We will investigate the effect of glia proportion on the brain resistivity and will also show how anisotropy of tissue changes as the population of various cell morphologies changes.

Finally, a summary of our results and the future direction of this work will be discussed in Chapter 6.

Chapter 3

Isotropic Tissues with a Uniform Distribution of Fiber Orientations

3.1 Introduction

A deeper understanding of electrical stimulation of neural tissue is particularly important for developing medical bionic devices to either treat a disease or use it to augment a sense. Example are bionic eye devices that restore partial function of lost cells, or deep brain stimulation for treatment of neurological disabilities, such as epileptic seizures. Modeling of electrical stimulation is important because it will facilitate selective activation of target neural populations.

In the standard volume conductor approach, neural tissue is assumed to be homogeneous, even at the microscopic scale. Homogeneity results in having a local conductivity that is constant everywhere in tissue. However, real tissue is composed of cells and neurites in which the extracellular and intracellular spaces are separated by membranes. Neural membranes have capacitive and high impedance properties, but intra and extracellular spaces have comparatively low resistance. Neural tissue is composed of tightly packed fibers as displayed in Figure 3.1(a). This structure restricts the passage of current through the extracellular space creating a high extracellular resistance, Figure 3.1(b). Each fiber in tissue has a diameter that is wide compared to the width of the extracellular space, resulting in a low resistance intracellular pathway along the full fiber length. However, this current pathway is hard to access due to the existence of the high impedance membrane. None of these facts are accounted in the standard volume conductor models.

Meffin et al. (2012) provided a modified framework to the standard volume con-

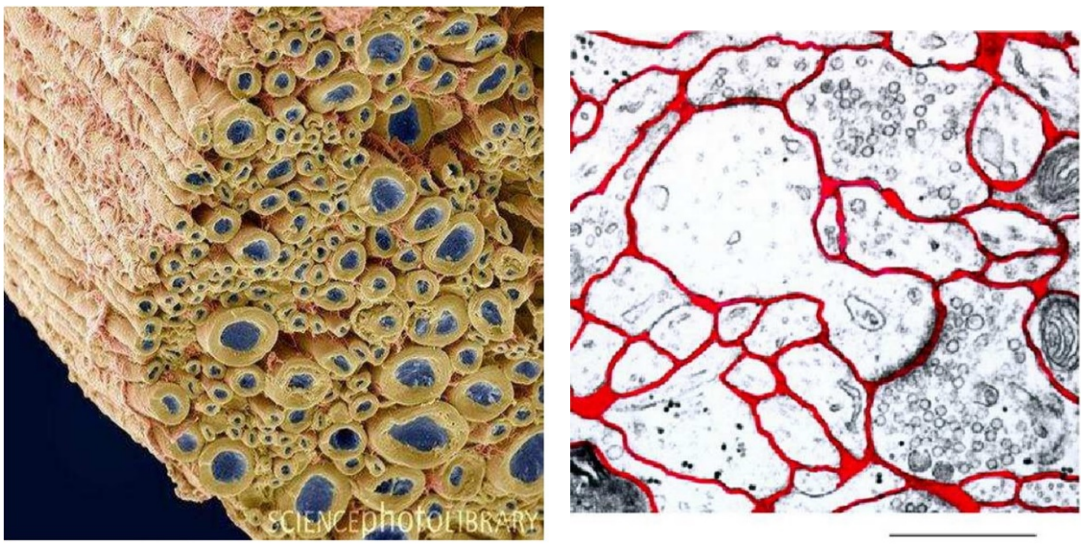

(a) (b)

Figure 3.1: (a) Fiber bundle is an example of neural tissues with tightly packed parallel fibers (b) Cross-section of neural tissue. Red parts are the confined extracellular space. Scale bar is 1 μm.

ductor approach to address these issues. They introduced an admittivity to account for the cellular geometry, which replaces the conductivity used in the standard volume conductor models. The admittivity was derived by characterizing the electrical properties of individual neurites via a trans-impedance equation. In a further study, they used a mean-field approach to find the admittivity for a composite of neurites [Meffin et al., 2014]. The admittivity changes the spatiotemporal profile of the electrical potentials in a standard volume conductor approach. In this Chapter, we apply the framework for modeling the effect of the cellular composition of tissue in a volume conductor. The main contribution in this chapter is to calculate the admittvity and the extracellular potential for a specific tissue type. The tissue is composed of neurites that are crossing each other in all directions representing cortical tissue. Here we consider an isotropic case of equal probability for neurite directions. This resembles a fiber arrangement similar to a stellate cell in Figure 3.2. We examine how cellular geometry affects the spatiotemporal profile of the extracellular potential and how different the profiles are compared to the standard volume conductor approach.

We first recall the equations of the standard volume conductor model and then intro-

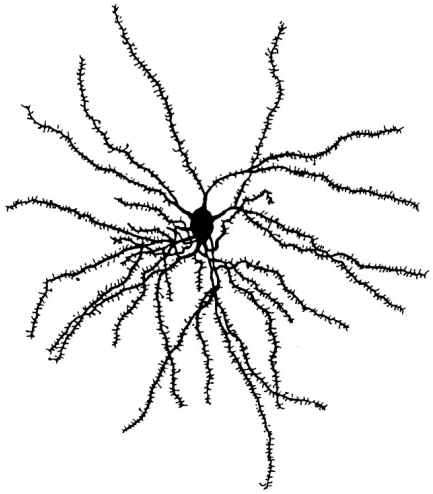

Figure 3.2: Stellate cell fiber arrangement [White and Keller, 1989].

duce the equivalent equations of the cellular composite volume conductor model.

3.2 Standard Volume Conductor Approach: Uniform Distribution of Fiber Orientation

The volume conductor approach involves both macroscopic and microscopic modeling stages. The first stage calculates the extracellular potential due to a set of electrodes (macroscopic scale). The second stage is to apply the calculation regarding the extracellular potential from stage 1 to an equation to determine the membrane potential (microscopic scale) [Meffin et al., 2012, Tahayori et al., 2012, McNeal, 1976, Coburn, 1988].

In the standard volume conductor approach, the current density, $\mathbf{J}_e$, and the extracellular potential, V_e, are related via a set of equations

$$\begin{aligned} \mathbf{J}_e &= -\sigma \nabla V_e, \\ \nabla \cdot \mathbf{J}_e &= 0. \end{aligned} \tag{3.1}$$

The first equation relates the current density to the extracellular potential via a constant conductivity, σ. The second equation is the continuity equation for the current density.

Combining these equations and adding a point source electrode on the right hand

side results in Poisson's equation

$$\sigma\left(\frac{\partial^2 V_{\mathrm{e}}}{\partial x^2}+\frac{\partial^2 V_{\mathrm{e}}}{\partial y^2}+\frac{\partial^2 V_{\mathrm{e}}}{\partial z^2}\right) \quad = \quad -\iota(t)\delta(x)\delta(y)\delta(z), \tag{3.2}$$

where $\delta(\cdot)$ is the Dirac delta function and $\iota(t)$ is the total current injected by a point source electrode. When Poisson's equation is solved, we are given a classical R^{-1} dependency for the decay in potential as a function of space

$$V_{\mathrm{e}}(\mathbf{R},t)=\frac{\iota(t)}{4\pi\sigma\mathbf{R}}, \tag{3.3}$$

where R is the distance from the electrode.

One approach to solve the partial differential equation (3.2) is to use the Fourier transform. The following definition is adopted in the application of the Fourier transform.

Definition 1. *The Fourier transform of a function $f(\mathbf{R})$ is denoted by $\mathcal{F}\{f(\mathbf{R})\}(\mathbf{k})$, where $\mathbf{R}=(x,y,z)$ and $\mathbf{k}=(k_x,k_y,k_z)$. The three-dimensional spatial Fourier transform pair is defined by*

$$\check{f}(\mathbf{k})=\left(\frac{1}{\sqrt{2\pi}}\right)^3\int_{R^3} f(\mathbf{R})e^{-j\mathbf{R}\cdot\mathbf{k}}d\mathbf{R}, \tag{3.4}$$

$$f(\mathbf{R})=\left(\frac{1}{\sqrt{2\pi}}\right)^3\int_{K^3} \check{f}(\mathbf{k})e^{j\mathbf{R}\cdot\mathbf{k}}d\mathbf{k}. \tag{3.5}$$

Using Definition 1, the extracellular potential of equation (3.2) is represented in the Fourier domain as

$$\hat{\check{V}}_{\mathrm{e}}(K)=\frac{\hat{\iota}(w)}{(2\pi)^2\sigma K^2}, \tag{3.6}$$

where w is the Fourier pair of t (i.e. the angular frequency), $K=|\mathbf{k}|$, and "$\hat{}$" is used to show the temporal Fourier transform. The inverse Fourier transform of this equation has $1/R$ dependency and is of the form of equation (3.3).

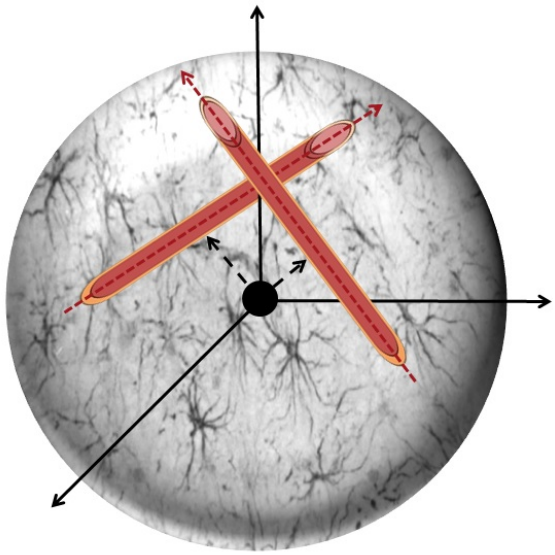

Figure 3.3: Uniform spherical distribution of fiber orientations configuration of fibers with a point source electrode at the origin (black solid circle). Red cylinders are the fibers in different orientation with their main axis shown in red dashed arrows.

3.3 Cellular Composite Model: Uniform Spherical Distribution of Fiber Orientation

3.3.1 Stage 1: Extracellular Potential Calculation

In the cellular composite volume conductor model, the local extracellular current density is related to extracellular electrical field via convolution with an admittivity kernel in time and space [Meffin et al., 2014].

Consider tissue composing crossing fibers which are classified by the index $h = 1, \cdots, H$. The local extracellular potential, V_{e}, is related to the local current density, $\mathbf{J}_{\mathrm{e,h}}$, via a spatiotemporal convolution equation

$$\mathbf{J}_{\mathrm{e,h}} = -\frac{1}{2\pi}\zeta_{\mathrm{e,h}} \underset{\mathbf{u}_h,t}{*} \nabla V_{\mathrm{e}}, \tag{3.7}$$

$$\mathbf{J}_{\mathrm{e}} = \sum_{h=1}^{H} \alpha_h \mathbf{J}_{\mathrm{e,h}}, \tag{3.8}$$

$$\nabla \cdot \mathbf{J}_{\mathrm{e}} = 0, \tag{3.9}$$

where $\xi_{\mathrm{e,h}}$ is the admittivity kernel for fibers of type h with both spatial and temporal arguments and is capturing the heterogeneity of tissue at the microscale. The admittivity is defined in such a way to capture some properties of the fibers such as their orientation, diameter, and membrane properties [Meffin et al., 2014]. α_h is the extracellular volume fraction occupied by fibers of type h, and $\mathbf{J}_{\mathrm{e}}$ is the mean extracellular current density of the tissue. $\mathbf{u}_h$ represents the unit vector parallel to a fiber axes as shown by red dotted arrows in Figure 3.3. The convolution on the direction of $\mathbf{u}_h$ (red dashed arrows in Figure 3.3) shows the orientation of a class of fiber in the model. The spatial convolution captures the effect of current paths between points in the extracellular space via the intracellular space. The capacitive property of the membrane leads to the time convolution. It relates the current density to the extracellular electrical field at previous times.

Definition 2. *The convolution in equation (3.7) is defined as:*

$$\begin{aligned}\xi_{\mathrm{e,h}} \underset{\mathbf{u}_h,t}{*} \nabla V_{\mathrm{e}}(\mathbf{p},t) = \int_{-\infty}^{\infty}\int_{-\infty}^{\infty} \xi_{\mathrm{e,h}}(s'\mathbf{u}_h, t' : \mathbf{u}_h) \\ \times \nabla V_{\mathrm{e}}(\mathbf{p} - s'\mathbf{u}_h, t - t')ds'dt'.\end{aligned} \tag{3.10}$$

The admittivity kernel, $\xi_{\mathrm{e,h}}$, for this general structure is defined in the Fourier domain as

$$\begin{aligned}\hat{\hat{\xi}}_{\mathrm{e,h}}(\mathbf{k}, w : \mathbf{u}_h) &= \hat{\hat{\xi}}_{\mathrm{e,T}} I_3 + (\hat{\hat{\xi}}_{\mathrm{e,L}}(\mathbf{k}, w : \mathbf{u}_h) - \hat{\hat{\xi}}_{\mathrm{e,T}})\mathbf{u}_h\mathbf{u}_h^T, \\ \hat{\hat{\xi}}_{\mathrm{e,T}} &= \frac{d}{b\rho_{\mathrm{e}}}, \\ \hat{\hat{\xi}}_{\mathrm{e,L}}(\mathbf{k}, w : \mathbf{u}_h) &= \frac{1}{\rho_{\mathrm{i}}}\frac{1 + jw\tau_m + (\mathbf{k}\cdot\mathbf{u}_h)^2\lambda_{0J}^2}{1 + jw\tau_m + (\mathbf{k}\cdot\mathbf{u}_h)^2\lambda_{0V}^2},\end{aligned} \tag{3.11}$$

where $\hat{\hat{\xi}}_{\mathrm{e,T}}$ and $\hat{\hat{\xi}}_{\mathrm{e,L}}(\cdot)$ are the transverse and longitudinal components of the admittivity, $\hat{\hat{\xi}}_{\mathrm{e}}(\cdot)$. $I_{3\times3}$ is the 3×3 identity matrix, $\mathbf{u}_h\mathbf{u}_h^T$ is an outer product, τ_m is the membrane time constant, ρ_{e} and ρ_{i} are the extracellular and intracellular resistivities of the tissue, b is the radius of an ideal cylindrical neurite and d is the thickness of the extracellular sheath (equal to half the width of the extracellular space between neighboring cells). λ_{0J} and λ_{0V} are the electrotonic length constants calculated under current density and voltage boundary conditions for the cable equation, respectively, and can be expressed in terms

of the fiber's physical parameters,

$$\begin{aligned} \lambda_{0J}^2 &\equiv \frac{r_\mathrm{m}}{r_\mathrm{e}+r_\mathrm{i}}, \\ \lambda_{0V}^2 &\equiv \frac{r_\mathrm{m}}{r_\mathrm{i}}, \end{aligned} \tag{3.12}$$

where $r_\mathrm{m} = \dfrac{R_\mathrm{m}}{2\pi b}$ is the membrane per unit length resistance. R_m is the membrane per unit area resistance and b is the neurite radius. $r_\mathrm{e} \approxeq \dfrac{\rho_\mathrm{e}}{2\pi b d}$ is the extracellular resistance per unit length. d is the width of the extracellular space and $r_\mathrm{i} \approxeq \dfrac{\rho_\mathrm{i}}{\pi b^2}$ is the intracellular resistance per unit length. Details of these calculations can be found in Chapter 2, section 2.3.1.

Substituting equation (3.7) into equations (3.8) and (3.9) for a point source at the origin, we find

$$\frac{1}{2\pi}\nabla\cdot\Big(\sum_{h=1}^{H}\alpha_h\xi_{\mathrm{e,h}}\underset{\mathbf{u}_h,t}{*}\nabla V_\mathrm{e}\Big) = -\iota(t)\delta(x)\delta(y)\delta(z). \tag{3.13}$$

Taking a four-dimensional Fourier transform in time and space and rearranging the terms for V_e gives

$$\hat{\mathring{V}}_\mathrm{e}^{\mathrm{cart}}(\mathbf{k}) = \frac{\hat{\iota}(w)}{(2\pi)^2\sum_{h=1}^{H}\alpha_h\mathbf{k}^T\hat{\mathring{\xi}}_{e,h}\mathbf{k}}, \tag{3.14}$$

where $\hat{\mathring{V}}_\mathrm{e}^{\mathrm{cart}}$ is the Fourier transform of the extracellular potential calculated in Cartesian coordinates.

Assumption 1. *The distribution of fiber orientation is uniform in a spherically symmetric tissue.*

We parameterize fiber orientation using spherical polar coordinates so that $\mathbf{u}_h$ lies on the unit sphere centered at the origin. The spherical polar coordinate system is chosen such that axis of rotation is aligned with the vector $\mathbf{k}$. Thus, ϕ is the angle between $\mathbf{k}$ and the unit vector $\mathbf{u}_h$, so that $\mathbf{k}\cdot\mathbf{u}_h = K\cos\phi$. The angle θ is the angle between the projection of $\mathbf{u}_h$ onto the plane perpendicular to $\mathbf{k}$, and some arbitrary vector in that plane (see Figure. 3.4.). The sum over fiber orientations, $\sum_{h=1}^{H}\alpha_h\mathbf{k}^T\hat{\mathring{\xi}}_{\mathrm{e,h}}\mathbf{k}$, can be expressed as the integral in the limit of a continuous distribution of an infinite number of fiber orientations

$$\sum_{h=1}^{H}\alpha_h\mathbf{k}^T\hat{\mathring{\xi}}_{\mathrm{e,h}}\mathbf{k} = \frac{1}{4\pi}\int_0^{2\pi}\int_0^{\pi}\mathbf{k}^T\hat{\mathring{\xi}}_\mathrm{e}(\mathbf{k},w:\mathbf{u}_h)\mathbf{k}\sin\phi d\phi d\theta. \tag{3.15}$$

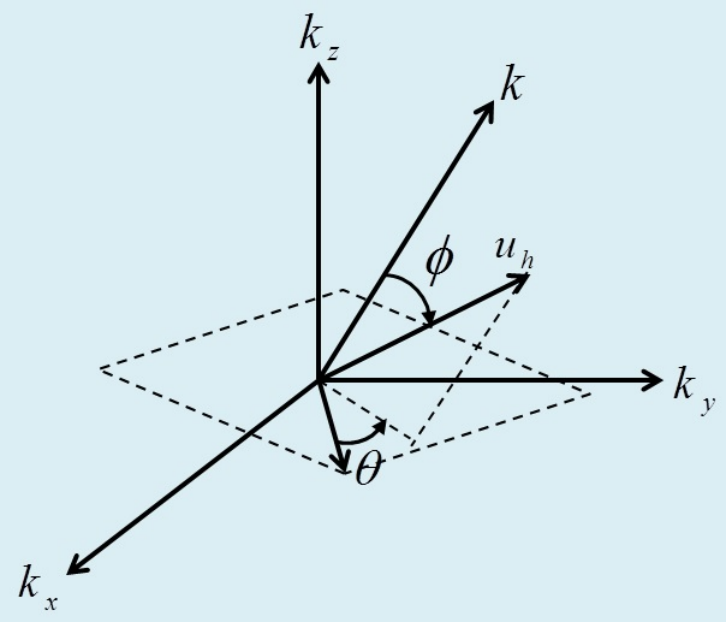

Figure 3.4: Spherical polar coordinates. The dotted line projecting $\mathbf{u}_h$ onto the plane is parallel to $\mathbf{k}$ and project onto the plane perpendicular to $\mathbf{k}$. θ is the angle from some arbitrary vector in the plane (dotted parallelogram) perpendicular to $\mathbf{k}$.

The volume fraction α_h becomes a differential area on the surface of the unit sphere $d\alpha = \frac{\sin\phi d\phi d\theta}{4\pi}$, normalized to integral of unity. This is to have $\int_{\theta,\phi} d\alpha = \int_0^{2\pi}\int_0^{\pi} \frac{\sin\phi d\phi d\theta}{4\pi} = 1$.

Substituting for $\hat{\hat{\xi}}_{\mathrm{e,h}}(\mathbf{k}, w : \mathbf{u}_h)$ from equation (3.11), the integral in equation (3.15) becomes

$$\begin{aligned}\frac{1}{4\pi}\int_0^{2\pi}\int_0^{\pi} \mathbf{k}^T \hat{\hat{\xi}}_{\mathrm{e,h}}(\mathbf{k}, w : \mathbf{u}_h)\mathbf{k}\sin\phi d\phi d\theta =& \frac{1}{4\pi}\int_0^{2\pi}\int_0^{\pi} \hat{\hat{\xi}}_{\mathrm{e,T}}\mathbf{k}^2 \\ &+ \left(\hat{\hat{\xi}}_{\mathrm{e,L}}(\mathbf{k}\cdot\mathbf{u}_h, w) - \hat{\hat{\xi}}_{\mathrm{e,T}}\right) \times (\mathbf{k}\cdot\mathbf{u}_h)^2 \sin\phi d\phi d\theta \\ =& g_1 K^2 + \frac{g_2}{\lambda_V^2(w)}\left(1 - \frac{\tan^{-1}(K\lambda_V(w))}{K\lambda_V(w)}\right),\end{aligned} \tag{3.16}$$

where $\mathbf{k}.\mathbf{u}_h = K\cos\phi$ and the approximation $d/b \ll 1$ is used to simplify some of the

following expressions (assuming ρ_i and ρ_e have similar magnitudes).

$$\begin{aligned} g_1 =& \frac{2}{3}\frac{d}{b\rho_\mathrm{e}} + \frac{1}{3}\frac{1}{\rho_\mathrm{i} + \rho_\mathrm{e}\frac{b}{2d}} \approxeq \frac{4}{3}\frac{d}{b\rho_\mathrm{e}}, \\ g_2 =& \frac{1}{\rho_\mathrm{i}}\frac{\rho_\mathrm{e}}{\rho_\mathrm{e} + \rho_\mathrm{i}\frac{2d}{b}} \approxeq \frac{1}{\rho_\mathrm{i}}, \\ \lambda_V(w) =& \frac{\lambda_{0V}}{\sqrt{1 + jw\tau_m}}. \end{aligned} \tag{3.17}$$

In spherical coordinates, equation (3.14) is

$$\mathring{V}_\mathrm{e}^\mathrm{sph}(K) = \frac{-jK\hat{\imath}(w)}{(2\pi)^2\left[\frac{4}{3}\frac{d}{b\rho_\mathrm{e}}K^2 + \frac{1}{\rho_i\lambda_V^2(w)}\left(1 - \frac{\tan^{-1}(K\lambda_V(w))}{K\lambda_V(w)}\right)\right]}. \tag{3.18}$$

Refer to Appendix A for calculation details. As this equation is only dependent on $K = |\mathbf{k}|$, by performing a modified, one-dimensional inverse Fourier transform of equation (3.18) with respect to K, instead of the normal three-dimensional inverse Fourier transform with respect to $\mathbf{k}$, we have

$$V_\mathrm{e}^\mathrm{sph}(|R|) = \frac{\mathcal{F}^{-1}\{\mathring{V}_\mathrm{e}^\mathrm{sph}(K)\}}{R}, \tag{3.19}$$

where, by definition, $V_\mathrm{e}^\mathrm{sph}(K) = -jKV_\mathrm{e}^\mathrm{cart}(\mathbf{k})$, using the observation that dependency on the vector $\mathbf{k}$ occurs only through its norm, K. (Note also, to apply this trick, K is allowed to vary across the whole real line, including negative values).

3.3.2 Stage 2: Membrane Potential Calculation

Stage 2 of the volume conductor approach involves applying the calculated extracellular potential in stage 1 to the cable equation to compute the change in the membrane potential.

Using the cable equation, the membrane potential in the Fourier domain is given by

$$\mathring{V}_\mathrm{m} = -\frac{(\mathbf{k}\cdot\mathbf{u}_h)^2\lambda_V^2(w)}{1 + (\mathbf{k}\cdot\mathbf{u}_h)^2\lambda_V^2(w)}\mathring{V}_\mathrm{e}^\mathrm{cart}(\mathbf{k}). \tag{3.20}$$

This equation needs to be inverted from the Fourier domain to obtain the spatiotemporal pattern of the membrane potential. Details of deriving this equation is given in Chapter 2.

3.4 Far-field and Near-field Approximations

The far-field and near-field solutions derived here are both approximations of the standard volume conductor models in the regions, far and close to the electrode, respectively. Here, near-field indicates distances from the electrode much less than the frequency dependent (refer to equations (2.27) and (2.22)) electrotonic length constant for current density, $\lambda_J(w)$, while far-field means distance much greater than the frequency dependent electrotonic length constant for voltage, $\lambda_V(w)$. Both of these solutions consider tissue to be homogeneous and describe it with a constant conductivity.

To obtain a far-field approximation to equation (3.18), we consider $K > 0$ and adopt a Taylor series expansion around $K = 0$ for the $\tan^{-1}(\cdot)$ term. Thus, equation (3.18) is approximated as

$$\hat{\tilde{V}}_{\mathrm{e}}^{\mathrm{FF}} = \frac{\hat{\imath}(w)}{(2\pi)^2 \sigma_{\mathrm{FF}} K^2}, \tag{3.21}$$

in the far-field limit, where $\sigma_{\mathrm{FF}} = \dfrac{4}{3}\dfrac{d}{b\rho_{\mathrm{e}}} + \dfrac{1}{3\rho_{\mathrm{i}}}$ is the conductivity corresponding to the standard volume conductor model in this region.

The near-field approximation is achieved when $K \to \infty$. The resulting equation is similar to the far-field equation (3.21) but with a conductivity that is smaller than the far-field one by approximately an order of magnitude

$$\hat{\tilde{V}}_{\mathrm{e}}^{\mathrm{NF}} = \frac{\hat{\imath}(w)}{(2\pi)^2 \sigma_{\mathrm{NF}} K^2}, \tag{3.22}$$

where $\sigma_{\mathrm{NF}} = \dfrac{4}{3}\dfrac{d}{b\rho_{\mathrm{e}}}$.

The Fourier transform inversion of equations (3.14), (3.21), (3.22) were performed in MATLAB using the ifft function, via the inversion formula in equation (3.19). To avoid a numerical instability due to the singularity in these expressions at $K = 0$, we multiplied the expression by jK, (corresponding to differentiation wrt to R) performed the inverse

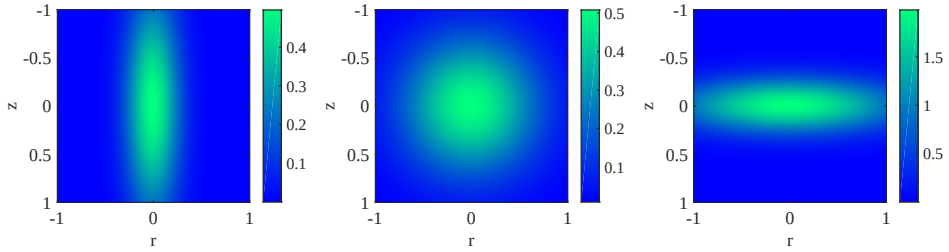

Figure 3.5: Gaussian distribution function. The figures refer to equation (3.23) with different values for $\frac{\gamma_r}{\gamma_z}$. From left to right 4, 1, 0.25.

Fourier transform, and then integrated the result wrt R to reverse the effect of the jK multiplication.

3.5 Extension to Three-Dimensional Gaussian Distribution of Fibers

In more realistic neural tissue, specific directions of fiber orientations might be more dominant. Therefore, in this section, we provide an extension to the proposed cellular composite model to account for this general case by introducing a Gaussian distribution function for fiber orientations in neural tissue.

A three-dimensional Gaussian distribution function is defined as

$$p(x,y,z) = \frac{1}{(2\pi)^{\frac{3}{2}}\gamma_r^2\gamma_z} e^{-\frac{x^2+y^2}{2\gamma_r^2} - \frac{z^2}{2\gamma_z^2}}. \tag{3.23}$$

which captures the orientation of fibers with different weights along (x,y) and z directions. In this equation, it is assumed that the standard deviation, γ_r, is the same for fibers in the (x,y) plane and is different from the standard deviation in the z direction, γ_z. This equation is then transformed to spherical coordinates and mapped into an ellipsoid with a unit radius. The ellipsoid is only dependent on the polar angle and can be written as

$$p_p(\phi) = \frac{\eta \sin\phi}{2\varrho^{\frac{3}{2}}(\phi)}, \quad 0 \leq \phi \leq \pi, \tag{3.24}$$

where $p_p(\phi)$ is the mapped Gaussian distribution function with

$$\begin{aligned} \varrho(\phi) &= \sin^2\phi + \eta^2\cos^2\phi, \\ \eta &= \frac{\gamma_r}{\gamma_z}. \end{aligned} \tag{3.25}$$

3.5.1 Extracellular Potential Calculation

A modified cellular composite model is rewritten as

$$\mathbf{J}_{\mathrm{e}}^{\mathrm{fb}} = -\frac{1}{2\pi}\xi_{\mathrm{e}} \underset{\mathbf{u},t}{*} \nabla V_{\mathrm{e}}, \tag{3.26}$$

$$\mathbf{J}_{\mathrm{e}} = \iint_{\theta,\phi} p_p(\phi)\mathbf{J}_{\mathrm{e}}^{\mathrm{fb}}\, d\theta\, d\phi, \tag{3.27}$$

$$\nabla \cdot \mathbf{J}_{\mathrm{e}} = 0, \tag{3.28}$$

to include the effect of the new probability function. In this set of equations, ξ_{e} is the admittivity kernel for the fibers with both spatial and temporal arguments and is a function of azimuth angle, θ, and polar angle, ϕ. $\mathbf{u}$ represents the unit vector parallel to a fiber axes. $\mathbf{J}_{\mathrm{e}}^{\mathrm{fb}}$ is the current density corresponding to the fibers oriented in the direction of $\mathbf{u}$.

To capture the effect of electrical stimulation on neural tissue with the aforementioned properties, we consider a point source electrode at the origin, combine the above equations and apply a four-dimensional Fourier transform to obtain

$$\iint_{\theta,\phi} p_p(\phi)\hat{\hat{\nabla}}^T\hat{\hat{\xi}}_{\mathrm{e}}\hat{\hat{\nabla}}\hat{\hat{V}}_e\, d\theta\, d\phi = \frac{-\hat{\imath}(w)}{(2\pi)^2}. \tag{3.29}$$

The extracellular potential is then given as

$$\hat{\hat{V}}_{\mathrm{e}} = \frac{-\hat{\imath}(w)}{(2\pi)^2 \iint_{\theta,\phi} p_p(\phi)\hat{\hat{\nabla}}^T\hat{\hat{\xi}}_{\mathrm{e}}\hat{\hat{\nabla}}\, d\theta\, d\phi}, \tag{3.30}$$

where the integral part contains the admittivity kernel to be computed. Some parts of this integral are calculated using Mathematica and a part is solved numerically as Mathematica was unable to generate the correct answer. Details of this calculation are given in Appendix E.

Table 3.1: Parameter Value

Parameter	b	d	ρ_i	ρ_e	R_{m}	τ_m
Value	1	0.05	1	1	0.1	1
Unit	μ m	μ m	Ω m	Ω m	Ω mˆ2	ms

3.6 Results

This section provides analytical and numerical results of our calculations for the extracellular potential. For the solutions of the standard volume conductor model, the analytic results are given whereas for the cellular composite model only numerical calculations in Matlab were possible.

3.6.1 Analytic Result for the Near-field and Far-field Approximations

The analytic results for homogeneous neural tissue in the near-field and the far-field regions are given in this section. As explained previously, these solutions are the result of approximating a spatiotemporal admittivity with a smooth and homogeneous conductivities.

By referring to equations (3.21), (3.22) and applying an inverse Fourier transform in spatial and temporal domains (which is explained in details in Appendix A) we obtain

$$V_{\mathrm{e}}^{\mathrm{NF}} = \frac{\iota(t)}{4\pi\sigma_{NF}R}, \tag{3.31}$$

which describes the near-field solution with the conductivity σ_{NF}. The far-field solution has a similar form with different conductivity, that is

$$V_{\mathrm{e}}^{\mathrm{FF}} = \frac{\iota(t)}{4\pi\sigma_{FF}R}. \tag{3.32}$$

3.6.2 Numerical Result

The result of our calculation for the extracellular potential of the cellular composite model and the standard volume conductor solutions in the near-field and far-field are sketched in Figure 3.7. The plots are obtained by applying a constant current input with an amplitude of 1 μA. To show that our numerical calculations produce correct prediction of the extracellular potential, we have plotted both analytic and numerical solutions for the near-field and far-field regions. The near-field analytic (red diamond points) and numerical (dashed pink line) solutions show a perfect matching to each other and we can see that the cellular composite solution in the near-field region, which is $< 10\mu$m, also matches with these plots. Similarly, for the far-field solution the analytic (blue star points) and numerical (dotted green lines) results fit together and the cellular composite solution in the far-field region, that is $> 300\mu$m, eventually matches with these solutions. However, in an intermediate-field we observe a transition in the cellular composite solution as a result of the frequency dependent admittivity that does not exist in the standard volume conductor solutions. According to our graph, the near-field region ($r \ll \lambda_{0J}$) ends at around 10 μm from the electrode which is around 6-7 times smaller than $\lambda_{0J} \approx 68\mu$m. The far-field region ($r \gg \lambda_{0V}$) starts at around 300 μm which is longer than $\lambda_{0V} \approx 200\mu$m. The values we obtained for the electrotonic length constants are based on the parameters in Table 3.1.

The second graph in this section shows the effect of pulse-width duration on the cellular composite prediction of the extracellular potential and the transition from the near-field to the far-field region. We have considered monophasic pulses of 10 μs, 100 μs and 1000 μs durations with an amplitude of 1 μA, as shown in Figure 3.6. The results are plotted in Figure 3.8 that demonstrates as the pulse-width increases the transition from the near-field to the far-field also increases. The reason behind this will be explained in the next section and is rooted in the frequency-dependent electrotonic length constants. In this figure, the light green, olive green and dark green are the cellular composite solutions under the pulse-widths of 10 μs, 100 μs and 1000μs, respectively. The near-field and far-field solutions are both independent of temporal frequency and are sketched in dashed pink and dotted black lines, respectively.

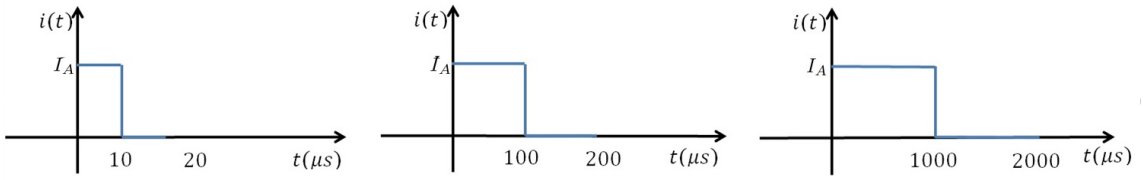

Figure 3.6: Monophasic current input with pulse-widths of 10 μs, 100 μs and 1000 μs durations, respectively.

3.7 Discussion

3.7.1 Near-field and Far-field regions

Comparing equations (3.33) and (3.34), we note that $|\lambda_V(w)| > |\lambda_J(w)|$. The near-field solution occurs when $r \ll |\lambda_J(w)|$ and the far-field solution occurs when $r \gg |\lambda_V(w)|$. In terms of the extracellular potential magnitude, the near-field solution is always an order of magnitude larger than the near-field counterpart. Alternatively, this can be explained through the conductivity magnitudes in the near-field and far-field regions. Comparing σ_{NF} with σ_{FF}, we realize that the far-field conductivity is an order of magnitude larger than the near-field conductivity. This effect can also be explained physically. That is, when the electrode is closer to the tissue there is less dissipation of the current density and the cells within tissue receive a more localized electrical stimulation. Since the resistivity in the near-field is higher, most of this current flow through the extracellular space whereas in the far-field region the current can access the low resistance intracellular space.

3.7.2 Pulse Width Effect

The change in the extracellular potential over a distance r from the electrode is described by the current density or voltage electrotonic length constants, λ_{0J} or λ_{0V}, respectively. If the input current density is a time-varying signal, such as monophasic or biphasic pulses, then the relative electrotonic length constants, as shown in Chapter 2, can be defined from

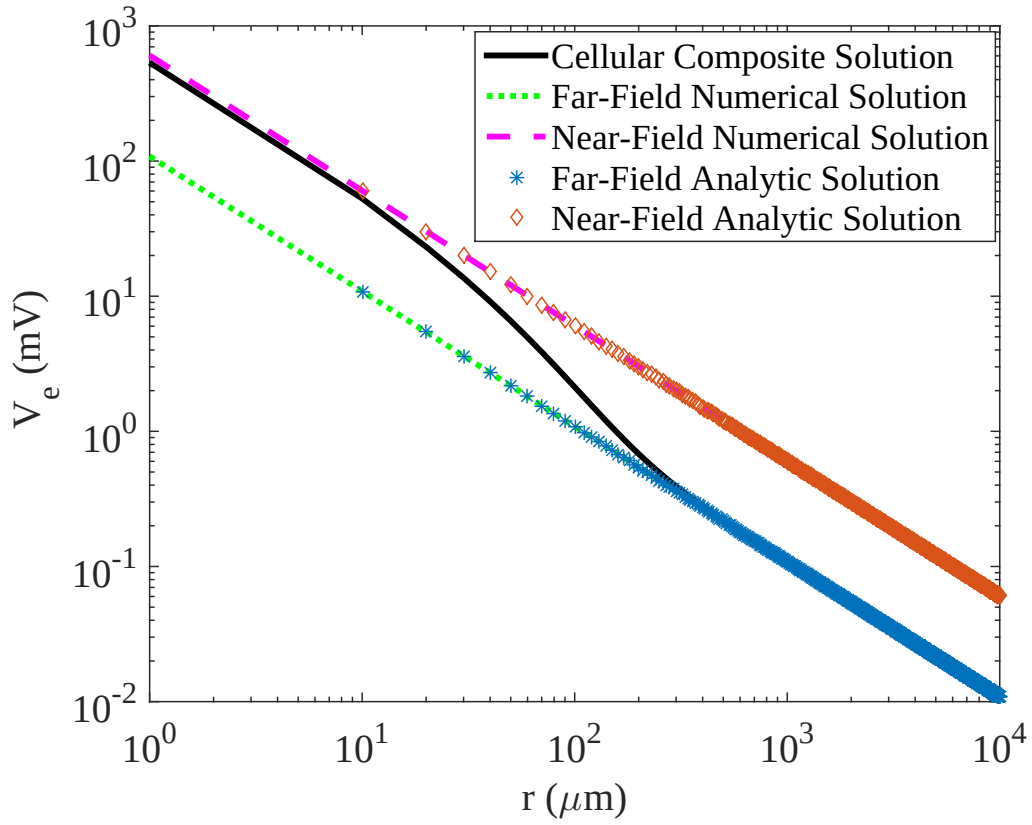

Figure 3.7: Black: Cellular composite numerical solution. Green: Far-field approximation using the Taylor series expansion around $K = 0$. Blue: The analytic solution for the far-field approximation. Magenta: Near-field approximation. This is the case when $K \to \infty$. Red: The analytic solution for the near-field approximation.

the membrane potential equation as

$$|\lambda_V(w)| = \frac{\lambda_{0V}}{\sqrt{|1 + jw\tau_m|}}, \tag{3.33}$$

$$|\lambda_J(w)| = \frac{\lambda_{0J}}{\sqrt{|1 + jw\tau_m|}}. \tag{3.34}$$

These equations clearly state that the cellular composite admittivity varies as the pulse width changes. In other words, as the pulse width becomes longer, the dominant temporal frequency in the pulse spectrum becomes smaller. Therefore, $|\lambda_V(w)|$ and $|\lambda_J(w)|$ both increase. Hence, the transition point from the near-field to the far-field increases. An alternative explanation is that shorter pulse-widths correspond to a higher temporal

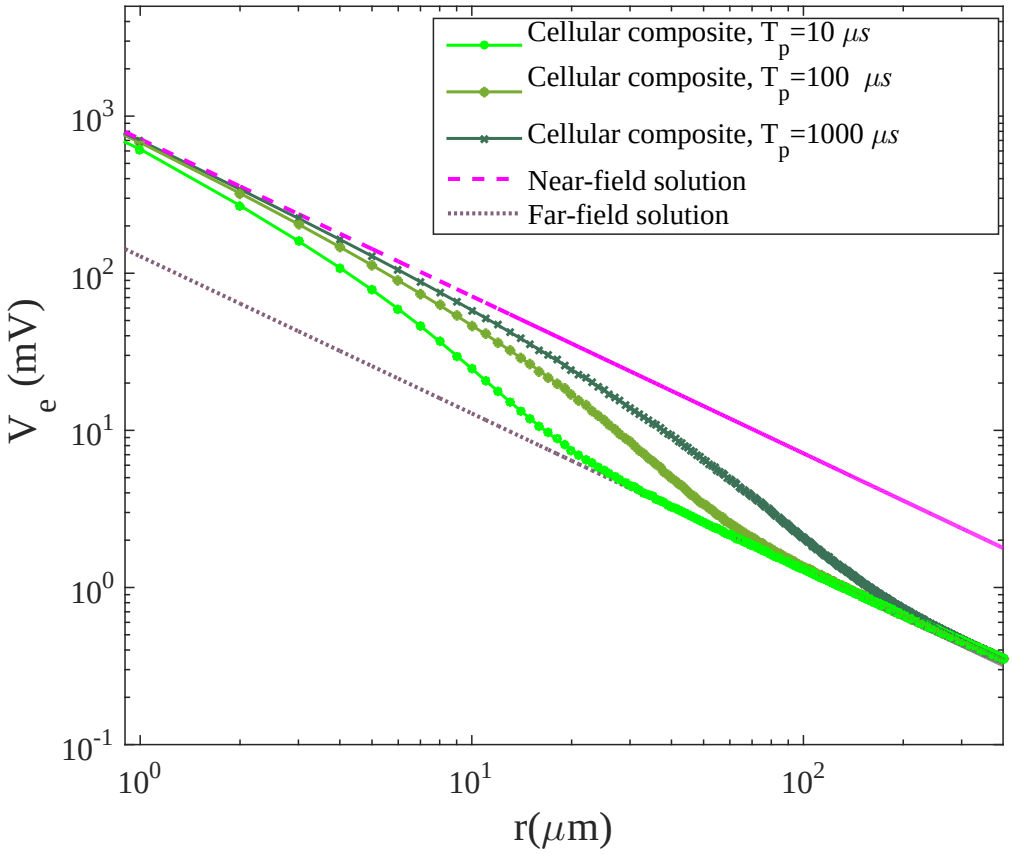

Figure 3.8: Pulse-width effect at time value $t = T_p$. Greens belong to the cellular composite solutions. Pink is the near-field solution and dotted black is the far-field solution.

frequency. A higher temporal frequency means a larger w which indicates the values in equations (3.33) and (3.34) both decrease. This results in a shorter transition between the near-field to the far-field regions.

In order to see the effect of the pulse-width on the membrane potential, we can apply the extracellular potential results to the cable equation. Our expectation is to see a more widespread neural activation for longer pulse-widths compared to shorter ones.

3.7.3 Conclusion

In this chapter, we modeled the effect of a point source electrical stimulation in an isotropic neural tissue composed of crossing fibers. Under the assumption of equally oriented

fibers in all directions, we derived the tissue admittivity to replace the purely smooth and homogeneous conductivity in the standard volume conductor approach. We then calculated the extracellular potential using the cellular composite model [Meffin et al., 2014]. The results were compared to the solutions of a standard volume conductor model in the near- and far-field regions. The physical intuition behind our calculation was to take into account the effective resistance of tissue, which is higher close to the electrode. This is due to the current being forced to pass through the tightly packed extracellular space, a fact that has not been taken into account in the conventional model. Taking advantage of the cellular composite model, we demonstrated how the cellular geometry affected the spatial profile of extracellular and (subthreshold) membrane potential. As a result, we found a range of electrode-neurite separations over which neither approximations (near- or far-field) were able to be applied. This range ($10 - 300\mu m$) is common in neuroprosthetic and electrophysiological applications.

We also considered the effect of stimulation parameter, i.e. monophasic pulse with different pulse-width durations and explained that with an increase in the pulse-width, the distance between the near-field and the far-field regions increases.

Furthermore, we showed theoretically how to incorporate more complicated fiber orientation distribution in our modeling to mimic more realistic neural tissue. Our calculations were performed using a Gaussian distribution of fibers orientations, however, it is not restricted to that. In a special case where the standard deviations are the same in all directions, our solution for the uniform distribution is recovered from the Gaussian distribution equations.

There have been several experimental studies such as [Histed et al., 2009, Joucla and Yvert, 2012] that observed tissue activation was usually more widespread than the models typically predicted. However, Histed et al., 2009 suggested that the wide and sparse spread of activation observed in cell bodies is due to stimulation of axons of passage passing close ($< 15\mu$m) from the micro-electrode. Hence, models may accurately predict activation provided detailed information about passing axons is available.

Chapter 4

Anisotropic Tissues with Laminar Structure

IN the previous chapter, we modeled the effect of electrical stimulation in tissues with stellate structures such as the CA3 region of the hippocampus. We continue developing our framework in this chapter for tissues with laminar structure such as retina and the neo-cortex. The layered configuration of a retina is shown in Figure 4.1. Different cell types exist across different layers. Within each layer, cells are mainly parallel to each other and create a cascade connection with other cells across different layers for transmission of information.

Another example of laminar structures is the neo-cortex. The cortex has an intricate structure in terms of fiber orientations, geometry and electrical properties along its six layers. The cells in the cortex are intermingled together with a feedback connection between them. Figure 4.2(a) shows an image of a cortical column with pyramidal cells occupying a major proportion of tissue. Figure 4.2(b) is an intuitive depiction of the orientation of fibers in different layers of cortex based on diffusion magnetic resonance imaging (MRI) study on human cadaver [Leuze et al., 2014]. For simplicity the six layers of the cortex are combined into four laminae based on the cell popularity in each layer. In laminae 2 and 4, the majority of cells are of pyramidal type whereas in lamina 3 spiny stellate cells are more prevalent. Lamina 1, which is the molecular layer, mainly consists of axons and dendrites form cells in other layers. In each lamina, the orientation distribution is shown either in circles for stellate like distributions or in ellipsoids for laminar orientation distribution.

Other examples of fibers oriented in a plane in a layered structure are auditory and

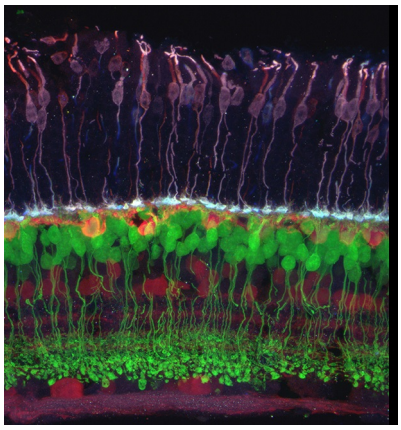

Figure 4.1: Microscopic image of retina. Source http://wonglab.biostr.washington.edu.

visual thalamic nuclei. Structures like this are very common throughout the nervous system.

Since the cells in a laminar structure are preferentially oriented within a plane and lack any fiber oriented perpendicular to the plane, we expect to see some anisotropic effect. The main focus of this chapter is to show this behavior through our modeling framework.

Similar to Chapter 3, we assume a uniform distribution of fiber orientations, however, only within a plane (circularly symmetric structure). Based on this structure, the admittivity kernel and the extracellular potential are calculated. The analytical result is then extended to a case where the orientations of fibers follow a Gaussian distribution function. This case gives some flexibility in terms of having some directions of fibers away from a specific direction. Finally, calculations for a double layer inhomogeneous and anisotropic tissue is given to accommodate for a more general structure.

4.1 Methods

In this section, we briefly summarize the standard volume conductor approach solved for laminar tissue with circularly symmetric fiber orientation and then introduce the cellular composite equivalent.

(a) (b)

Figure 4.2: (b). Cortical columns. Source: http://www.gregadunn.com/ (b) Illustration of orientation distribution in different lamina of the cortex based on the work in [Leuze et al., 2014].

4.1.1 Standard Volume Conductor Approach

For a homogeneous tissue the voltage distribution in the extracellular space due to a point source electrode is written as

$$\nabla^2 V_{\mathrm{e}} = -\frac{\iota(t)\delta(x)\delta(y)\delta(z)}{\sigma}, \tag{4.1}$$

where $\delta(\cdot)$ is a Dirac delta function and $\iota(t)$ is the injected current from the electrode. By applying a two-dimensional Fourier transform in (x, y), we obtain the ordinary differential equation

$$\frac{\partial^2 \hat{\hat{V}}_{\mathrm{e}}}{\partial z^2} - k_r^2 \hat{\hat{V}}_{\mathrm{e}} = -\frac{\hat{\iota}(\omega)\delta(z)}{2\pi\sqrt{2\pi}\sigma}. \tag{4.2}$$

in which $k_r^2 = k_x^2 + k_y^2$ and k_x and k_y are the spatial Fourier variable corresponding to x and y, respectively.

Assuming the potential is bounded at infinity, the solution to this differential equation is

$$\hat{\hat{V}}_{\mathrm{e}} = \frac{\hat{\iota}(w)}{4\pi\sqrt{2\pi}\sigma|k_r|} e^{-|k_r||z|}. \tag{4.3}$$

4.1.2 Cellular Composite Model: Uniform Planar Distribution of Fibers

The generalized cellular composite model of neural tissue with fiber orientation distribution $p(\cdot)$ is described by a set of equations

$$\mathbf{J}_{\mathrm{e},\alpha} = -\frac{1}{2\pi}\xi_{\mathrm{e},\alpha} \underset{\mathbf{u}_\alpha,t}{*} \nabla V_{\mathrm{e}}, \tag{4.4}$$

$$\mathbf{J}_{\mathrm{e}} = \int_\alpha p(\alpha)\mathbf{J}_{\mathrm{e},\alpha} d\alpha, \tag{4.5}$$

$$\nabla \cdot \mathbf{J}_{\mathrm{e}} = 0, \tag{4.6}$$

where α describes angles of orientation of fibers. The spatial convolution is taken in the direction of fibers with orientation α and captures the effect of current paths between points in the extracellular spaces via the intracellular space; refer to Definition 2 in Chapter 3. The capacitive property of the membrane leads to the time convolution, which relates the current density to the extracellular electrical field at previous times. $\mathbf{J}_{\mathrm{e}}$ is the mean extracellular current density of tissue. $\mathbf{u}_\alpha$ is the unit vector parallel to a fiber (cylinder) main axis. This structure is shown in Figure 4.3. In this configuration, a point source electrode is placed at the origin. Neural tissue is located in xy plane and fibers are oriented evenly in every direction. Cylindrical models of fibers are shown in red with yellow arrows showing the direction of that fiber ($\mathbf{u}_\alpha$).

The admittivities are calculated from the trans-impedance equations for a single neurite and are expressed in the Fourier domain as

$$\hat{\hat{\xi}}_{\mathrm{e},\alpha}(\mathbf{k},\omega:\mathbf{u}_\alpha) = \hat{\hat{\xi}}_{\mathrm{e,T}} I_3 + (\hat{\hat{\xi}}_{\mathrm{e,L}}(\mathbf{k},\omega:\mathbf{u}_\alpha) - \hat{\hat{\xi}}_{\mathrm{e,T}})\mathbf{u}_\alpha \mathbf{u}_\alpha^T, \tag{4.7}$$

$$\hat{\hat{\xi}}_{\mathrm{e,T}} = \frac{d}{b\rho_{\mathrm{e}}}, \tag{4.8}$$

$$\hat{\hat{\xi}}_{\mathrm{e,L}}(\mathbf{k},\omega:\mathbf{u}_\alpha) = \frac{1}{\rho_{\mathrm{i}}}\frac{1+j\omega\tau_m+(\mathbf{k}\cdot\mathbf{u}_\alpha)^2\lambda_{0I}^2}{1+j\omega\tau_m+(\mathbf{k}\cdot\mathbf{u}_\alpha)^2\lambda_{0V}^2}, \tag{4.9}$$

to capture some properties of the fibers such as their orientation, diameter, and membrane properties. In the admittivity equation, $\hat{\hat{\xi}}_{\mathrm{e,T}}$ and $\hat{\hat{\xi}}_{\mathrm{e,L}}(\mathbf{k},\omega)$ are the transverse and longitudinal components of the admittivity $\hat{\hat{\xi}}_{\mathrm{e},\alpha}(\mathbf{k},\omega)$. $I_{3\times3}$ is the 3×3 identity matrix. $\mathbf{u}_\alpha\mathbf{u}_\alpha^T$ is an outer product where $\mathbf{u}_\alpha^T$ defines the transpose vector of $\mathbf{u}_\alpha$. τ_m is the mem-

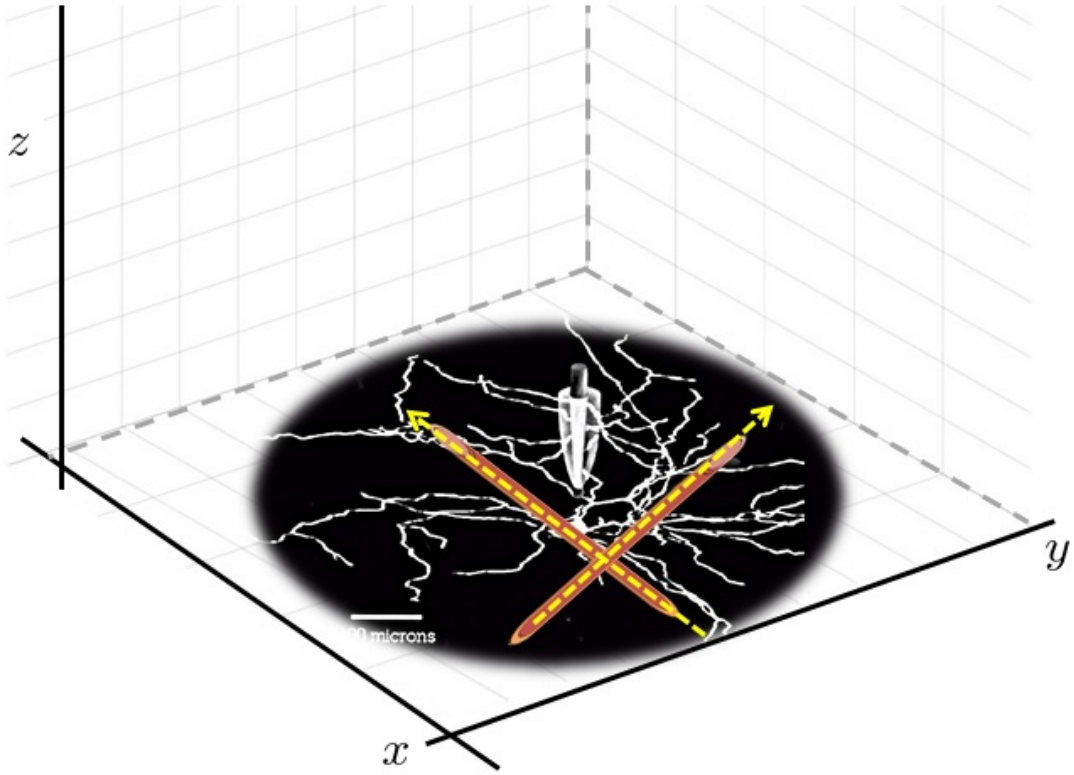

Figure 4.3: Laminar neural tissue structure. Fibers are oriented uniformly in xy plane and the electrode is placed at the origin.

brane time constant. ρ_e and ρ_i are the extracellular and intracellular resistivities of tissue, respectively. b is the radius of an ideal cylindrical neurite and d is the thickness of the extracellular sheath (equal to half the width of the extracellular space between neighboring cells). λ_{0J} and λ_{0V} are the electrotonic length constants calculated under current density and voltage boundary conditions for the cable equation [Meffin et al., 2012] respectively, and can be expressed in terms of fiber physical parameters,

$$\begin{aligned} \lambda_{0J}^2 &= \frac{r_m}{r_e + r_i}, \\ \lambda_{0V}^2 &= \frac{r_m}{r_i}, \end{aligned} \tag{4.10}$$

where $r_m = \dfrac{R_m}{2\pi b}$ is the membrane per unit length resistance. R_m is the membrane per unit area resistance. $r_e \approxeq \dfrac{\rho_e}{2\pi b d}$ is the extracellular resistance per unit length and $r_i \approxeq \dfrac{\rho_i}{\pi b^2}$

is the intracellular resistance per unit length.

4.1.3 Admittivity Calculation

For a laminar structure with infinitely many fibers, the admittivity can be computed in the Fourier domain as

$$\begin{aligned}\hat{\hat{\xi}}_{\mathrm{e}} &= \int_{\alpha} d\alpha \hat{\hat{\xi}}_{\mathrm{e},\alpha}(\mathbf{k},\omega) \\ &= \int_{\alpha} d\alpha \hat{\hat{\xi}}_{\mathrm{e,T}}(I_{3\times 3} - u_\alpha u_\alpha^T) \\ &\quad + \int_{\alpha} d\alpha \left(\frac{1}{\rho_{\mathrm{i}}} \frac{1 + j\omega\tau_m + (\mathbf{k}\cdot\mathbf{u}_h)^2\lambda_{0J}^2}{1 + j\omega\tau_m + (\mathbf{k}\cdot\mathbf{u}_h)^2\lambda_{0V}^2} u_\alpha u_\alpha^T \right).\end{aligned} \tag{4.11}$$

The solutions to these integrals have a form

$$\hat{\hat{\xi}}_{\mathrm{e}} = \begin{bmatrix} \hat{\hat{\xi}}_{\mathrm{e},r} & 0 \\ 0 & \hat{\hat{\xi}}_{\mathrm{e},z} \end{bmatrix}, \tag{4.12}$$

where $\hat{\hat{\xi}}_{\mathrm{e},r}$ is a 2×2 block matrix describing the admittivity in the r-direction

$$\begin{aligned}\hat{\hat{\xi}}_{\mathrm{e,r}} = \begin{bmatrix} \hat{\hat{\xi}}_{\mathrm{e}_{11}} & \hat{\hat{\xi}}_{\mathrm{e}_{12}} \\ \hat{\hat{\xi}}_{\mathrm{e}_{21}} & \hat{\hat{\xi}}_{\mathrm{e}_{22}} \end{bmatrix} &= \left(\frac{1}{2}\hat{\hat{\xi}}_{\mathrm{e,T}} + \frac{1}{2\rho_i}\frac{\lambda_{0J}^2}{\lambda_{0V}^2} \right) \begin{bmatrix} 1 & 0 \\ 0 & 1 \end{bmatrix} \\ &\quad + \frac{1}{\rho_i} \frac{(1 - \frac{\lambda_{0J}^2}{\lambda_{0V}^2}) f^2(k_r)}{\lambda_V^2(w) k_r^4 \sqrt{1 + \lambda_V^2(w) k_r^2}} \begin{bmatrix} k_y^2 & -k_x k_y \\ -k_x k_y & k_x^2 \end{bmatrix} \\ &\quad - \frac{1}{\rho_i} \frac{(1\frac{\lambda_{0J}^2}{\lambda_{0V}^2}) f(k_r)}{\lambda_V^2(w) k_r^4 \sqrt{1 + \lambda_V^2(w) k_r^2}} \begin{bmatrix} k_r^2 & 0 \\ 0 & k_r^2 \end{bmatrix},\end{aligned} \tag{4.13}$$

in which $f(k_r) = 1 - \sqrt{1 + \lambda_V^2(w)k_r^2}$. The second diagonal element in equation (4.12) is the admittivity in the z-direction and is defined as

$$\hat{\hat{\xi}}_{\mathrm{e},z} = \hat{\hat{\xi}}_{\mathrm{e,T}}. \tag{4.14}$$

Although there is no fiber oriented in the z-direction, this admittivity is the result of stacking planar tissues on top of each other in a homogeneous medium. By analyzing equation (4.12) and calculating the eigenvalues and eigenvectors of the second matrix on the right hand side of equation (4.13), we find

$$\begin{aligned} s_1 &= 0, \quad v_1 = [k_x, k_y]^T, \\ s_2 &= k_r^2, \quad v_2 = [k_y, -k_x]^T. \end{aligned} \tag{4.15}$$

Physically, the second eigenvalue-eigenvector pair is irrelevant, as later we will show that the vector we use to perform our calculation is of the form of v_1.

Definition 3. *A matrix, M, is rotationally symmetric if and only if*

$$M = RMR^T, \tag{4.16}$$

where $R = \begin{bmatrix} \cos\theta & -\sin\theta \\ \sin\theta & \cos\theta \end{bmatrix}$ *is the rotation matrix.*

According to this definition, it can be easily checked that the submatrix $\hat{\hat{\xi}}_{\mathrm{e,r}}$ is rotationally symmetric. This can be further extended to the whole matrix $\hat{\hat{\xi}}_{\mathrm{e}}$.

This confirms our assumption on the orientation distribution of fibers and having an isotropic structure within each plane modeling neural tissue.

4.1.4 Extracellular Potential Calculation

The extracellular potential for a point source electrode can be calculated by combining equations (4.4)-(4.6)

$$\frac{1}{2\pi}\nabla \cdot \Big(\int_\alpha p(\alpha)\xi_{\mathrm{e},\alpha} d\alpha \underset{\mathbf{u}_\alpha, t}{*} \nabla V_{\mathrm{e}} \Big) = -\iota(t)\delta(x)\delta(y)\delta(z), \tag{4.17}$$

where $u_\alpha = [\cos\theta, \sin\theta, 0]^T$ determines the fiber orientation in a laminar tissue.

Assumption 2. *Neural tissue can be modeled as a stack of planes on top of each other with continuum fibers uniformly distributed in every direction within each plane.*

Under assumption 2, $p(\alpha) = 1/2\pi$ that is equivalent to the surface of a unit circle. To simplify the calculations, a two-dimensional Fourier transform in (x, y) and a one-dimensional in time are applied to both sides of equation (4.17),

$$\check{\nabla}^T \int_\alpha \hat{\hat{\xi}}_{e,\alpha} d\alpha \check{\nabla} \check{V}_e = \frac{-\hat{\imath}(w)}{2\pi\sqrt{2\pi}} \delta(z), \tag{4.18}$$

where $\check{\nabla} = [jk_x, jk_y, \frac{\partial}{\partial z}]$. Replacing $\hat{\hat{\xi}}_{e,\alpha}$ with the definition in equation (4.7) and arranging different terms, an ordinary differential equation in z is given,

$$c_1 \frac{\partial^2 \hat{\check{V}}_e}{\partial z^2} - c_2 \check{V}_e = \frac{-\hat{\imath}(w)}{2\pi\sqrt{2\pi}} \delta(z), \tag{4.19}$$

where $\mathbf{k} = [k_x, k_y, 0]$, and

$$\begin{aligned} c_1 &= \int_\alpha \hat{\hat{\xi}}_{e,T} d\alpha, \\ c_2 &= \int_\alpha \hat{\hat{\xi}}_{e,T} (k_r^2 - (\mathbf{k}\cdot\mathbf{u}_\alpha)^2) d\alpha \\ &\quad + \int_\alpha \left(\frac{1}{\rho_i} \frac{1 + j\omega\tau_m + (\mathbf{k}\cdot\mathbf{u}_\alpha)^2 \lambda_{0J}^2}{1 + j\omega\tau_m + (\mathbf{k}\cdot\mathbf{u}_\alpha)^2 \lambda_{0V}^2} \right) (\mathbf{k}\cdot\mathbf{u}_\alpha)^2 d\alpha. \end{aligned} \tag{4.20}$$

The integral over the orientation in equation (4.20) can be performed to give the analytical solutions

$$\begin{aligned} c_1 &= \hat{\hat{\xi}}_{e,T} = \hat{\hat{\xi}}_{e,z}, \\ c_2 &= \left(\frac{1}{2} \hat{\hat{\xi}}_{e,T} + \frac{1}{2\rho_i} \frac{\lambda_{0J}^2}{\lambda_{0V}^2} \right) k_r^2 \\ &\quad + \frac{1}{\rho_i} \frac{(1 - \frac{\lambda_{0J}^2}{\lambda_{0V}^2})}{\lambda_V^2} \left(1 - \frac{1}{\sqrt{1 + \lambda_V^2 (k_r^2)}} \right) = k_r^T \hat{\hat{\xi}}_{e,r} k_r, \end{aligned} \tag{4.21}$$

where $k_r^2 = (k_x^2 + k_y^2)$.

Please note that parameters c_1 and c_2 are only introduced for mathematical calcula-

tions. We replace these parameters with more physically meaningful parameters $\hat{\hat{\xi}}_{e,z}$ and $k_r^T \hat{\hat{\xi}}_{e,r} k_r$ in the extracellular potential equation.

Subsequently, the solution to the second order differential equation with constant coefficients is calculated as

$$\hat{\hat{V}}_e(k_r, w, z) = \frac{-\hat{\imath}(w)}{4\pi\sqrt{2\pi}\sqrt{k_r^T \hat{\hat{\xi}}_{e,z} \hat{\hat{\xi}}_{e,r} k_r}} \left(e^{-\hat{\hat{\chi}}(k_r,w)z} - e^{\hat{\hat{\chi}}(k_r,w)z} \right) u(z) + k_1 e^{\hat{\hat{\chi}}(k_r,w)z} + k_2 e^{-\hat{\hat{\chi}}(k_r,w)z}, \tag{4.22}$$

where

$$\hat{\hat{\chi}}(k_r, w) = \sqrt{k_r^T \frac{\hat{\hat{\xi}}_{e,r}}{\hat{\hat{\xi}}_{e,z}} k_r}, \tag{4.23}$$

is a measure of anisotropy, $u(z)$ is the Heaviside step function, and k_1 and k_2 are to be found through the choice of boundary conditions. As it is assumed that the fibers are infinitely long, the voltage at infinity, i.e., $\lim_{z\to\pm\infty} \hat{\hat{V}}_e < \infty$, should be finite. Given equation (4.22), to satisfy the condition at $z \to \infty$, we choose $k_1 = \hat{\imath}(w)/4\pi\sqrt{2\pi}\sqrt{k_r^T \hat{\hat{\xi}}_{e,z} \hat{\hat{\xi}}_{e,r} k_r}$. In order to have a finite potential when $z \to -\infty$, $k_2 = 0$. Therefore, equation (4.22) is simplified to

$$\hat{\hat{V}}_e(k_r, w, z) = \frac{-\hat{\imath}(w)}{4\pi\sqrt{2\pi}\sqrt{k_r^T \hat{\hat{\xi}}_{e,z} \hat{\hat{\xi}}_{e,r} k_r}} \left(e^{-\hat{\hat{\chi}}(k_r,w)|z|} \right). \tag{4.24}$$

This is the Fourier domain extracellular potential, which will be inverted numerically and figures will be shown in the Results section.

4.2 Near-field and Far-field Approximations of Cellular Composite Model

The cellular composite solution in equation (4.24) can be approximated in the near-field and the far-field regions by a constant conductivity. The near-field approximation describes the behavior of neurons close to the electrode where $r \ll \lambda_J(w)$, and the far-field approximation describes their behavior at distances where $r \gg \lambda_V(w)$. The main difference between these approximations and the cellular composite solution is in the coeffi-

cient c_2

$$\begin{aligned} c_2^{\mathrm{NF}} &= \left(\frac{1}{2}\hat{\hat{\xi}}_{\mathrm{e,T}} + \frac{1}{2\rho_i}\frac{\lambda_{0J}^2}{\lambda_{0V}^2}\right) k_r^2 = \sigma_r^{\mathrm{NF}} k_r^2, \\ c_2^{\mathrm{FF}} &= \left(\frac{1}{2}\hat{\hat{\xi}}_{\mathrm{e,T}} + \frac{1}{2\rho_i}\right)(k_x^2 + k_y^2) = \sigma_r^{\mathrm{FF}} k_r^2, \end{aligned} \tag{4.25}$$

where c_2^{NF} and c_2^{FF} are the near- and far-field approximations of c_2, respectively.

Replacing these coefficients into equation (4.24) and applying an inverse Fourier transform, the analytic solution can be computed as

$$V_{\mathrm{e}}(x,y) = \frac{\iota(t)}{4\pi\sqrt{\sigma_r\sigma_z r^2 + \sigma_r^2 z^2}}, \tag{4.26}$$

where $r = \sqrt{x^2+y^2}$ and σ_r, σ_z are constant conductivities which are given in the near- and far-field regions as

$$\begin{aligned} \sigma_r^{\mathrm{NF}} &= \frac{1}{2}\hat{\hat{\xi}}_{\mathrm{e,T}} + \frac{1}{2\rho_i}\frac{\lambda_{0J}^2}{\lambda_{0V}^2}, \\ \sigma_z^{\mathrm{NF}} &= \hat{\hat{\xi}}_{\mathrm{e,T}}, \end{aligned} \tag{4.27}$$

$$\begin{aligned} \sigma_r^{\mathrm{FF}} &= \frac{1}{2}\hat{\hat{\xi}}_{\mathrm{e,T}} + \frac{1}{2\rho_i}, \\ \sigma_z^{\mathrm{FF}} &= \hat{\hat{\xi}}_{\mathrm{e,T}}. \end{aligned} \tag{4.28}$$

4.3 Extension to a Distribution of Fiber Orientations Based on the Gaussian Distribution

In realistic tissue, fibers are not necessarily oriented uniformly. This means fibers in a specific direction may outnumber fibers in other directions. To account for this fact in laminar tissue we assume different standard deviations in the x and y directions. Based on this assumption, a corresponding orientation distribution function $p(\alpha)$, and hence the extracellular potential are calculated.

A two-dimensional Gaussian distribution function in (x,y) can be expressed as

$$p(x,y) = \frac{1}{2\pi\gamma_x\gamma_y} e^{\left(-\frac{x^2}{2\gamma_x^2} - \frac{y^2}{2\gamma_y^2}\right)}, \tag{4.29}$$

where γ_x and γ_y are the standard deviations in the x and y directions, respectively.

To capture different orientations of fibers, this function is transformed into a polar coordinates by choosing $x = r\cos\theta$ and $y = r\sin\theta$

$$p(r,\theta) = \frac{1}{2\pi\gamma_x\gamma_y} e^{r^2\left(-\frac{\cos\theta^2}{2\gamma_x^2} - \frac{\sin\theta^2}{2\gamma_y^2}\right)}. \tag{4.30}$$

This function is then mapped onto an ellipsoid around the origin to remove the dependency on the fiber distances from the origin. This can be done by performing integration over r from zero to infinity

$$p_p(\theta) = \frac{\eta}{\pi(\cos^2\theta + \eta^2\sin^2\theta)}, \tag{4.31}$$

where $\eta = \dfrac{\gamma_x}{\gamma_y}$.

4.3.1 Extracellular Potential Calculation

To calculate the extracellular potential for fibers oriented at an angle θ, the cellular composite equations are modified to

$$\mathbf{J}_\mathrm{e}^\theta = -\frac{1}{2\pi}\xi_{\mathrm{e},\theta} \underset{\mathbf{u}_\theta,t}{*} \nabla V_\mathrm{e}, \tag{4.32}$$

$$\mathbf{J}_\mathrm{e} = \int_\theta p_p(\theta)\mathbf{J}_\mathrm{e}^\theta d\theta, \tag{4.33}$$

$$\nabla\cdot\mathbf{J}_\mathrm{e} = 0, \tag{4.34}$$

where $\xi_{\mathrm{e},\theta}$ is the admittivity kernel for the fibers with both spatial and temporal arguments and is a function of angle, θ. $\mathbf{u}_\theta$ represents the unit vector parallel to a fiber axis. $\mathbf{J}_\mathrm{e}^\theta$ is the current density corresponding to the fiber oriented at the angle θ.

The calculation is very similar to the previous section. However, coefficients c_1 and c_2

in equation (4.19) take new forms as

$$
\begin{aligned}
c_1 &= \int_\theta \frac{\hat{\hat{\xi}}_e \eta}{\pi(\cos^2\theta + \eta^2 \sin^2\theta)} d\theta, \\
c_2 &= \int_\theta \frac{\hat{\hat{\xi}}_e \eta}{\pi(\cos^2\theta + \eta^2 \sin^2\theta)} (K^2 - (\mathbf{k}\cdot\mathbf{u}_\theta)^2) d\theta \\
&\quad + \int_\theta \frac{\eta}{\pi\rho_i(\cos^2\theta + \eta^2 \sin^2\theta)} \frac{1+\lambda_I^2(\mathbf{k}\cdot\mathbf{u}_\theta)^2}{1+\lambda_V^2(\mathbf{k}\cdot\mathbf{u}_\theta)^2} d\theta.
\end{aligned} \tag{4.35}
$$

Solving these integrals using Maple or Mathematica software, we obtain

$$
\begin{aligned}
c_1 =& \xi_{\mathrm{e,T}} = \xi_{\mathrm{e},z}, \\
c_2 =& \xi_{\mathrm{e,T}} \frac{k_x^2 + \eta k_y^2}{1+\eta} + \frac{\lambda_{0I}^2}{\lambda_{0V}^2} \frac{\eta k_x^2 + k_y^2}{\rho_i(1+\eta)} + \frac{(1 - \frac{\lambda_{0I}^2}{\lambda_{0V}^2})}{\rho_i \lambda_V^2} \times \Bigg(1 - \\
& \frac{\eta\left(\eta\lambda_V^2\left((f(\eta))\left(k_x^2 - k_y^2\right) + \lambda_V^2 k_r^2\left(\eta^2 k_x^2 + k_y^2\right)\right)\right)}{Den} \\
& + \frac{\eta\left(f(\eta)\left(\eta^2 - 1 + \lambda_V^2\left(\eta^2 k_x^2 - k_y^2\right)\right)\sqrt{1+\lambda_V^2 k_r^2}\right)}{Den} \Bigg),
\end{aligned} \tag{4.36}
$$

where $f(\eta) = \eta^2 - 1$ and

$$
\begin{aligned}
Den =& \sqrt{1+\lambda_V(w)^2 k_r^2}\Big[f(\eta)^2 + 2 f(\eta)\lambda_V(w)^2\left(\eta^2 k_x^2 - k_y^2\right) \\
& + \lambda_V(w)^4\left(\eta^2 k_x^2 + k_y^2\right)^2 \Big].
\end{aligned} \tag{4.37}
$$

According to these equations, one can choose appropriate distribution proportion, η, to obtain the extracellular potential solution in the Fourier domain. In a special case of $\eta = 1$, equation (4.21) for c_2 is recovered. Once the Fourier domain solution is inverted numerically, the extracellular potential is obtained.

4.4 Electrical Stimulation in a two-layer inhomogeneous neural tissue

Laminar tissues might contain layers with different cell types, fiber orientations and electrical properties. An example of this can be the retina or the cortex with different cell properties and conductivities in each layer. In this section, a guideline on connecting layered neural tissues with appropriate boundary conditions is provided to account for inhomogeneous and anisotropic neural tissue. Figure 4.4 illustrates this situation graphically. The electrode is placed close to the neural tissue in layer A within a distance from the boundary. Layers are assumed to have different conductivities. Each layer can contain different tissue structure with different electrical properties, i.e., tissue with stellate or laminar distribution of fibers or a fiber bundle or an insulation layer such as air.

Although the framework is very similar to that in the previous section, the idea of choosing appropriate boundary conditions between each layer is novel.

We start the modeling by introducing the volume conductor solution and then explain the more complicated cellular composite modeling approach.

4.4.1 Standard Volume Conductor Approach

Consider a two-layer neural tissue with different conductivities in each layer as shown in Figure 4.4. The point source electrode is located at distance h from the origin in the z direction in layer A. The conductivity of layers A and B are described by σ_A and σ_B, respectively. The objective is to apply the volume conductor approach using appropriate boundary conditions at each layer to find the effect of electrical stimulation.

Standard volume conductor equations for layer A are expressed as

$$\begin{aligned} \mathbf{J}_{\mathrm{e}} &= -\sigma_A \nabla V_{\mathrm{e}}^A, \\ \nabla \cdot \mathbf{J}_{\mathrm{e}} &= \iota(t)\delta(x)\delta(y)\delta(z-h), \end{aligned} \tag{4.38}$$

where the effect of the electrode is reflected in the Dirac delta function $\delta(\cdot)$ in the z-direction.

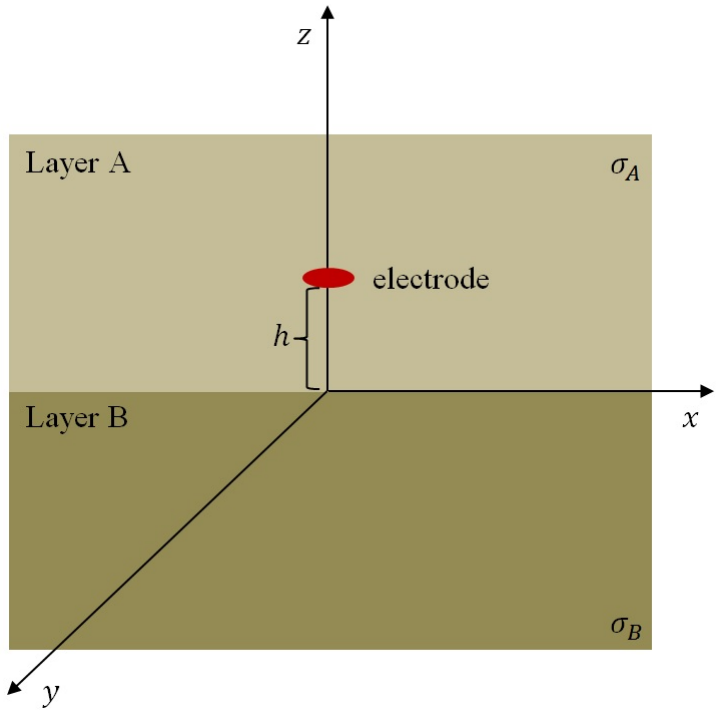

Figure 4.4: A two-layer electrode-tissue configuration.

The two equations are then combined to give the Poisson equation

$$\nabla^2 V_{\mathrm{e}}^A = -\frac{\iota(t)\delta(x)\delta(y)\delta(z-h)}{\sigma_A}, \tag{4.39}$$

which in the Fourier domain is represented as

$$\frac{\partial^2 \hat{\hat{V}}_{\mathrm{e}}^A}{\partial z^2} - k_r^2 \hat{\hat{V}}_{\mathrm{e}}^A = -\frac{\hat{\iota}(w)\delta(z-h)}{2\pi\sigma_A}, \tag{4.40}$$

where $k_r^2 = (k_x^2 + k_y^2)$.

The solution to the differential equation is calculated as

$$\begin{aligned} \check{\hat{V}}_{\mathrm{e}}^A &= k_1 e^{-|k_r|z} + k_2 e^{|k_r|z} \\ &\quad -\frac{\hat{\iota}(w)}{4\pi\sigma_A|k_r|}\left(e^{|k_r|(z-h)} - e^{-|k_r|(z-h)}\right)u(z-h), \end{aligned} \tag{4.41}$$

where k_1 and k_2 are constants to be found using the boundary conditions and $u(\cdot)$ is the Heaviside step function. To find k_1 and k_2, we use the assumption that the extracellu-

lar potential at infinity should be zero and also should be continuous at the boundary between layers. Using the first assumption, we find $k_2 = \frac{\hat{\imath}(w)e^{-|k_r|h}}{4\pi\sigma_A|k_r|}$. This can simplify equation (4.41) to

$$\hat{\mathring{V}}_{\mathrm{e}}^{A} = k_1 e^{-|k_r|z} + \frac{\hat{\imath}(w)}{4\pi\sigma_A|k_r|} e^{-|k_r||z-h|}. \tag{4.42}$$

The descriptive equations in layer B, however, are different as there is no electrode in this layer.

In layer B the voltage distribution in the extracellular space is written as

$$\nabla^2 V_{\mathrm{e}}^{B} = 0, \tag{4.43}$$

which can be solved as

$$\hat{\mathring{V}}_{\mathrm{e}}^{B} = k_1' e^{-|k_r|z} + k_2' e^{|k_r|z}, \tag{4.44}$$

in which k_1' and k_2' are constants to be found. Assuming $\hat{\mathring{V}}_{\mathrm{e}}^{B}(z) \to 0$ as $z \to -\infty$, we conclude $k_1' = 0$. Therefore, the simplified equation will be

$$\hat{\mathring{V}}_{\mathrm{e}}^{B} = k_2' e^{|k_r|z}, \tag{4.45}$$

To find the remaining unknown constants in equations (4.42) and (4.45), the boundary conditions at $z = 0$ are used. These boundary conditions are continuity of voltage and current across the boundary between the layers. The following relationship between the differential equation coefficients in layers A and B are the result of applying the boundary conditions at $z = 0$. If it is assumed that $h > 0$, as shown in Figure 4.4 and the areas underneath the electrode is taken as the region of interest i.e., $z < h$ then equation (4.42) is changed to

$$\hat{\mathring{V}}_{\mathrm{e}}^{A} = k_1 e^{-|k_r|z} + \frac{\hat{\imath}(w)}{4\pi\sigma_A|k_r|} e^{|k_r|(z-h)}. \tag{4.46}$$

By using the voltage boundary conditions at $z = 0$, we have

$$\begin{aligned} \check{V}_{\mathrm{e}}^{A}(z)\Big|_{z=0^+} &= \check{V}_{\mathrm{e}}^{B}(z)\Big|_{z=0^-} \longrightarrow \\ k_1 + \frac{\hat{\imath}(\omega)}{4\pi\sigma_A|k_r|} e^{-|k_r|h} &= k_2', \end{aligned} \tag{4.47}$$

and the current density boundary condition is

$$\check{\mathbf{J}}_{\mathrm{e}}^{A}(z)\cdot\mathbf{n}\,\Big|_{\mathbf{z}=\mathbf{0}^{+}} \;=\; \check{\mathbf{J}}_{\mathrm{e}}^{B}(z)\cdot\mathbf{n}\,\Big|_{\mathbf{z}=\mathbf{0}^{-}}, \tag{4.48}$$

where $\mathbf{n}$ is the normal vector to the common border between the layers. In this configuration, $\mathbf{n}=\mathbf{a_z}$. Hence, equation (4.48) is changed to

$$\begin{aligned} \check{\mathbf{J}}_{\mathrm{e}}^{A}(z)\cdot\mathbf{a_z}\,\Big|_{\mathbf{z}=\mathbf{0}^{+}} &= \check{\mathbf{J}}_{\mathrm{e}}^{B}(z)\cdot\mathbf{a_z}\,\Big|_{\mathbf{z}=\mathbf{0}^{-}} \longrightarrow \\ -\sigma_A\frac{\partial\check{V}_{\mathrm{e}}^{A}}{\partial z}\,\Big|_{z=0^{+}} &= -\sigma_B\frac{\partial\check{V}_{\mathrm{e}}^{B}}{\partial z}\,\Big|_{z=0^{-}} \longrightarrow \\ \sigma_A\Big(-k_1|k_r| + \frac{\hat{\imath}}{4\pi\sigma_A}e^{-|k_r|h}\Big) &= \sigma_B k_2'|k_r| \end{aligned} \tag{4.49}$$

Combining equations (4.47) and (4.49), the constants k_1 and k_2' are calculated as

$$\begin{aligned} k_1 &= \frac{\hat{\imath}(\omega)}{4\pi(\sigma_B+\sigma_A)\sqrt{k_x^2+k_y^2}}\Big(1-\frac{\sigma_B}{\sigma_A}\Big)e^{-|k_r|h} \\ k_2' &= \frac{\hat{\imath}(\omega)}{4\pi|k_r|}\Big((\frac{1}{\sigma_B+\sigma_A})(1-\frac{\sigma_B}{\sigma_A})+\frac{1}{\sigma_A}\Big)e^{-|k_r|h} \\ &= \frac{2\hat{\imath}(\omega)}{4\pi(\sigma_A+\sigma_B)|k_r|}e^{-|k_r|h}. \end{aligned} \tag{4.50}$$

If these coefficients are replaced in equations (4.40) and (4.45) then the extracellular potential in each layer can be obtained.

4.4.2 Two-Layer Cellular Composite Model

Following the result of the volume conductor approach, we extend the method to the cellular composite modeling framework. In other words, instead of assuming a homogeneous tissue in each layer described by σ, we introduce an admitivitty kernel to capture the spatiotemporal change of the extracellular potential within tissue in each layer.

The cellular composite equations in layer A are rewritten as

$$\mathbf{J}^A_{\mathrm{e},\theta} = -\frac{1}{2\pi}\xi^A_{\mathrm{e},\theta} \underset{\mathbf{u}_\theta,t}{*} \nabla V^A_{\mathrm{e}}, \tag{4.51}$$

$$\mathbf{J}^A_{\mathrm{e}} = \int_\theta p(\theta)\mathbf{J}^A_{\mathrm{e},\theta} d\theta, \tag{4.52}$$

$$\nabla \cdot \mathbf{J}^A_{\mathrm{e},\theta} = \iota(t)\delta(x)\delta(y)\delta(z-h). \tag{4.53}$$

Combining these equations results to

$$\frac{1}{2\pi}\nabla \cdot \Big(\int_\theta p(\theta)\xi^A_{\mathrm{e},\theta} \underset{\mathbf{u}_\theta,t}{*} \nabla V^A_{\mathrm{e}} \Big) d\theta = -\iota(t)\delta(x)\delta(y)\delta(z-h), \tag{4.54}$$

where $u_\theta = [\cos\theta, \sin\theta, 0]$ defines the distribution of fibers in polar coordinates.

This equation can be expressed in the Fourier domain as

$$\int_\theta p(\theta)\check{\nabla}^T \check{\xi}^A_{\mathrm{e},\theta}\check{\nabla}\hat{\check{V}}^A_{\mathrm{e}} d\theta = \frac{-\hat{\iota}(\omega)}{2\pi}\delta(z-h), \tag{4.55}$$

where $\check{\nabla} = [jk_x, jk_y, \frac{\partial}{\partial z}]$. Substituting for $\hat{\check{\xi}}_{\mathrm{e},\theta}$ from equation (4.7), we find

$$\Big\{ \int_\theta p(\theta)\hat{\check{\xi}}^A_{\mathrm{e,T}}\check{\nabla}^T\check{\nabla} d\theta - \int_\theta p(\theta)(\hat{\check{\xi}}^A_{\mathrm{e,L}}(\mathbf{k},\omega;\mathbf{u}_\theta) - \hat{\check{\xi}}^A_{\mathrm{e,T}})(\mathbf{k}\cdot\mathbf{u}_\theta)^2 d\theta \Big\} \hat{\check{V}}^A_{\mathrm{e}} = \frac{-\hat{\iota}(\omega)}{2\pi}\delta(z-h), \tag{4.56}$$

where $\mathbf{k} = [k_x, k_y, 0]$. Expanding this equation further and using the fact that $\mathbf{k}\cdot\mathbf{u}_\theta = k_x\cos\theta + k_y\sin\theta$ results in

$$\begin{aligned} &-\int_\theta d\theta \hat{\check{\xi}}^A_{\mathrm{e,T}}\mathbf{k}^2 d\theta \hat{\check{V}}^A_{\mathrm{e}} + \int_\theta p(\theta)\hat{\check{\xi}}^A_{\mathrm{e,T}} d\theta \frac{\partial^2 \hat{\check{V}}^A_{\mathrm{e}}}{\partial z^2} - \\ &\int_\theta p(\theta)\Big(\frac{1}{\rho_{\mathrm{i}}}\frac{1+j\omega\tau_m+(\mathbf{k}\cdot\mathbf{u}_\theta)^2\lambda^2_{0J}}{1+j\omega\tau_m+(\mathbf{k}\cdot\mathbf{u}_\theta)^2\lambda^2_{0V}} - \hat{\check{\xi}}^A_{\mathrm{e,T}}\Big)(\mathbf{k}\cdot\mathbf{u}_\theta)^2 d\theta \hat{\check{V}}^A_{\mathrm{e}} = \frac{-\hat{\iota}(\omega)}{2\pi}\delta(z-h), \end{aligned} \tag{4.57}$$

which is equal to

$$-\int_\theta p(\theta)\hat{\hat{\xi}}^A_{\mathrm{e,T}}(k_r^2-(\mathbf{k}\cdot\mathbf{u}_\theta)^2)d\theta\hat{\check{V}}^A_{\mathrm{e}}+\int_\theta p(\theta)\hat{\hat{\xi}}^A_{\mathrm{e,T}}d\theta\frac{\partial^2\check{V}^A_{\mathrm{e}}}{\partial z^2}-$$
$$\int_\theta p(\theta)(\frac{1}{\rho_{\mathrm{i}}}\frac{1+j\omega\tau_m+(\mathbf{k}\cdot\mathbf{u}_\theta)^2\lambda_{0J}^2}{1+j\omega\tau_m+(\mathbf{k}\cdot\mathbf{u}_\theta)^2\lambda_{0V}^2})(\mathbf{k}\cdot\mathbf{u}_\theta)^2d\theta\hat{\check{V}}^A_{\mathrm{e}}=\frac{-\hat{\imath}(\omega)}{2\pi}\delta(z-h). \tag{4.58}$$

This is an ordinary differential equation in z of the form

$$c_1^A\frac{\partial^2\hat{\check{V}}^A_{\mathrm{e}}}{\partial z^2}-c_2^A\hat{\check{V}}^A_{\mathrm{e}}=\frac{-\hat{\imath}(\omega)}{2\pi}\delta(z-h), \tag{4.59}$$

where

$$c_1^A=\sum_{h=1}^{H}\alpha_h\hat{\hat{\xi}}^A_{\mathrm{e,T}}, \tag{4.60}$$
$$c_2^A=\sum_{h=1}^{H}\alpha_h\hat{\hat{\xi}}^A_{\mathrm{e,T}}((k_x^2+k_y^2-(\mathbf{k}\cdot\mathbf{u}_h)^2) \tag{4.61}$$
$$+\sum_{h=1}^{H}\alpha_h(\frac{1}{\rho_{\mathrm{i}}}\frac{1+j\omega\tau_m+(\mathbf{k}\cdot\mathbf{u}_h)^2\lambda_{0J}^2}{1+j\omega\tau_m+(\mathbf{k}\cdot\mathbf{u}_h)^2\lambda_{0V}^2})(\mathbf{k}\cdot\mathbf{u}_h)^2. \tag{4.62}$$

We assume the fibers are oriented in every direction within a plane. Hence, c_1^A and c_2^A can be approximated by an integral in polar coordinates and are calculated as

$$c_1^A=\hat{\hat{\xi}}^A_{\mathrm{e,T}}, \tag{4.63}$$
$$c_2^A=\left(\frac{1}{2}\hat{\hat{\xi}}_{\mathrm{e,T}}+\frac{1}{2\rho_i}\frac{\lambda_{0J}^2}{\lambda_{0V}^2}\right)k_r^2$$
$$+\frac{1}{\rho_i}\frac{(1-\frac{\lambda_{0J}^2}{\lambda_{0V}^2})}{\lambda_V^2(w)}\left(1-\frac{1}{\sqrt{1+\lambda_V^2(w)k_r^2}}\right). \tag{4.64}$$

The solution to the second order differential equation (4.19) with constant coefficients

with respect to z is

$$\begin{aligned}\hat{\mathring{V}}_{\mathrm{e}}^{A} =& \frac{\hat{\imath}(\omega)}{4\pi\sqrt{c_1^A c_2^A}}\left(e^{-\sqrt{\hat{\mathring{\chi}}^A(k_r,w)}(z-h)} - e^{\sqrt{\hat{\mathring{\chi}}^A(k_r,w)}(z-h)}\right)u(z-h) \\ &+ k_1 e^{-\sqrt{\hat{\mathring{\chi}}^A(k_r,w)}z} + k_2 e^{\sqrt{\hat{\mathring{\chi}}^A(k_r,w)}z},\end{aligned} \tag{4.65}$$

where $\hat{\mathring{\chi}}^A(k_r,w) = \sqrt{\frac{c_2^A}{c_1^A}}$ is the anisotropy ratio, $u(z)$ is the Heaviside step function and k_1 and k_2 are to be found through the choice of boundary conditions. The voltage at infinity is finite, hence, $\lim_{z\to\infty} \hat{\mathring{V}}_{\mathrm{e}}^{A} < \infty$. Given equation (4.65), to satisfy the condition at $z \to \infty$, we choose $k_2 = \hat{\imath}(\omega)/4\pi\sqrt{c_1^A c_2^A}e^{-\sqrt{\hat{\mathring{\chi}}^A(k_r,w)}h}$. Therefore, equation (4.65) is simplified to

$$\hat{\mathring{V}}_{\mathrm{e}}^{A} = \frac{\hat{\imath}(\omega)}{4\pi\sqrt{c_1^A c_2^A}}\left(e^{-\sqrt{\hat{\mathring{\chi}}^A(k_r,w)}|z-h|}\right) + k_1 e^{-\sqrt{\hat{\mathring{\chi}}^A(k_r,w)}z}. \tag{4.66}$$

The equation in layer B in the Fourier domain is expressed as

$$\sum_{h=1}^{H} \alpha_h \mathring{\nabla}^T \hat{\mathring{\xi}}_{\mathrm{e,h}}^{B} \mathring{\nabla} \hat{\mathring{V}}_{\mathrm{e}}^{B} = 0. \tag{4.67}$$

In order to calculate V_{e}^{B}, a similar approach to the previous section is taken. The only difference is that there is no electrode in this layer. Hence, the right-hand side of equation (4.67) is equal to zero. Given this explanation, the differential equation in layer B takes the form of

$$c_1^B \frac{\partial^2 \hat{\mathring{V}}_{\mathrm{e}}^{B}}{\partial z^2} - c_2^B \hat{\mathring{V}}_{\mathrm{e}}^{B} = 0, \tag{4.68}$$

with the solution being

$$\hat{\mathring{V}}_{\mathrm{e}}^{B} = k_1' e^{-\sqrt{\hat{\mathring{\chi}}^B(k_r,w)}z} + k_2' e^{\sqrt{\hat{\mathring{\chi}}^B(k_r,w)}z}, \tag{4.69}$$

where $\hat{\mathring{\chi}}^B(k_r,w) = \sqrt{\frac{c_2^B}{c_1^B}}$. Applying the boundary condition at $z = -\infty$, we conclude that $k_1' = 0$. To calculate the remaining unknown constant coefficients in equations (4.69), the boundary conditions at $z = 0$ are applied. We also assume $h > 0$ and $z < h$. Continuity

of voltage across the boundary results in

$$\begin{aligned} \hat{\mathring{V}}_{\mathrm{e}}^{A} &= \hat{\mathring{V}}_{\mathrm{e}}^{B} \longrightarrow \\ k_1 + \frac{\hat{\imath}(\omega)}{4\pi\sqrt{c_1^A c_2^A}} e^{-\sqrt{\hat{\mathring{\chi}}^A(k_r,w)}h} &= k_2'. \end{aligned} \tag{4.70}$$

Also, the normal component of the current density across the boundary remains continuous which means

$$\check{\mathbf{J}}_{\mathrm{e}}^{A}(z)\cdot\mathbf{n}\,\Big|_{\mathbf{z}=\mathbf{0}^+} \;=\; \check{\mathbf{J}}_{\mathrm{e}}^{B}(z)\cdot\mathbf{n}\,\Big|_{\mathbf{z}=\mathbf{0}^-}, \tag{4.71}$$

where $\mathbf{n}$ is the normal vector to the common border between the layers. In this configuration $\mathbf{n} = \mathbf{a_z}$. Hence, equation (4.71) is rewritten as

$$\Big(\int_\theta p(\theta)\hat{\mathring{\xi}}_{\mathrm{e},\theta}^{A}d\theta\Big)\check{\nabla}\cdot\hat{\mathring{V}}_{\mathrm{e}}^{A}\cdot\mathbf{a}_z\,\Big|_{z=0^+} = \Big(\int_\theta p(\theta)\hat{\mathring{\xi}}_{\mathrm{e},\theta}^{B}d\theta\Big)\check{\nabla}\cdot\hat{\mathring{V}}_{\mathrm{e}}^{A}\cdot\mathbf{a}_z\,\Big|_{z=0^-}, \tag{4.72}$$

which is equal to

$$\begin{aligned} \Big(\int_\theta p(\theta)\hat{\mathring{\xi}}_{\mathrm{e,T}}^{A}\Big)d\theta\frac{\partial\hat{\mathring{V}}_{\mathrm{e}}^{A}}{\partial z}\,\Big|_{z=0^+} &= \Big(\int_\theta \hat{\mathring{\xi}}_{\mathrm{e,T}}^{B}\Big)d\theta\frac{\partial\hat{\mathring{V}}_{\mathrm{e}}^{B}}{\partial z}\,\Big|_{z=0^-}, \longrightarrow \\ c_1^A\frac{\partial\hat{\mathring{V}}_{\mathrm{e}}^{A}}{\partial z}\,\Big|_{z=0^+} &= c_2^B\frac{\partial\hat{\mathring{V}}_{\mathrm{e}}^{B}}{\partial z}\,\Big|_{z=0^-}, \longrightarrow \\ c_1^A\left(\frac{\hat{\imath}(w)}{4\pi\sqrt{c_1^A c_2^A}}\sqrt{\hat{\mathring{\chi}}^A(k_r,w)}e^{-\sqrt{\hat{\mathring{\chi}}^A(k_r,w)}h} - k_1\sqrt{\hat{\mathring{\chi}}^A(k_r,w)}\right) &= c_1^B\sqrt{\hat{\mathring{\chi}}^B(k_r,w)}k_2'. \end{aligned} \tag{4.73}$$

The result of the above calculation leads to the following relationship between k_1 and k_2',

$$\sqrt{c_1^A c_2^A}k_1 + \sqrt{c_1^B c_2^B}k_2' = \frac{\hat{\imath}(\omega)}{4\pi}e^{-\sqrt{\hat{\mathring{\chi}}^A(k_r,w)}h}. \tag{4.74}$$

The equations in (4.70) and (4.74) can be rewritten in matrix form as

$$\begin{pmatrix} 1 & -1 \\ \sqrt{c_1^A c_2^A} & \sqrt{c_1^B c_2^B} \end{pmatrix}\begin{pmatrix} k_1 \\ k_2' \end{pmatrix} = \begin{pmatrix} \dfrac{-\hat{\imath}(w)}{4\pi\sqrt{c_1^A c_2^A}}e^{-\sqrt{\frac{c_2^A}{c_1^A}}h} \\ \dfrac{\hat{\imath}(w)}{4\pi}e^{-\sqrt{\frac{c_2^A}{c_1^A}}h} \end{pmatrix}. \tag{4.75}$$

By solving the matrix equality we find

$$\begin{aligned} k_1 =& \frac{\hat{\imath}(\omega)}{4\pi\left(\sqrt{c_1^A c_2^A}+\sqrt{c_1^B c_2^B}\right)}\left(1-\frac{\sqrt{c_1^B c_2^B}}{\sqrt{c_1^A c_2^A}}\right)e^{-\sqrt{\frac{c_2^A}{c_1^A}}h}, \\ k_2' =& \frac{2\hat{\imath}(\omega)}{4\pi\left(\sqrt{c_1^A c_2^A}+\sqrt{c_1^B c_2^B}\right)}e^{-\sqrt{\frac{c_2^A}{c_1^A}}h}. \end{aligned} \tag{4.76}$$

Equation (4.76) gives the remaining unknown parameters required to calculate the extracellular potential in each layer.

4.5 Numerical Results

In this section we provide the numerical calculation results for the extracellular potential of the cellular composite model. Our numerical calculation involves applying three-dimensional inverse Fourier transform to equation (4.24) to obtain the extracellular voltage in spatial and temporal domains. It should be noted that equation (4.24) contains a removable singularity at the origin which has been dealt with using the method introduced in Appendix D.

In all our calculations a monophasic pulse of 100 μs pulse-width and an amplitude of 1 μA is applied to tissue.

The first graph in this section, Figure 4.5, illustrates the effect of anisotropy predicted by the cellular composite model for laminar tissues. The four graphs are sketched within different distances from the electrode. Figure 4.5(a) shows an area of up to 10 μm from the electrode. In this region, the cellular composite contour in white matches the near-field solution in dashed black. The colorbar represents the logarithm of the extracellular potential in millivolts.

As the distance from the electrode increases, around 10 times more, 4.5(b), the cellular composite magnitude becomes smaller than the near-field solution. However, the solution is still isotropic. In the range of 1000 μm from the electrode, Figure 4.5(c), the effect of anisotropy becomes more pronounced. The far-field solution is replaced with

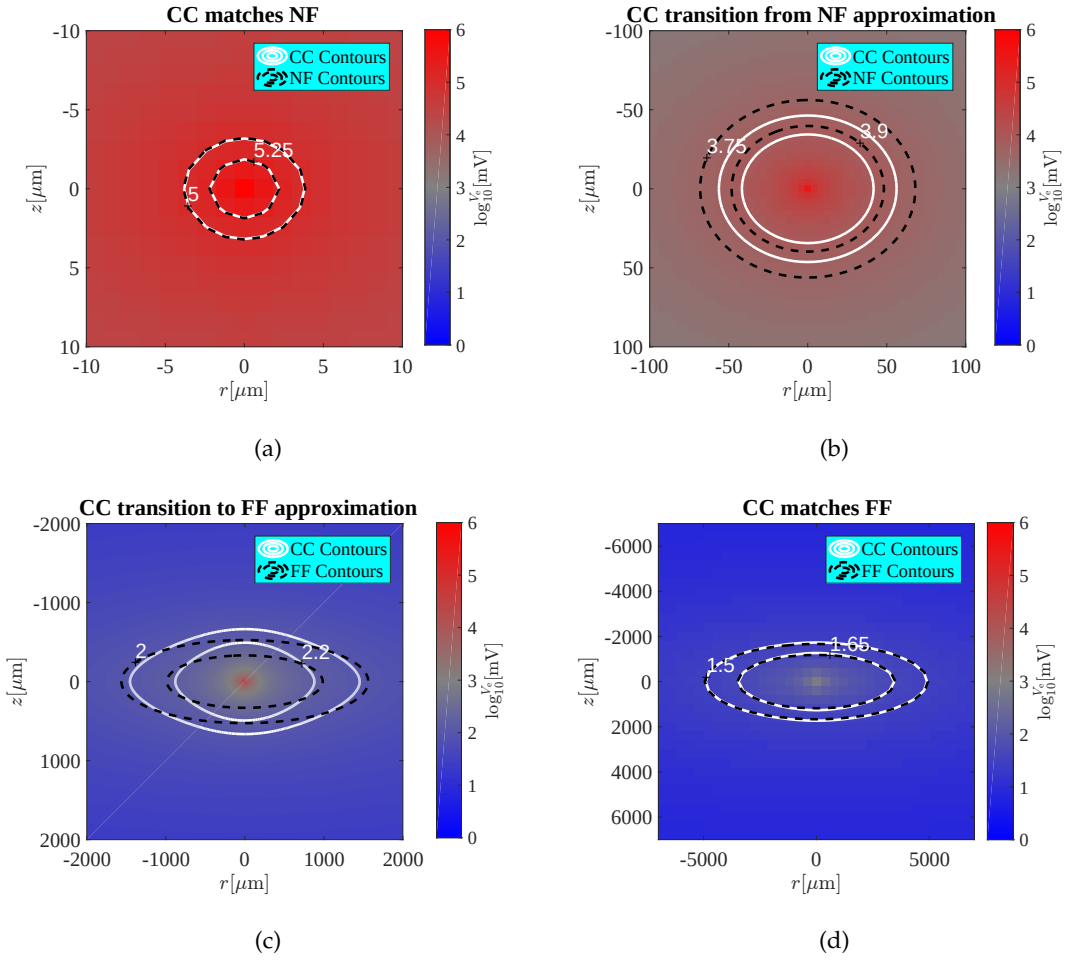

Figure 4.5: Anisotropy effect at time value $t = T_p$. (a) Cellular composite contours (white) are matched with the near-field contours (black) for a pulse width of 100μs, in a range of less than 5 μm from the electrode. (b) Transition of the cellular composite solution from the near-field solution. (c) Transition of the cellular composite to the far-field in the range of less than 1000 μm from the electrode. (d) Cellular composite is matched with the anisotropic solution in the far-field region.

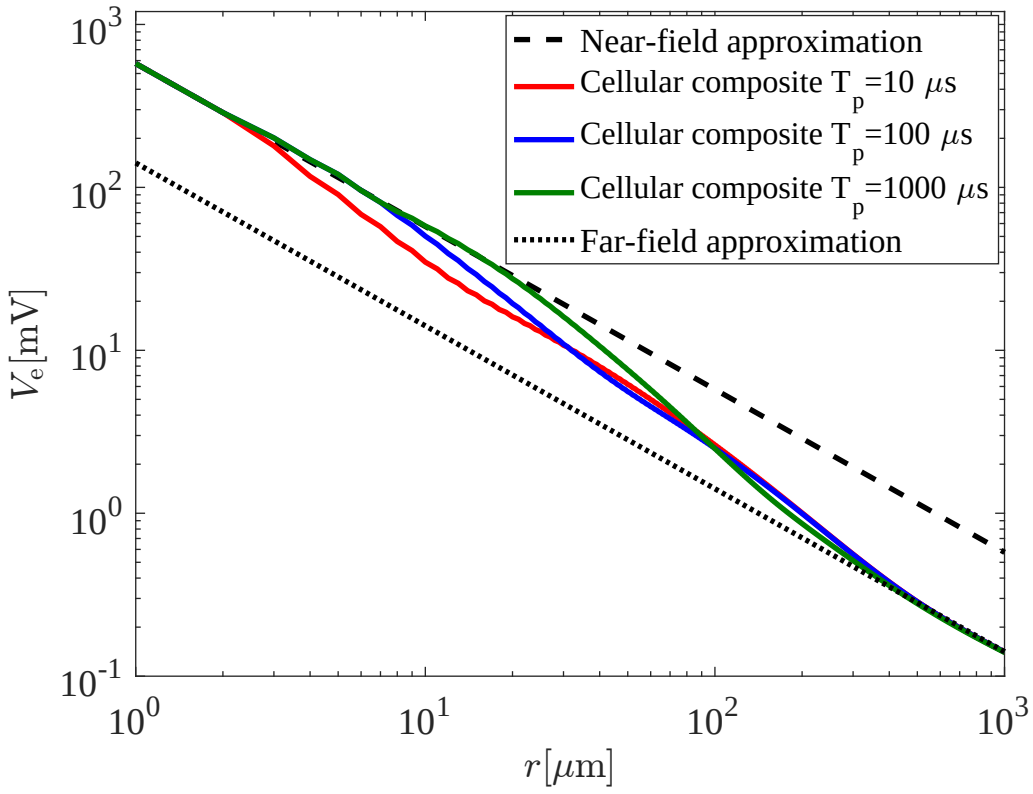

Figure 4.6: Pulse width effect at time value $t = T_p$. Graphs in red, blue and green correspond to stimuli with pulse widths 10 μs, 100 μs and 1000 μs, respectively. As the pulse width increases, the transition time between the near-field (dashed black line) and far-field (dotted black line) regions increases as well.

the near-field solution to better display the change of behavior of the cellular composite model. This is the range where the cellular composite makes a transition to match the far-field solution. By passing this range we see that the cellular composite and the far-field solutions are perfectly matched in a range of around 2000 μm from the electrode, Figure 4.5(d). Comparing the cellular composite behavior in this range with the graph in Figure 4.5(a), we notice a prominent change of shape as a result of anisotropy.

Note that anisotropy is influenced by the pulse-width as well. This means for different pulse-width durations the transition ranges and the shapes might be slightly different. The next graph in this section, Figure 4.6, is a one-dimensional plot in the r-direction

to explain the pulse-width effect on the transition distance. Three different pulse-widths, 10 μs, 100 μs and 1000 μs are sketched in red, blue and green, respectively. The standard volume conductor approximations at the near-field (dashed black) and the far-field (dotted black) are also plotted. We can see that as the pulse-width duration increases, the transition from the near-field to the far-field also increases. Note that these graphs may have numerical errors with unknown source (some wiggles are obvious).

4.6 Discussion

4.6.1 Anisotropy Effect

Tissue with laminar structure is an example of anisotropic neural tissue where fibers are oriented in a plane. As there is no fiber oriented along the z-axis, we expect to see a change of behavior as we go from the near-field to the far-field region.

The degree of anisotropy is defined as

$$\chi(k_r, w) = \sqrt{\frac{\hat{\hat{\xi}}_{\mathrm{e,L}}}{\hat{\hat{\xi}}_{\mathrm{e,T}}}}. \tag{4.77}$$

The near-field case corresponds to a combination of high spatial ($k_r\lambda_{0V} > k_r\lambda_{0J} \gg 1$) and low temporal frequency. In this case, the longitudinal admittivity in equation (4.9) is approximated as

$$\xi_{\mathrm{e,L}} = \frac{1}{\rho_i}\frac{\lambda_{0J}^2}{\lambda_{0V}^2} = \frac{1}{\rho_i}\frac{r_i}{r_e + r_i}. \tag{4.78}$$

By referring to Table 2.1 and assuming $a \approx b$ we obtain

$$\xi_{\mathrm{e,L}} \approx \frac{2d}{b\rho_e}. \tag{4.79}$$

This is equal to a resistivity of $\frac{b\rho_e}{2d}$. In this limit, the transverse ($\frac{b\rho_e}{d}$) and the longitudinal resistivities are only different by a factor of two which means tissue appears more isotropic in the near-field with the degree of anisotropy of $\sqrt{2}$.

The far-field limit is the case where $k_r\lambda_{0J} < k_r\lambda_{0V} \ll 1$. This leads to $\xi_{\mathrm{e,L}} \to \frac{1}{\rho_i}$. By

comparing equations (4.8) and (4.9), if we assume $d \ll b$ and $\rho_i \approx \rho_e$, then $\xi_{\mathrm{e,T}} \ll \xi_{\mathrm{e,L}}$. This simply means the resistivity in the transverse mode is higher. Physically, this means that in the far-field region most current enters the low impedance intracellular pathway via the membrane, with the effective resistivity of ρ_i in longitudinal direction. If we use the parameters in Table 3.1, we find the anisotropy degree is around 20. This is approximately 15 times more than the degree of anisotropy in the near-field region.

This is an effect that did not exist in the standard volume conductor model and is the result of an admittivity that has spatial and temporal components.

4.6.2 Pulse Width Effect

As displayed in Figure 4.6, the transition from the near-field to the far-field changes as the pulse width changes. For shorter pulse duration, $10\mu s$, the far-field model provides a good approximation for smaller electrode-neurite separation. The transition can be explained by investigating the electrode-neurite separation, r, relative to the effective electrotonic length constants, which are frequency-dependent

$$\begin{aligned} |\lambda_V(w)| &= \frac{\lambda_{0V}}{\sqrt{|1+jw\tau_m|}}, \\ |\lambda_J(w)| &= \frac{\lambda_{0J}}{\sqrt{|1+jw\tau_m|}}. \end{aligned} \tag{4.80}$$

As $|\lambda_V(w)| > |\lambda_J(w)|$, the far-field transition occurs when $r \gg |\lambda_V(w)|$ and the near-field transition occurs in the range $r \ll |\lambda_J(w)|$. Shorter pulse-width corresponds to higher temporal frequency. This results in a decrease in the magnitudes of $|\lambda_V(w)|$ and $|\lambda_J(w)|$ as seen by equation (4.80). As the electrotonic length constants decrease, the transition between near-field and far-field also decreases.

As explained earlier, the pulse duration can affect spatial characteristics of excitation for neural excitation such as the degree of anisotropy, equation (4.77). This is due to the fact that our measure of anisotropy includes admittivities with spatiotemporal components

$$\chi(k_r, w) = \sqrt{\frac{\hat{\hat{\xi}}_{\mathrm{e,L}}}{\hat{\hat{\xi}}_{\mathrm{e,T}}}}.$$

Therefore, as w changes, the frequency-dependent admittivity also changes and hence the degree of anisotropy.

4.7 Conclusion

In this chapter, the effect of a point source electrode on anisotropic neural tissue was modeled using the cellular composite approach. The fibers in the tissue were assumed to be uniformly oriented in every direction. Under this assumption, the admittivity kernel and the extracellular potential were computed. The result of the numerical calculation confirmed how anisotropy influences the voltage in the extracellular space under cellular composite modeling. This was contrasted with the solutions of the volume conductor models in the near-field and far-field regions where the anisotropy did not affect the prediction of the extracellular potential. To help explain this phenomenon mathematically, a measure of anisotropy based on the ratio of the longitudinal to transverse admittivities was introduced. Using this equation, it was shown that the ratio is much smaller in the near-field compared to the far-field region. Therefore, the behavior at distances greater than the voltage electrotonic length constant was shown to be more anisotropic. This is due to the current accessing the low resistance intracellular space via the membrane.

Also, we considered the effect of different pulse widths on the cellular composite as well as the standard volume conductor approaches. As predicted, since the admittivity in the cellular composite model had temporal as well as spatial components, the behavior changed as the pulse-width changed. The result showed longer transitions from the near-field to the far-field regions for longer pulse-widths and vice versa. This effect cannot be addressed in the standard volume conductor model, because in this approach neural tissue is described by a purely conductive element that is independent of temporal or spatial frequencies.

Apart from the numerical results, two mathematical extensions were also presented in this chapter. The first one demonstrated how we can use any other known distribution of fibers in tissue to predict behavior in more realistic neural tissue. This was shown for a Gaussian distribution of fiber orientations. The second extension explained a way to

build a layered inhomogeneous structure, such as the retina or the cortex, using appropriate boundary conditions.

In the following chapter, we take advantage of our modeling framework presented in the previous chapter and this one to model the gray matter of the cortex and investigate the effect of glia cells on the brain resistivity.

Chapter 5
Model of Cortex and Effect of Glia

5.1 Introduction

THE nervous system consists of cells with different morphologies and electrical properties. The two main types, however, are categorized as neurons and glial cells. Cells within each category can have different electrical properties, a fact that we have ignored for simplicity. In the previous chapters, our focus was mainly on modeling neuron dynamical behavior and all the numerical calculations were performed assuming neuron electrical parameters. However, in every piece of neural tissue, neurons and glial cells are intermingled together. Neurons are the cells responsible for the generation of action potential while the role of glial cells is to provide support, as explained in Chapter 1, to neuronal function. Electrical properties and geometry of neuron and glia are quite different. Glia cells have a much leakier membrane compared to neurons leading to conducting more ions. This may have a significant impact on tissue admittivity depending on the ratio of the glia to neuron [Trachtenberg and Pollen, 1970]. In comparison to neurons, glia cells are smaller; their soma diameter is about 25-35 percent of the diameter of neurons [Alvarez-Maubecin et al., 2000]. While neuronal cell morphologies might vary in different tissues, for instance stellate or pyramidal-like morphologies, most glia cells such as astrocytes or microglia have a stellate morphology. That is there are many processes radiating from the cell body of a glia resulting in a spherical distribution of fibers [Alvarez-Maubecin et al., 2000].

Furthermore, the ratio of glia to neuron varies significantly in different regions of the brain. The review article by [Herculano-Houzel, 2014] provides an in-depth investigation

on how the glia to neuron ratio changes across brain structures and how it can affect the physiology of the brain. According to this article, the glia to neuron ratio does not vary uniformly across the brain structures and the reason behind that is related to the large variation of neuronal sizes across the brain.

Our focus in this chapter is to specifically look at the gray matter of the neocortex and model the effect of glial cells in combination with neurons on tissue admittivity. We give example on a range of different ratios of glia to neuron, from small to large, to study the effect of glial cells and compare to estimates of the ratio for cortex. This ratio is defined as how much of neural tissue is occupied by glial cells compared to neurons. The estimated values for different parts of the brain are taken from Herculano-Houzel [2014].

5.2 Admittivity Calculation in Different Directions

This model describes the gray matter of the cortex which has a layered structure. However, for simplicity, we assume a stratified structure that is homogeneous: This can be taken as modeling a single cortical layer, or alternatively making the assumption that differences between cortical layers can be ignored to a first approximation. The glia cells and neurons are intermingled together with different morphologies in this neural tissue. It is assumed that the glial cells (astrocytes and microglia) have a stellate morphology. For neurons we consider only pyramidal cells that make up 80 percent of the population. The neurites of pyramidal cells are partitioned into two sets. A laminar structure is assumed as a model of the distal portion of apical dendrites and for basal dendrites which means fibers are oriented in a plane and have no component outside that specific plane. These planes are stacked on top of each other along a vertical line to the plane. Finally, an axon or ascending dendrite of a pyramidal cells is modeled with a single fiber perpendicular to the laminar structure.

Using the constitutive equation of the cellular composite model we have

$$\begin{aligned}\mathbf{J}_{\mathrm{e}} &= -\frac{1}{2\pi}\xi_{\mathrm{e}}^{\mathrm{A}} \underset{\mathbf{u}_\alpha,t}{*} \nabla V_{\mathrm{e}} \\ &= -\frac{1}{2\pi}\left(\xi_{\mathrm{e}}^{\mathrm{G}} + \xi_{\mathrm{e}}^{\mathrm{N}_r} + \xi_{\mathrm{e}}^{\mathrm{N}_z}\right) V_{\mathrm{e}},\end{aligned} \tag{5.1}$$

where $\xi_{\mathrm{e}}^{\mathrm{A}}$ is the aggregate admittivity of the tissue and

$$\begin{aligned}
\xi_{\mathrm{e}}^{\mathrm{G}} =& p\int_{\alpha} d\alpha \xi_{\mathrm{e},\alpha}^{\mathrm{G}}, && \text{glial cell admittivity component,}\\
\xi_{\mathrm{e}}^{\mathrm{N}_r} =& q\int_{\alpha} d\alpha \xi_{\mathrm{e},\alpha}^{\mathrm{N}_r}, && \text{lateral dendrites of neuron,}\\
\xi_{\mathrm{e}}^{\mathrm{N}_z} =& (1-p-q)\xi_{\mathrm{e}}^{\mathrm{f}}, && \text{ascending dendrite or axon of pyramidal cell,}
\end{aligned} \tag{5.2}$$

where $\xi_{\mathrm{e},\alpha}^{\mathrm{G}}$ and $\xi_{\mathrm{e},\alpha}^{\mathrm{N}_r}$ are the admittivities of glia and neuron lateral component along direction α, respectively, and $\xi_{\mathrm{e}}^{\mathrm{f}}$ is the admittivity of a single fiber in the z direction. p is percentage of the glial cells and for simplicity we assume in most of the following that $q = \dfrac{1-p}{2}$ is the percentage of neuron horizontal dendrites.

Each admittivity in equation (5.2) has components in the r and z directions. By referring to the admittivity section in previous chapters, the glia and neuron admittivities in these directions are given as

Glia - stellate morphology with spherically symmetric distribution of orientation

$$\begin{aligned}
\hat{\xi}_{\mathrm{e}}^{\mathrm{G}_r} =& \frac{4\hat{\xi}_{\mathrm{e,T}}^{\mathrm{G}}}{3} + \frac{1}{\rho_i^{\mathrm{G}}\lambda_V^{\mathrm{G}2}(w)k_r^2}\left(1 - \frac{\tan^{-1}(k_r\lambda_V^{\mathrm{G}}(w))}{k_r\lambda_V^{\mathrm{G}}(w)}\right),\\
\hat{\xi}_{\mathrm{e}}^{\mathrm{G}_z} =& \frac{4\hat{\xi}_{\mathrm{e,T}}^{\mathrm{G}}}{3} + \frac{1}{\rho_i^{\mathrm{G}}\lambda_V^{\mathrm{G}2}(w)k_z^2}\left(1 - \frac{\tan^{-1}(k_z\lambda_V^{\mathrm{G}}(w))}{k_z\lambda_V^{\mathrm{G}}(w)}\right).
\end{aligned} \tag{5.3}$$

Neurons - lateral dendrites and planar distribution of orientation

$$\begin{aligned}
\hat{\xi}_{\mathrm{e,r}}^{\mathrm{N}_r} =& \frac{\hat{\xi}_{\mathrm{e,T}}^{N}}{2} + \frac{1}{2\rho_i^{\mathrm{N}}}\frac{\lambda_{0J}^{\mathrm{N}2}}{\lambda_{0V}^{\mathrm{N}\,2}} + \frac{1-\dfrac{\lambda_{0J}^{\mathrm{N}2}}{\lambda_{0V}^{\mathrm{N}\,2}}}{\rho_i^{\mathrm{N}}\lambda_V^{\mathrm{N}2}(w)k_r^2}\left(1 - \frac{1}{\sqrt{1+\lambda_V^{\mathrm{N}2}(w)k_r^2}}\right),\\
\hat{\xi}_{\mathrm{e,z}}^{\mathrm{N}_r} =& \hat{\xi}_{\mathrm{e,T}}^{\mathrm{N}}.
\end{aligned} \tag{5.4}$$

Neurons - ascending dendrite or axon

$$\begin{aligned}
\hat{\xi}_{\mathrm{e,r}}^{\mathrm{N}_z} =& \hat{\xi}_{\mathrm{e,T}}^{\mathrm{N}},\\
\hat{\xi}_{\mathrm{e,z}}^{\mathrm{N}_z} =& \hat{\xi}_{\mathrm{e,L}}^{\mathrm{N}} = \frac{1+\lambda_J^{\mathrm{N}2}(w)k_z^2}{\rho_i^{\mathrm{N}}(1+\lambda_V^{\mathrm{N}2}(w)k_z^2)}.
\end{aligned} \tag{5.5}$$

where $\hat{\hat{\varsigma}}^{\mathrm{G}_r}_{\mathrm{e}}$ and $\hat{\hat{\varsigma}}^{\mathrm{G}_z}_{\mathrm{e}}$ are glia admittivities, $\hat{\hat{\varsigma}}^{\mathrm{N}_r}_{\mathrm{e,r}}$ and $\hat{\hat{\varsigma}}^{\mathrm{N}_r}_{\mathrm{e},z}$ are neuron admittivities, and $\hat{\hat{\varsigma}}^{\mathrm{N}_z}_{\mathrm{e,r}}$ and $\hat{\hat{\varsigma}}^{\mathrm{N}_z}_{\mathrm{e},z}$ are the ascending dendrite/ axon admittivities in the r and z directions, respectively. Th expression for glia are obtained by setting $k_z = 0$ in the r-direction and $k_r = 0$ in the z-direction.

As can be seen, glia admittivity in both directions has the same functional form which is due to the assumption on cell morphology, i.e., isotropic distribution. For the horizontal component of neurons which is anisotropic (laminar morphology) the admittivity in the r direction (along fibers) is frequency dependent and is different from the constant conductivity in the z direction. This is opposite to the vertical component of neurons such as axon with the frequency dependent component in the z direction (across fibers) and a constant conductivity in the r direction.

Note that since neuron membrane resistance is larger than glia membrane resistance we have $r^{\mathrm{N}}_{\mathrm{M}} > r^{\mathrm{G}}_{\mathrm{M}}$. This means that the time constants of neuron and glial cells are different even though membrane capacitance is assumed to be the same, i.e., for neurons

$$\tau^{\mathrm{N}}_{\mathrm{m}} = R^{\mathrm{N}}_{\mathrm{M}} C_{\mathrm{M}} = 2\pi a^{\mathrm{N}} r^{\mathrm{N}}_{\mathrm{M}}, \tag{5.6}$$

and for glial cell

$$\tau^{\mathrm{G}}_{\mathrm{m}} = R^{\mathrm{G}}_{\mathrm{M}} C_{\mathrm{M}} = 2\pi a^{\mathrm{G}} r^{\mathrm{G}}_{\mathrm{M}}, \tag{5.7}$$

where R_{M} is the membrane unit area resistance and a is the diameter of the relevant cell.

This also results in having different static electrotonic length constants for each cell type

$$\begin{aligned}
\lambda^{\mathrm{G}}_{0J} &= \frac{r^G_m}{r^G_{\mathrm{e}} + r^G_{\mathrm{i}}}, \\
\lambda^{\mathrm{G}}_{0V} &= \frac{r^G_m}{r^G_{\mathrm{i}}}, \\
\lambda^{\mathrm{N}}_{0J} &= \frac{r^N_m}{r^N_{\mathrm{e}} + r^N_{\mathrm{i}}}, \\
\lambda^{\mathrm{N}}_{0V} &= \frac{r^N_m}{r^N_{\mathrm{i}}},
\end{aligned} \tag{5.8}$$

which in turn affects the frequency dependent electrotonic length constants

$$\begin{aligned}\lambda_J^{\mathrm{G}}(w) =& \frac{\lambda_{0J}^{\mathrm{G}}}{1+jw\tau_m^G},\\ \lambda_V^{\mathrm{G}}(w) =& \frac{\lambda_{0V}^{\mathrm{G}}}{1+jw\tau_m^G},\\ \lambda_J^{\mathrm{N}}(w) =& \frac{\lambda_{0J}^{\mathrm{N}}}{1+jw\tau_m^N},\\ \lambda_V^{\mathrm{N}}(w) =& \frac{\lambda_{0V}^{\mathrm{N}}}{1+jw\tau_m^N}.\end{aligned} \tag{5.9}$$

The differences in the electrotonic length constants result in different transitions lengths from the near-field to the far-field region for glia and neuron.

5.3 Extracellular Potential Calculation

The extracellular potential can be calculated using equation (5.1) and applying the continuity equation

$$\begin{aligned}\nabla\cdot\mathbf{J}_{\mathrm{e}} =& -\frac{1}{2\pi}\nabla\cdot\left(p\tilde{\varsigma}_{\mathrm{e}}^{\mathrm{G}}\underset{\mathbf{u}_{\alpha}^{G},t}{*}\nabla+q\tilde{\varsigma}_{\mathrm{e}}^{\mathrm{N}_r}\underset{\mathbf{u}_{\alpha}^{N},t}{*}\nabla+(1-p-q)\tilde{\varsigma}_{\mathrm{e}}^{\mathrm{N}_z}\underset{\mathbf{z},t}{*}\nabla\right)V_{\mathrm{e}}\\ =&\iota(t)\delta(x)\delta(y)\delta(z),\end{aligned} \tag{5.10}$$

where in the Fourier domain we obtain

$$\breve{\nabla}^T\left(p\hat{\breve{\varsigma}}_{\mathrm{e}}^{G}+q\hat{\breve{\varsigma}}_{\mathrm{e}}^{\mathrm{N}_r}+(1-p-q)\hat{\breve{\varsigma}}_{\mathrm{e}}^{\mathrm{N}_z}\right)\breve{\nabla}\hat{\breve{V}}_{\mathrm{e}} = -\frac{\hat{\iota}(w)}{(2\pi)^2}. \tag{5.11}$$

The three different admittivity components in this equation can be calculated separately. Introducing $\breve{\nabla}=j\mathbf{k}$ and $\mathbf{k}=(k_x,k_y,k_z)$

$$\mathbf{k}^T\left(p\hat{\breve{\varsigma}}_{\mathrm{e}}^{G}+q\hat{\breve{\varsigma}}_{\mathrm{e}}^{\mathrm{N}_r}+(1-p-q)\hat{\breve{\varsigma}}_{\mathrm{e}}^{\mathrm{N}_z}\right)\mathbf{k}\hat{\breve{V}}_{\mathrm{e}} =\frac{\hat{\iota}(w)}{(2\pi)^2}, \tag{5.12}$$

in which

$$\begin{aligned} p\mathbf{k}^T\left(\int_\alpha d\alpha \hat{\hat{\xi}}^{\mathrm{G}}_{\mathrm{e},\alpha}\right)\mathbf{k} &= \frac{p}{4\pi}\int_0^{2\pi}\int_0^{\pi}\mathbf{k}^T\hat{\hat{\xi}}^{\mathrm{G}}_{\mathrm{e},\alpha}\mathbf{k}\sin\phi d\phi d\theta, \\ &= p\left[\frac{4\hat{\hat{\xi}}^{\mathrm{G}}_{\mathrm{e,T}}}{3}K^2+\frac{1}{\rho_i^{\mathrm{G}}\lambda_V^{\mathrm{G}2}(w)\left(1-\frac{\tan^{-1}(K\lambda_V^{\mathrm{G}}(w))}{K\lambda_V^{\mathrm{G}}(w)}\right)}\right], \end{aligned} \tag{5.13}$$

is the uniform spherical distribution of fiber orientation of glia (stellate morphology) and $K=|\mathbf{k}|$, and

$$\begin{aligned} q\mathbf{k}^T\left(\int_\alpha d\alpha\hat{\hat{\xi}}^{\mathrm{N}_r}_{\mathrm{e},\alpha}\mathbf{k}\right) =& q\Bigg[\left(\frac{\hat{\hat{\xi}}^{N}_{\mathrm{e,T}}}{2}+\frac{\lambda_{0J}^{\mathrm{N}\,2}}{2\rho_i^{\mathrm{N}}\lambda_{0V}^{\mathrm{N}\,2}}\right)k_r^2 \\ &+\frac{1}{\rho_i^{\mathrm{N}}\lambda_V^{\mathrm{N}2}(w)}\left(1-\frac{\lambda_{0J}^{\mathrm{N}\,2}}{\lambda_{0V}^{\mathrm{N}\,2}}\right)\left(1-\frac{1}{\sqrt{1+\lambda_V^{\mathrm{N}2}(w)k_r^2}}\right) \\ &+\hat{\hat{\xi}}^{\mathrm{N}}_{\mathrm{e,T}}k_z^2\Bigg]. \end{aligned} \tag{5.14}$$

is the uniform distribution of lateral dendrites of neuron (laminar morphology) and

$$\begin{aligned} (1-p-q)\mathbf{k}^T\hat{\hat{\xi}}^{\mathrm{N}_z}_{\mathrm{e}}\mathbf{k} =& \Big(\hat{\hat{\xi}}^{\mathrm{N}}_{\mathrm{e,T}}k_r^2 \\ &+\frac{1+\lambda_J^{\mathrm{N}2}(w)k_z^2}{\rho_i(1+\lambda_V^{\mathrm{N}2}(w)k_z^2)}k_z^2\Big)(1-p-q), \end{aligned} \tag{5.15}$$

models the ascending dendrite or axon of pyramidal cell. By adding all these admittivities together, the aggregate admittivity for this tissue, in the form of $\mathbf{k}^T\hat{\hat{\xi}}^{A}_{\mathrm{e}}\mathbf{k}$, is given.

The extracellular potential in the Fourier domain is then obtained as

$$\hat{\hat{V}}_{\mathrm{e}} = -\frac{\iota(w)}{(2\pi)^2\mathbf{k}^T\hat{\hat{\xi}}^{A}_{\mathrm{e}}\mathbf{k}} \tag{5.16}$$

5.4 Limits of Glia-Neuron Interactions

Neurons and glia cells have different electrical properties. As a result their contribution to tissue resistivity is dominant in different spatial and temporal frequency ranges. Figure 5.1 shows how admittivity arising from neuron and glia cells change behavior within a distance from the electrode due to transition from high spatial frequencies near the electrode to low spatial frequencies in the far-field. Understanding and interpreting this figure is the core part of our analysis in this chapter. In this figure the electrotonic length constants are sketched in cyan for glial cells and in red for neurons. The anisotropic behavior of neurons is reflected in their ellipsoid shape as opposed to more isotropic and hence more circular glia behavior. The graph points out at six different regions of interaction that are labeled appropriately. The first index in each region, "G", refers to the glia and the second index, "N", refers to the neuron. The sub-indexes show whether that cell is in its near-field (NF), intermediate-field (IF) or far-field (FF) region.

Note as the glia membrane is much leakier (around 20 fold) than neuron membrane, the cyan lines are closer to the electrode (white circle at the origin). The region closer to the electrode corresponds to a case where both glia and neuron cells are in their near-field region, $\mathrm{G}_{NF}/\mathrm{N}_{\mathrm{NF}}$. This can be described as $r < \lambda_J^{\mathrm{G}}(w)$. The second region which is bounded by $\lambda_J^{\mathrm{G}}(w)$, $\lambda_V^{\mathrm{G}}(w)$ and $\lambda_J^{\mathrm{N}}(w)$ is when the neuron is still in the near-field while the glia has entered the intermediate-field, $\mathrm{G}_{IF}/\mathrm{N}_{\mathrm{NF}}$. The third region occurs when $\lambda_V^{\mathrm{G}}(w) < r < \lambda_J^{\mathrm{N}}(w)$. This is associated with glia in the far-field and neuron in the near-field, $\mathrm{G}_{FF}/\mathrm{N}_{\mathrm{NF}}$. However, due to differences in anisotropy arising from differences in morphology between neurons and glia, transitions between near and far field occur at different rates in different directions, which leads to a fourth region. In this case where $\lambda_J^{\mathrm{N}}(w) < r < \lambda_V^{\mathrm{G}}(w)$, both neurons and glial cells are in their intermediate-field and labeled as $\mathrm{G}_{IF}/\mathrm{N}_{\mathrm{IF}}$. By going further away from the electrode, outside the boundaries of $\lambda_V^{\mathrm{G}}(w)$ and $\lambda_J^{\mathrm{N}}(w)$ glia reaches its far-field limit whereas neurons are still transitioning through the intermediate-field. Eventually, in the range of $r \gg \lambda_V^{\mathrm{N}}(w)$, that is labeled as $\mathrm{G}_{FF}/\mathrm{N}_{\mathrm{FF}}$, both cells reach their far-field limit.

In our analysis of the regions we focus on three limiting cases shown as R_1, R_2 and R_3 in Figure 5.1. This correspond to neurons and glia being both in the near-field, being

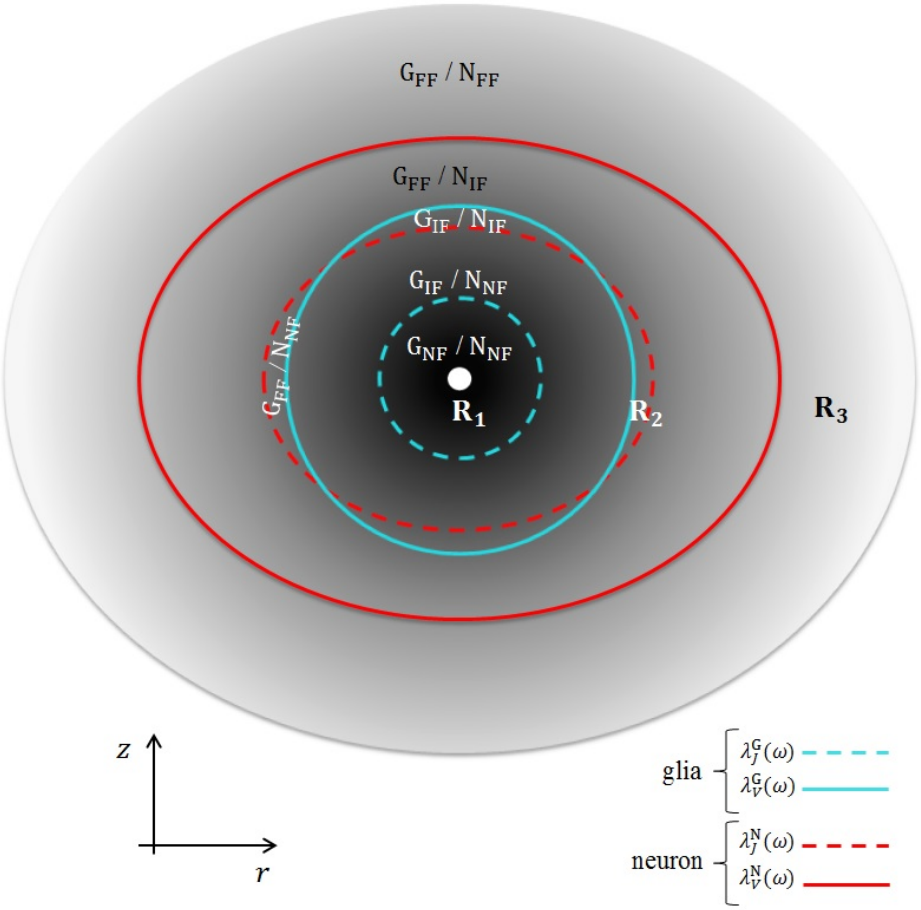

Figure 5.1: Regions marking different behavior for the admittivity of neurons and glia. Red (dashed and solid lines) corresponds to the current and voltage electrotonic length constants for neurons which are referred to as $\lambda_J^N(w)$ and $\lambda_V^N(w)$ in the text, respectively. Electrotonic length constants for glial cells, $\lambda_J^G(w)$ and $\lambda_V^G(w)$ are sketched in cyan (dashed and solid lines) respectively.

in near-field for neurons and far-field for glia, and both being in the far-field. Using the admitivity definitions in the previous section we calculate the conductivities based on the limits of vector $\mathbf{k}$ for the near-field and the far-field and then combine relevant parts of these conductivities to obtain tissue conductivity.

The near-field approximation of solutions is obtained when $k \to \infty$. We rewrite the aggregate admittivity equation (This is the denominator in equation (5.16)) in the following form which shows conductivities along different directions

$$\mathbf{k}^T \hat{\xi}_e^{A,NF} \mathbf{k} = \sigma_r^{NF} k_r^2 + \sigma_z^{NF} k_z^2, \tag{5.17}$$

where $k_r^2 = k_x^2 + k_y^2$ and

$$\begin{aligned} \sigma_r^{NF} &= p\frac{4\hat{\xi}_{e,T}^{G}}{3} + q\left(\frac{\hat{\xi}_{e,T}^{N}}{2} + \frac{{\lambda_{0J}^{N}}^2}{2\rho_i^N {\lambda_{0V}^{N}}^2}\right) + (1-p-q)\hat{\xi}_{e,T}^{N}, \\ \sigma_z^{NF} &= p\frac{4\hat{\xi}_{e,T}^{G}}{3} + q\hat{\xi}_{e,T}^{N} + (1-p-q)\frac{{\lambda_{0J}^{N}}^2}{\rho_i^N {\lambda_{0V}^{N}}^2}. \end{aligned} \tag{5.18}$$

are the conductivities in the near-field in the r and z directions. Having different conductivities in different directions is due to the anisotropy effect of neurons along these directions.

Conversely, the far-field approximation is calculated as $k \to 0$.

$$\mathbf{k}^T \hat{\xi}_e^{A,FF} \mathbf{k} = \sigma_r^{FF} k_r^2 + \sigma_z^{FF} k_z^2, \tag{5.19}$$

where

$$\begin{aligned} \sigma_r^{FF} &= p\left(\frac{4\hat{\xi}_{e,T}^{G}}{3} + \frac{1}{3\rho_i^G}\right) + q\left(\frac{\hat{\xi}_{e,T}^{N}}{2} + \frac{1}{2\rho_i^N}\right) + (1-p-q)\hat{\xi}_{e,T}^{N}, \\ \sigma_z^{FF} &= p\left(\frac{4\hat{\xi}_{e,T}^{G}}{3} + \frac{1}{3\rho_i^G}\right) + q\hat{\xi}_{e,T}^{N} + (1-p-q)\frac{1}{\rho_i^N}. \end{aligned} \tag{5.20}$$

It is important to reemphasize that the near-field and the far-field ranges change as a function of cell type.

Having calculated the near-field and far-field conductivities we provide a definition for admittivities in the regions R_1, R_2 and R_3 in Figure 5.1.

In region R_1 the cortex conductivity is the same as the near-field calculations in equation (5.18). For consistency we rewrite this equation as

$$\begin{aligned} \sigma_{r,C}^{R_1} &= p\frac{4\hat{\xi}_{e,T}^{G}}{3} + q\left(\frac{\hat{\xi}_{e,T}^{N}}{2} + \frac{{\lambda_{0J}^{N}}^2}{2\rho_i^N {\lambda_{0V}^{N}}^2}\right) + (1-p-q)\hat{\xi}_{e,T}^{N}, \\ \sigma_{z,C}^{R_1} &= p\frac{4\hat{\xi}_{e,T}^{G}}{3} + q\hat{\xi}_{e,T}^{N} + (1-p-q)\frac{{\lambda_{0J}^{N}}^2}{\rho_i^N {\lambda_{0V}^{N}}^2}. \end{aligned} \tag{5.21}$$

R_2 region corresponds to the case in which glial cells are in their far-field and the neurons are in their near-field. We have adopted these parts from the glia far-field conductivity in equation (5.20) and neuron conductivity in equation (5.18).

$$\begin{aligned}\sigma_{r,\mathrm{C}}^{R_2} =& p\left(\frac{4\hat{\xi}_{\mathrm{e,T}}^{\mathrm{G}}}{3}+\frac{1}{3\rho_i^{\mathrm{G}}}\right)+q\left(\frac{\hat{\xi}_{\mathrm{e,T}}^{\mathrm{N}}}{2}+\frac{{\lambda_{0J}^{\mathrm{N}}}^2}{2\rho_i^N{\lambda_{0V}^{\mathrm{N}}}^2}\right)+(1-p-q)\hat{\xi}_{\mathrm{e,T}}^{\mathrm{N}},\\ \sigma_{z,\mathrm{C}}^{R_2} =& p\left(\frac{4\hat{\xi}_{\mathrm{e,T}}^{\mathrm{G}}}{3}+\frac{1}{3\rho_i^{\mathrm{G}}}\right)+q\hat{\xi}_{\mathrm{e,T}}^{\mathrm{N}}+(1-p-q)\frac{{\lambda_{0J}^{\mathrm{N}}}^2}{\rho_i^N{\lambda_{0V}^{\mathrm{N}}}^2},\end{aligned} \tag{5.22}$$

For region R_3, the conductivities have already been calculated in (5.20) that is re-expressed as

$$\begin{aligned}\sigma_{r,\mathrm{C}}^{R_3} =& p\left(\frac{4\hat{\xi}_{\mathrm{e,T}}^{\mathrm{G}}}{3}+\frac{1}{3\rho_i^{\mathrm{G}}}\right)+q\left(\frac{\hat{\xi}_{\mathrm{e,T}}^{N}}{2}+\frac{1}{2\rho_i^N}\right)+(1-p-q)\hat{\xi}_{\mathrm{e,T}}^{N},\\ \sigma_{z,\mathrm{C}}^{R_3} =& p\left(\frac{4\hat{\xi}_{\mathrm{e,T}}^{\mathrm{G}}}{3}+\frac{1}{3\rho_i^{\mathrm{G}}}\right)+q\hat{\xi}_{\mathrm{e,T}}^{N}+(1-p-q)\frac{1}{\rho_i^N}.\end{aligned} \tag{5.23}$$

Using these equations and the admittivity equations (5.3), (5.4) and (5.5) we introduce the following anisotropy ratios

$$\begin{aligned}\chi_{\xi} =& \sqrt{\frac{\xi_r(\mathbf{k},w)}{\xi_z(\mathbf{k},w)}},\\ \chi_{\sigma}^{R_i} =& \sqrt{\frac{\sigma_{r,\mathrm{C}}^{R_i}}{\sigma_{z,\mathrm{C}}^{R_i}}},\end{aligned} \tag{5.24}$$

where χ_{ξ} is the general anisotropy ratio and $\chi_{\sigma}^{R_i}$, and are the limiting values in region R_i, $i=1,2,3$.

We are primarily interested in the relative contributions of glia and neurons to overall tissue admittivity. To quantify this we introduce the glia admittivity ratio, as the glia admittivity to the total admittivity in the r and z directions. This can be defined generally as

$$\begin{aligned}S_r(\mathbf{k},w) =& \frac{\xi_{\mathrm{e}}^{G_r}}{\xi_r},\\ S_z(\mathbf{k},w) =& \frac{\xi_{\mathrm{e}}^{G_z}}{\xi_z},\end{aligned} \tag{5.25}$$

Table 5.1: Glia admittivity ratio in different regions

	$S_r^{R_1}$	$S_z^{R_1}$	$S_r^{R_2}$	$S_z^{R_2}$	$S_r^{R_3}$	$S_z^{R_3}$
$p = 0.1$	0.1071	0.0916	0.3826	0.3424	0.1347	0.0797
$p = 0.5$	0.5191	0.4756	0.8480	0.8241	0.5835	0.4382
$p = 0.9$	0.9067	0.8909	0.9805	0.9768	0.9265	0.8753

where in the limiting cases, using the defined conductivities have the forms

$$\begin{aligned} S_r^{R_i} &= \frac{\sigma_{r,G}}{\sigma_{r,\mathrm{C}}^{R_i}}, \\ S_z^{R_i} &= \frac{\sigma_{z,G}}{\sigma_{z,\mathrm{C}}^{R_i}}. \end{aligned} \tag{5.26}$$

Table 5.1 summarizes the values of S in different regions.

5.5 Numerical Result and Discussion

Our numerical calculation consists of three parts. First, we present the admittivity graphs in different directions. Then the admittivity ratio of glia to overall admittivity graphs are displayed and in the end, we discuss the effect of anisotropy through a few graphs.

In all the graphs the cyan dashed and solid lines are related to the inverse of current ($\lambda_J^G(w)$) and voltage ($\lambda_V^G(w)$) electrotonic length constants for glial cells, respectively. These denotes regions at which $k\lambda_J^G(w) > 1$ for the near-field, $k\lambda_J^G < 1 \ll k\lambda_V^G$ for the intermediate-field and $k\lambda_V^G \ll 1$ for the far-field. Similarly, the red dashed and solid lines belong to the inverse of the electrotonic length constants of neurons. All of the axes in this section are spaced logarithmically. The horizontal axis is related to the temporal frequency, Hz, and the vertical axis shows the spatial frequency.

We have used indexes FF, IF and NF that stand for far-field, intermediate-field and near-field, respectively. According to this categorization and based on how the electrotonic length constants curves intersect, we have labeled six regions corresponding to those in Figure 5.1 that are summarized in Table 5.2. The amplitude and phase of tissue admittivity in the (r, z) directions are sketched in Figures 5.2(a) and 5.2(b) for a case where 50 percent of tissue is glia and 50 percent is allocated to horizontal and vertical

Table 5.2: Six different regions of glia-neuron interaction

Sensitivity	Definition
G_{NF} /N_{NF}	Glia is in the near-field and neuron is in the near-field
G_{IF} /N_{NF}	Glia is in the intermediate-field and neuron is in the near-field
G_{FF} /N_{NF}	Glia is in the far-field and neuron is in the near-field
G_{FF} /N_{IF}	Glia is in the far-field and neuron is in the intermediate-field
G_{IF} /N_{IF}	Glia is in the intermediate-field and neuron is in the intermediate-field
G_{FF} /N_{FF}	Glia is in the far-field and neuron is in the far-field

components of neurons. In R_1 the admittivity has the smallest magnitude. As the spatial frequency becomes smaller (which means going towards the far-field region) the admittivity becomes larger. The low admittivity region means that the current takes the extracellular pathway whereas in the far-field region this current enters the low resistance (high admittivity) intracellular pathway. The phase graphs show a zero phase everywhere except in the range where the departure from zero is greatest. This is evident in the region where both cells are in their intermediate-field, G_{IF}/N_{IF} and also in G_{FF}/N_{IF} region. This is the result of a reactive effect of capacitance (and is within the range of electrical stimulation).

Figure 5.3 shows the admittivity ratio of glial cells to overall admittivity of tissue that is a function of spatial and temporal frequency. The numerical calculation is performed for different proportions of glia (p) and neuron ($1-p$) which may be the case for different parts of the brain. For instance, a study [Herculano-Houzel, 2014] shows that glia occupies less than 10 percent (around 9 percent to be more accurate) of the cells in the cerebellum, while in the gray matter this percentage is about 60 and if we look at the human brain as a whole, only 50 percent of the cells are glial cells. The reason behind such variation in the ratio has been related to the variation of the density of the neuronal cells across different brain structures (around 72-fold), while non-neuronal cell density varies little, around 3.7-fold in the human brain [Alvarez-Maubecin et al., 2000]. The left column in this figure belongs to the admittivity in the r direction and the right column belongs to the z direction. We have considered the following values for the proportion of glia in neural tissue. $p = 0.1$ is the limit of low glia population, $p = 0.5$ is similar to gray matter and $p = 0.9$ is the high limit of glia cells which is unrealistically high, but

included as an extreme case to starkly illustrate the effect of glia on tissue admittivity.

It is useful to consider the contribution of glia to overall admittivity in the limiting cases of regions R_1, R_2 and R_3. In each subplot, region R_1 is the limit of high spatial frequencies in which the contribution of glia to overall admittivity is approximately the same as there proportion in the tissue, $S \approx p$. This is because all the current goes through the extracellular space and the effect of glia in confining that space is in correspondence with their volume proportion. Region R_3 is the limit of low spatial or high temporal frequency. In this range $S > p$ in the r direction but not in the z direction. This can be related to the admittivities of neurons in the r and z directions. By comparing the admittivity norms of neurons in the r direction, $\hat{\bar{\varsigma}}^{\mathrm{N}_r}_{\mathrm{e,r}}$, and in the z direction $\hat{\bar{\varsigma}}^{\mathrm{N}_z}_{\mathrm{e,z}}$, we realize that the admittivity in the z direction is almost double the one in the r direction. This lowers the glia contribution to the admittivity in the z direction, thus $S < p$ in this direction. Region R_2 shows the greatest ratio among all other regions. In this region glia has a disproportionately large effect, however these are over a limited range of temporal and spatial frequencies. Physically, this means that the glia causes a short circuit effect to the extracellular current whereby current enters the glia intracellular pathway and avoids neuronal intracellular pathway. These regions occur in spatial frequencies of between 0.5-30 cycles/mm and the temporal frequencies of less than 1 kHz. This range is equivalent to a spatial scale of around 30 - 2000 μm and time scales longer than 1 ms. This range for the temporal frequency can be compared with the time constants for neurons (around 100 ms) and glial cells (around 0.35 ms). Similarly, the spatial scales should be compared with the length constants. This, for a neuron is around 625 μm for λ^N_{0J} and 1800 μm for λ^N_{0V} while for glial cells is between 37 μm for the current density length constant and 108 μm for voltage length constant.

Besides, as can be seen the size of the white region (which includes R_2 as well) increases as the glia population of tissue increases. This dependence is because region of high S gets larger with p.

The temporal frequency scale of the intrinsic signals is between 0.5 Hz for δ activity to 1 kHz for spiking whereas electrical stimulation frequency scale is usually above 1 kHz. Both intrinsic and external electrical stimulation can affect a wide range of spatial

Table 5.3: Spatial frequency scales

Brain Structure	Spatial Scale	Spatial Frequency
synapse	1 μm	1 cycles/ μm
neuron	10-100 μm	10-100 cycles/ mm
cortical column	200-400 μm	2.5-5 cycles/ mm
cortical area	>2000 μm	<0.5 cycles/ mm

Table 5.4: Temporal frequency

Brain Wave	Temporal frequency
δ	0.5-4 Hz
θ	4-8 Hz
α	8-12 Hz
β	12-40 Hz
δ	40-100 Hz
Local field potential	up to 300 Hz
Spike	1kHz

frequencies from synapse to cortical areas. These spatial and temporal frequency scales are given in Tables 5.3 and 5.4. The interaction between the intrinsic signals and the external electrical stimulation is shown in Figure 5.4. The white dashed box corresponds to the brain structures (spatial frequencies) and its intrinsic signals (temporal frequencies) and the solid yellow box shows the spatiotemporal frequency of electrical stimulation. In this figure, a typical range for the temporal frequency of electrical stimulation is given between 1-100 kHz. The lower range may have a slight overlap between the frequency of spiking that is around 1kHz. The spatial frequency of electrical stimulation close to the electrode depends on how fine a microelectrode array is designed. Current spatial scales of microelectrode arrays can range from around 2 cm at the largest and around 20-30 μm at the finest level. This can cover a range of brain structures from a size of a cortical area up to a size of a neuron, respectively. Note for practical purposes high density electrode arrays are used only when we are close to neural tissue.

To explain the effect of anisotropy we have sketched a matrix of graphs in Figure 5.5. These graphs are sketched for spatial and temporal frequencies (k_r, w) which corresponds to (r, t) in space and time. The image scale graphs are the anisotropy ratio which is the ratio of admittivity in the r over z direction, $\sqrt{\frac{\xi_r}{\xi_z}}$. Along different rows of this

matrix, the proportion of glia, p changes, and different columns show the variation in the proportion of neuron horizontal component, q, in the total admittivity. It is worth mentioning that any deviation from 1 is counted as anisotropy depending on if the admittivity in the r direction is larger or in the z direction. The graphs show as p increases tissue appears more isotropic. This means that the anisotropy ratio is closer to 1 for larger values of p. This can be inferred by comparing the graph color to the colorbar axis. However, by keeping p constant and increasing q (comparing different columns) we see that the anisotropy degree increases to a number more than one. The tissue is most nearly isotropic when $q = (1-p)/2$, i.e. fibers are equally split between horizontal and vertical components of neurons (middle column in Figure 5.5). If $q = 0$ we get a bias toward the vertical direction ($\chi < 1$), and $q = (1-p)$ we get bias toward the horizontal direction ($\chi > 1$) . This is the result of a higher population of horizontal neuron component along the r direction. In all these cases the far-field limit (R_3 region) appears more anisotropic compared to the near-field limit (R_1 region). The anisotropic behavior in the far-field region is due to the current redistribution in the distance of $r > \lambda_V^{\mathrm{N}}(w)$. In this region, the current gets access to the intracellular space of both glia and neurons. In Figure 5.5(a) the anisotropy degree in R_3 is around 0.35 which means the admittivity in the z direction is greater than in the r direction. This is because the neuron fiber in the z direction has more weight in creating this anisotropy degree. But for a plot like Figure 5.5(c) we expect to have a larger admittivity in the r direction as opposed to the z direction due to having a higher proportion of horizontal neuron component.

To sum up, in low glia limit, Figures 5.5(a), 5.5(b) and 5.5(c) tissue appears more anisotropic. In this case, depending on whether the vertical or horizontal component of the neuron is larger the anisotropy degree can be either smaller or larger than 1. In a case similar to cortical gray matter which contains 50 percent glia, the anisotropy still exists, Figures 5.5(d), 5.5(e) and 5.5(f), however with less variation between the near-field and far-field limits depending on the relative proportions of horizontal and vertical components of neurons. In all the graphs that include a high glia limit such as Figures 5.5(g), 5.5(h) and 5.5(i) we have a more isotropic tissue with a degree very close to 1. This shows the isotropic morphology of glia affects tissue admittivity predominantly.

5.6 Conclusion

In this chapter, we combined all our results from the previous chapters to account for more realistic neural tissue which includes glia as well as neurons. Neurons were assumed to be of a pyramidal type with two distinct partitions for their orientation distribution of their fibers. A laminar structure was considered for distribution orientation of the distal portion of apical dendrites and for basal dendrites and a single fiber modeled the axon or ascending dendrite. The glia distribution was more isotropic with stellate morphology. Different proportions of glia to neuron were assumed to investigate how much of an effect glia population has on the neural tissue resistivity. It was noted that as $S \to 1$ the tissue admittivity becomes a same as glia.

Our results showed that only in the intermediate range where the temporal frequency is less than 1 kHz and the spatial frequency of between 0.5-30 cycles/mm glia admittivity has a considerable effect and causing the injected current to pass through their membrane. This occurs when glial cells are in their far-field and neurons are in their near-field region. In other regions, however, the admittivity changes according to the proportion of the glia. We also realized the role of glia in increasing admittivity in R_2 corresponds to the region of many intrinsic brain signals. In the range of the electrical stimulation which is more in R_3 region, the effect of glia is more proportionate to their population.

Furthermore, the anisotropy degree was also investigated through plotting different proportions of glia and neuron horizontal components. In all the cases the far-field admittivity (R_3) appeared more anisotropic (more deviation from 1) than the near-field limit (R_1). In addition, anisotropy was smaller in the region of high glia limit compared to the low glia limit.

The effect of oligodendrocytes is not taken into account in this thesis, partially due to a limited amount of experimental values of the electrical properties of these cells. A role of these cells is to create myelin sheaths surrounding axons to speed up the passage of electrical signals, known as myelin. The study by [Bakiri et al., 2011] investigated the effects of myelin on the electrical properties of the nerve cells. The authors concluded that myelin reduces the capacitance and increases the resistance of the cell membrane to speed the electrical signal flow. However, the internodal membrane resistance of oligo-

dendrocytes is still unknown. Such a study may be helpful in the future to take into account the effect of oligodendrocyte cells in the same way as astrocytes to conclude the overall change in a neural tissue conductivity containing myelinated axons.

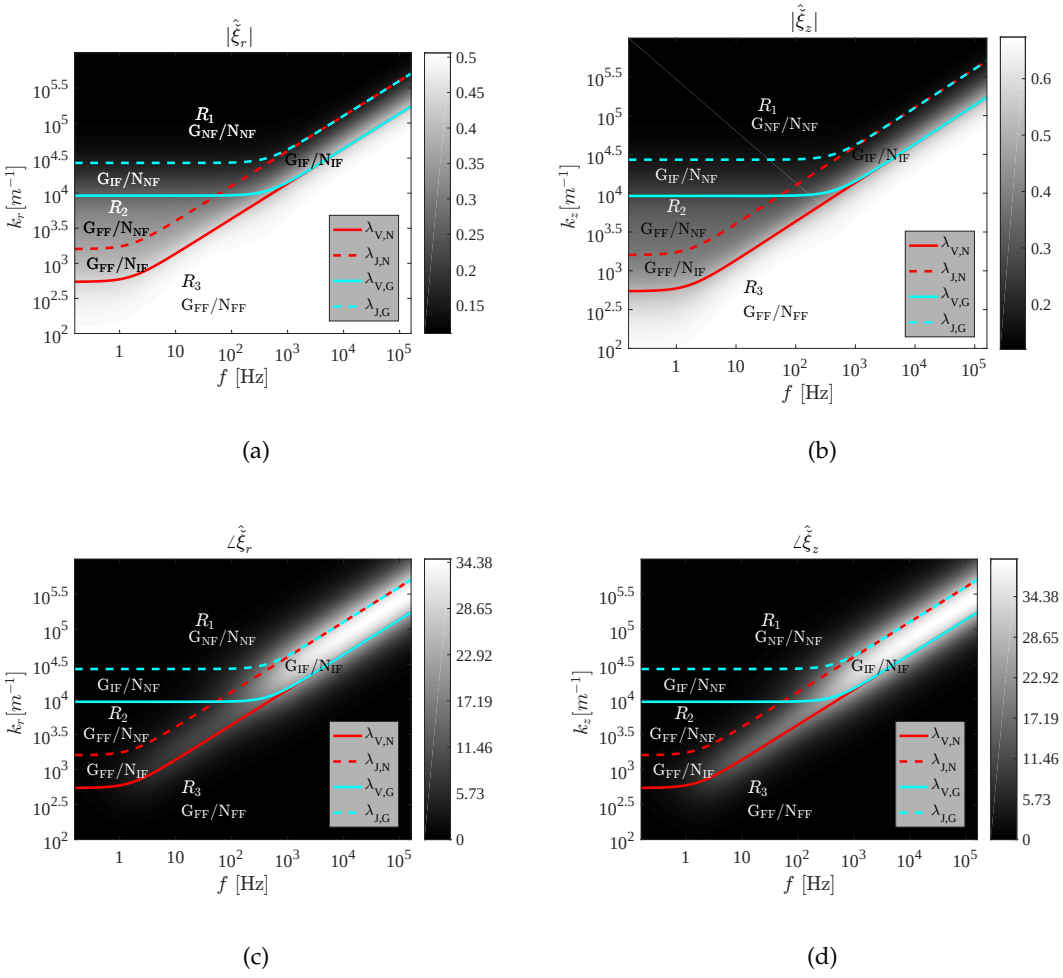

Figure 5.2: Admittivities of neural tissue consists of glia, neuron and fiber bundle. (a) Admittivity magnitude in the r direction. (b) Admittivity magnitude in the z direction. (c) Admittivity phase in the r direction (colorbar unit: degree). (d) Admittivity phase in the z direction (colorbar unit: degree).

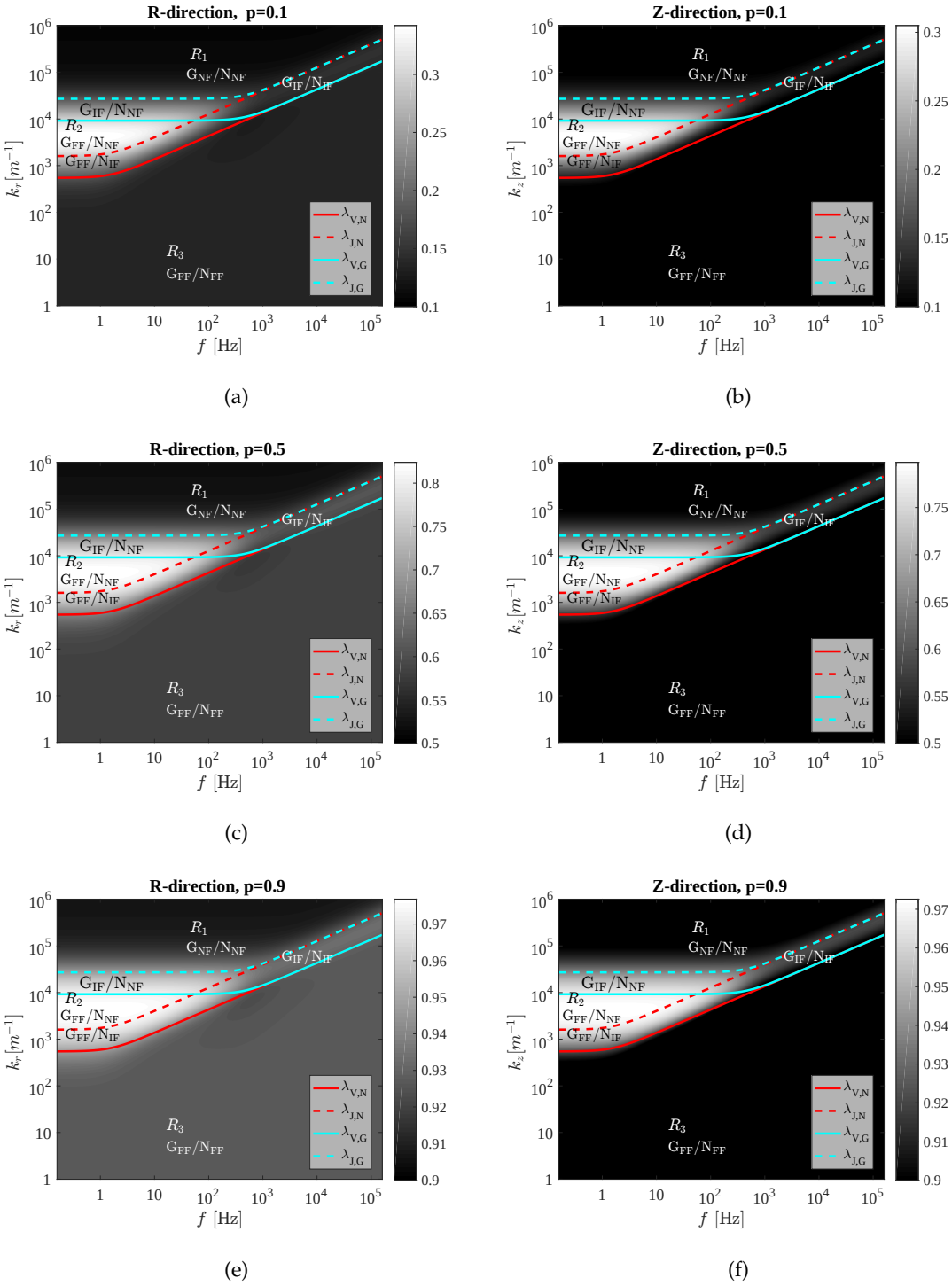

Figure 5.3: Glia admittivity to overall tissue admittivity. The figure shows the admittivity of glial cells to overall admittivity of neural tissue for different proportion of glia to neuron. Figures (a), (c) and (e) refer to this proportion for the cases when glia occupies 10, 50 and 90 percent of tissue in the r direction and Figures (b), (d) and (f) show similar cases but in the z direction. The axis are sketched in logarithmic spaces in terms of temporal and spatial frequencies. The cyan dashed and solid lines represent the electrotonic current and voltage length constants for glial cells and the red dashed and solid lines show the electrotonic current and voltage length constants for neurons.

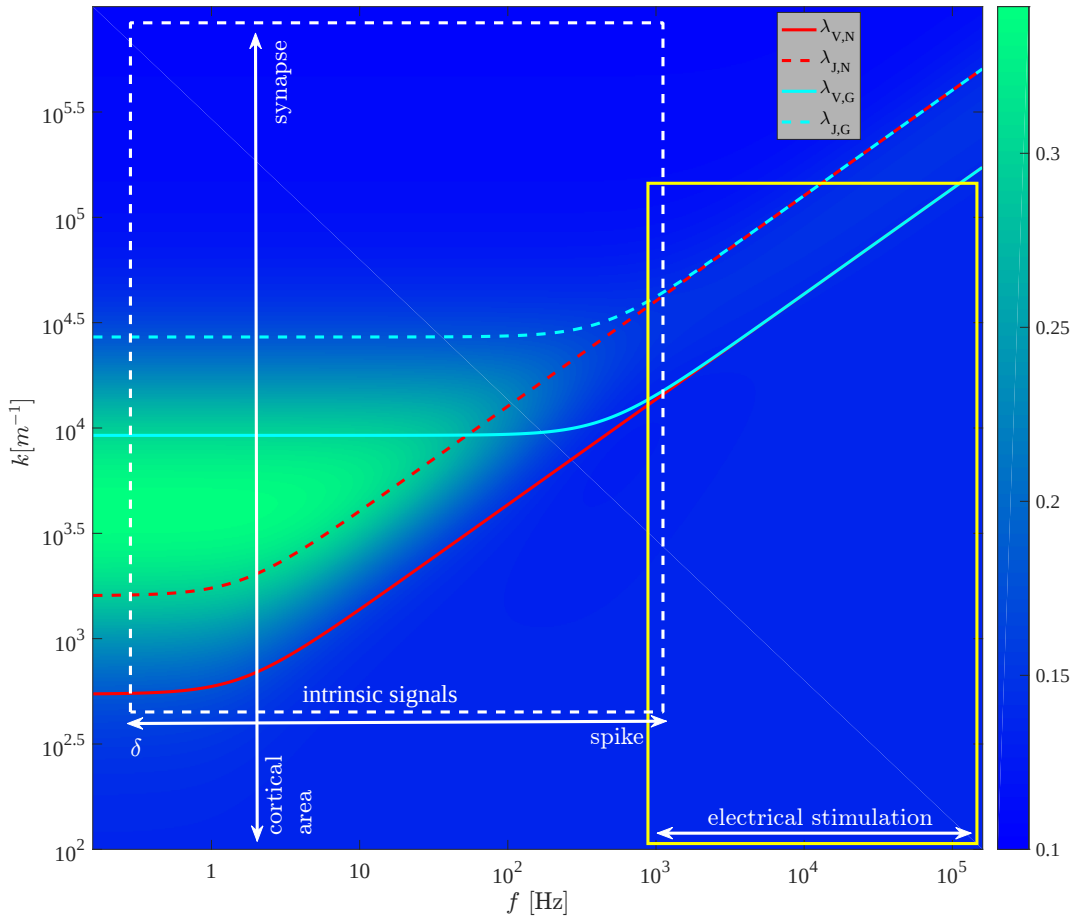

Figure 5.4: Spatial and temporal frequency interaction of the intrinsic signals and electrical stimulation

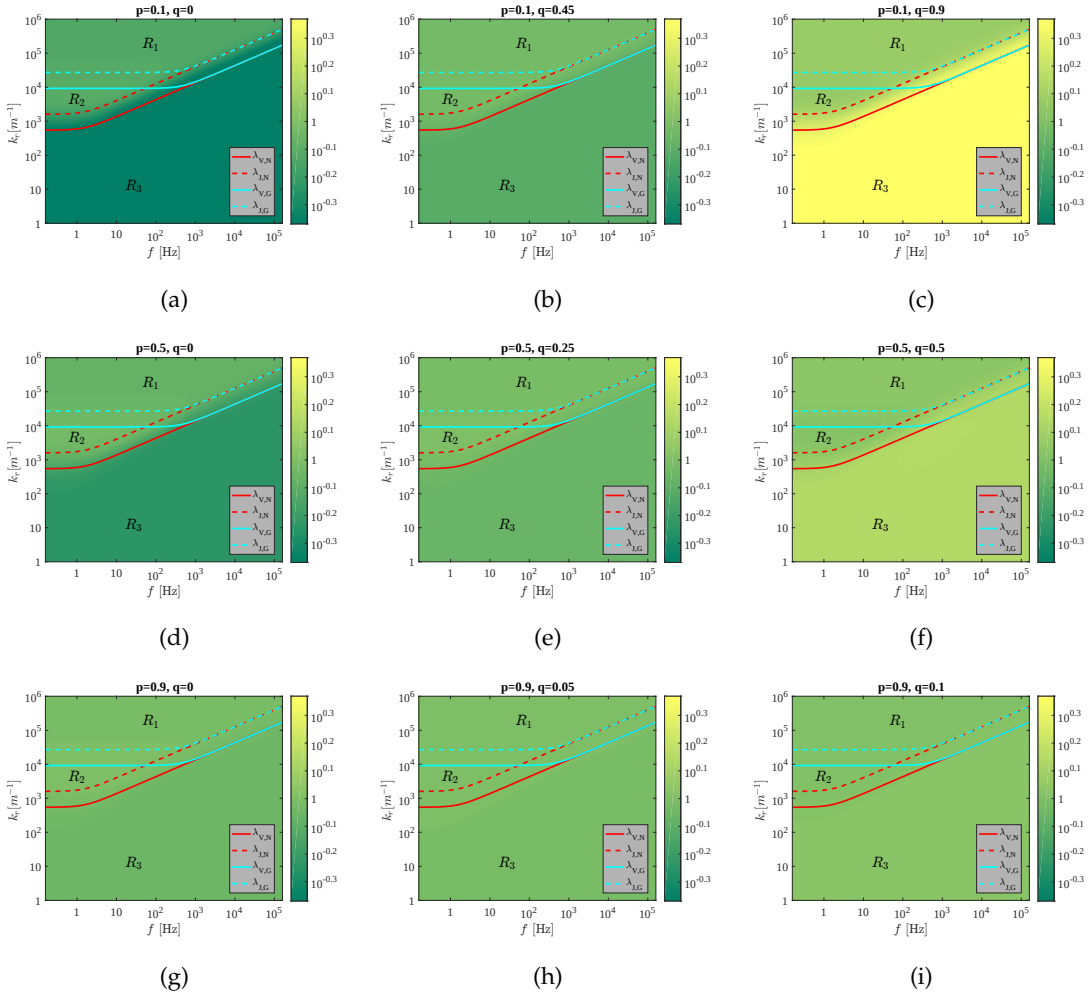

Figure 5.5: Anisotropy degree. The glia population changes along different rows and the horizontal component of neurons varies along different columns (a) 10 percent glia, 90 percent axon or ascending dendrite in the z direction and no horizontal neuronal component (b) 10 percent glia, 45 percent laminar distribution of neuron fibers in the r direction (c) 10 percent glia, 90 percent laminar distribution of neuron fibers in the r direction, no axon or ascending dendrite (d) 50 percent glia, 50 percent axon or ascending dendrite in the z direction and no horizontal neuronal component (e) 50 percent glia, 25 percent vertical component of neurons in the z direction and 25 percent laminar distribution of neuron fibers in the r direction (f) 50 percent glia, 50 percent laminar distribution of neuron fibers in the r direction, no vertical neuron component (g) 90 percent glia, 10 percent axon or ascending dendrite in the z direction and no horizontal neuronal component (h) 90 percent glia, 5 percent vertical component of neurons in the z direction and 5 percent laminar distribution of neuron fibers in the r direction (i) 90 percent glia, 10 percent laminar distribution of neuron fibers in the r direction, no vertical neuron component.

Chapter 6
Conclusion and Future Work

NEURAL electrical stimulation modeling is important in application of bionic devices to replace lost connection between the cells. An example of how electrical stimulation is applied in real life situations is shown in Figure 6.1. The figure shows a normal retina on the left and on the right, a retina with macular degeneration is displayed in which photoreceptor cells have died. However, with the help of electrical stimulation, the lost function can be replaced by an array of electrodes to deliver appropriate stimuli to other cells [Shepherd et al., 2013].

Another example of electrical therapeutic stimulation is deep brain stimulation. This method has been used in patients with epileptic seizures [Theodore and Fisher, 2004, Loddenkemper et al., 2001] or Parkinson's disease [Benabid, 2003, Okun, 2012] to rectify or control the brain signals. Modeling approaches can be advantageous in design stimulation protocols for these applications.

Our modeling framework extended the cellular composite method introduced in [Meffin et al., 2012, Meffin et al., 2014] to more general configurations of fiber orientation in neural tissue which contained glia cells as well as neurons. We introduced a spatiotemporal frequency dependent admittivity with passive electrical elements as a model of a neural membrane to account for cellular inhomogeneities. The spatial frequency arose from taking into account different current pathways and the temporal frequency was the result of modeling the capacitance property of the membrane.

In Chapter 3, we introduced neural tissue comprising cells with stellate morphology in three-dimensional space with uniform and Gaussian distribution for fiber orientations. Through this framework, we were able to demonstrate a transition between the

approximate solutions of standard volume conductor models in the near-field and far-field regions. The transition range fell within the region between the electrotonic length constants for current and voltage, $\lambda_I(w) < r < \lambda_V(w)$, which was around 10μm - 300μm. This range is very common in electrical stimulation applications. Furthermore, it was shown how modeling the cellular composition of tissue can affect voltage prediction in the extracellular space for different pulse widths. We found that for shorter pulse widths there was a shorter and sharper transition from the near-field to the far-field region. The implication of this is that the current redistribution occurs at shorter distances from the electrode dictated by the voltage electrotonic length constant. This means for shorter pulse width current can access the low impedance intracellular space in a shorter distance from the electrode and vice versa. This finding could be used to advantage to control the spread of excitation via pulse waveform.

We further generalized our work in Chapter 4 for tissues with a laminar structure such as the retina and the neocortex. These laminar structures have an anisotropic behavior because their fibers are only oriented in particular directions. Our comparison of the extracellular potentials of the cellular composite and the standard volume conductor model demonstrated that the anisotropy effect is only predictable through the former method. This was due to the effect of an admittivity which had spatial and temporal frequency dependence. The anisotropic behavior was shown to be stronger in the far-field region compared to the near-field or intermediate-field. This is because the current in the far-field region redistributes and takes the low resistance intracellular pathway while in the near-field the only current pathway accessible is the extracellular space.

Chapter 5 presented a step towards more realistic neural tissue model in which neurons and glial cells and parallel fibers coexisted together. A stellate morphology was assumed for glial cells and a laminar structure together with a single fiber represented neuron morphology. We analyzed the effect of glial cells on the overall admittivity of the brain. Different limits for glia population was considered i.e., the case where 10, 50 and 90 percent of the cells in tissue are glia. Glia membrane is more conductive than neuron membrane (around 20 times more) and therefore in specific frequency ranges, they have more a dominant effect. In this frequency range, which is less than 1kHz tempo-

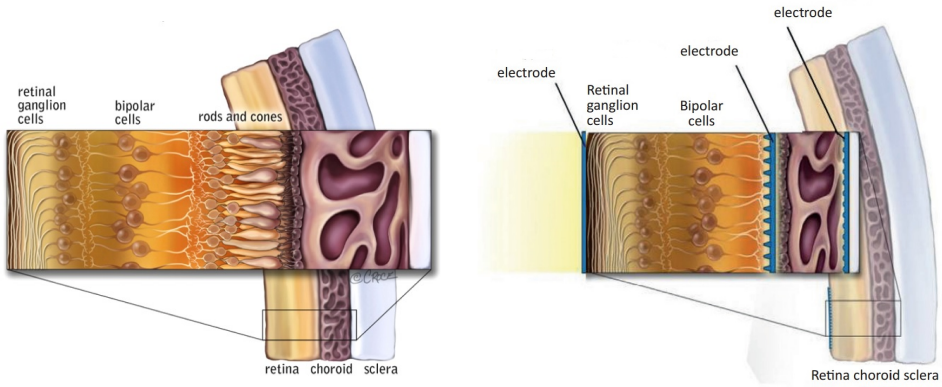

(a) (b)

Figure 6.1: (a) Healthy retina. (b) Retina with macular degeneration. Electrodes can be placed at different sites in the retina to partially replace the role of photoreceptor cells [Shepherd et al., 2013].

ral and between 0.5-30 cycle/mm spatial, glia provides a short circuit for current to pass through their membrane. This range is within the limits of intrinsic brain signals. This suggests a role of glia is to regulate admittivity in the spatiotemporal frequency range of intrinsic signals that exists in the brain. In other words, the electrical property of glia is such that it mainly alters admittivity in intrinsic signal range, but not outside it. For electrical stimulation applications, temporal frequencies tend to be higher due to the short pulse durations employed (10 μs-1000μs). For these frequency ranges, glial cells seemed to have an effect that was in proportion to their population. This underscores the importance of considering the temporal and spatial frequency dependence of tissue admittivity for electrical stimulation of neural tissue with bionic devices, including the range of effects we have described in this thesis. Furthermore, since the glia morphology is more similar to stellate and hence is more isotropic, whenever their ratio is higher compared to neurons, tissue appears more isotropic.

6.1 Future Work

Although in our modeling framework we tried to model neural tissue as realistic as possible, there are still a few steps to be taken to extend this work further. We have listed

several open questions in the following.

6.1.1 Membrane Potential Calculation

In order to have a complete model of electrical stimulation, we need to calculate the membrane potential. This can be done by applying the calculated extracellular potential in Chapters 3 and 4, to membrane potential equations in Chapter 2. Depending on which mode of stimulation is of interest the membrane potential can be obtained by solving either equation (2.23) for the longitudinal mode or equation (2.30) for the transverse mode of stimulation. However, the calculated membrane potential needs to be verified either through finite element software such as Comsol or through experimental data, as we do not have any analytical basis to confirm the calculated results.

One of the problems with the implementation in a finite element software, however, is that we have an infinite number of fibers. This is something that needs to be addressed carefully as the calculations may become tedious or even intractable.

6.1.2 Numerical Calculation of Gaussian Distribution of Fiber Orientations

Another great work that can be done is to find appropriate values for the standard deviation of Gaussian distribution of fiber orientations using experimental data and perform the calculation. We have derived equations describing the effect of the Gaussian distribution on tissue admittivity and the extracellular potential theoretically. However, experimental data are still required to accurately estimate orientation of fibers for individual's brain. Data emerging from the Human Brain Project and the Allen Brain Institute are expected to be useful in this regard.

6.1.3 Experimental Verification

To verify this model, an experimental setup is needed that uses microelectrode array for extracellular stimulation. The electrodes within the array are stimulated using a neural stimulator or digital signal processor. The accuracy of the stimulation really depends on the size of each electrode. The smaller the electrode the higher will be the accuracy of

stimulation. Besides, the choice of stimulating parameters such as frequency, amplitude, type of stimulus i.e., voltage or current, the direction of current flow may all affect tissue response. These effects can partially be addressed analytically using the results in this thesis, however, there are still some technical experimental issues that require different skills.

In this regard, some computer modeling in Comsol has been performed on three-dimensional models of tightly packed, parallel fibers by Sergeev and Meffin (unpublished). The idea is to test some of the approximations made in deriving a mean-field model from the full model, as was done for the cellular composite approach. The results show that the correspondence between these models is excellent over a large range of temporal and spatial frequencies.

6.1.4 Extension to an Inhomogeneous, Layered Neural Tissue

In Chapter 4, we explained how to choose appropriate boundary conditions to stack cellular composite models in a layered structure. This is readily achievable if fibers are infinite in extent, either within or across layers. However, including the effect of fibers with finite extent or branching is more challenging. The convolution arising from translation invariance no longer applies and the underlying equations for the trans-impedance of the neuron must be derived from first principles - at a task that may prove analytically intractable. During this process, we found that the calculation complexity increases dramatically after stacking two layers with different electrical properties. This work can be really important on stimulating a layered structure such as the cortex where it will be interesting to see how layer specific stimulation can influence the overall response in a cortical column. Toward this end, an in-depth understanding of the underlying microcircuit structure, as well as a layered mathematical model, is required.

Appendix A

Calculation of Voltage due to a Point Source Stimulation

A.1 Laplace's equation solution in an isotropic medium due to a point source electrode

The equations describing the extracellular potential and current density for the standard volume conductor models are

$$\mathbf{J}_e = -\sigma \nabla V_e, \tag{A.1}$$

$$\nabla \cdot \mathbf{J}_e = 0, \tag{A.2}$$

where $\mathbf{J}_e$ is the extracellular current density, σ is the conductivity of the tissue, and V_e is the extracellular potential in the tissue.

Substituting equation (A.1) into the equation (A.2) Laplace's equation is obtained which describes the spatial distribution of the voltage in the space. However, since we are dealing with a point source stimulator, the right hand side of the resulting equation is not equal to zero. The new equation is called Poisson's equation and that is

$$\sigma \left(\frac{\partial^2 V_e}{\partial x^2} + \frac{\partial^2 V_e}{\partial y^2} + \frac{\partial^2 V_e}{\partial z^2} \right) = -\iota(t)\delta(x)\delta(y)\delta(z), \tag{A.3}$$

where $\iota(t)$ is the total current coming out of an electrode and σ is the conductivity of the surface and is constant. The right hand side of equation (A.3) models a point source stimulator.

The solution of this equation is $V_e = \frac{\iota(t)}{4\pi\sigma R}$, where $R = \sqrt{x^2+y^2+z^2}$. To confirm, we substitute this equation into equation (A.3).

Case 1: $(x, y, z) \neq 0$. In this case, the right hand side of equation (A.3) is equal to zero. By using the following relationships

$$\begin{aligned}
\frac{\partial V_e}{\partial x} &= -\frac{x}{R^3}, \\
\frac{\partial V_e}{\partial y} &= -\frac{y}{R^3}, \\
\frac{\partial V_e}{\partial z} &= -\frac{z}{R^3}, \\
\frac{\partial^2 V_e}{\partial x^2} &= -\frac{1}{R^3} + \frac{3x^2}{R^5}, \\
\frac{\partial^2 V_e}{\partial y^2} &= -\frac{1}{R^3} + \frac{3y^2}{R^5}, \\
\frac{\partial^2 V_e}{\partial z^2} &= -\frac{1}{R^3} + \frac{3z^2}{R^5},
\end{aligned} \tag{A.4}$$

in equation (A.3), it can be shown that the result is zero as expected.

Case 2: $(x, y, z) = 0$.

For the proof in this case we need to use the following theorem.

Theorem A.1. *Divergence theorem*

The volume integral of the divergence of a vector field equals the total outward flux of the vector through the surface that bounds the volume, that is

$$\int_V \nabla \cdot J dv = \oint_S \mathbf{J} \cdot \hat{n} ds, \tag{A.5}$$

The left hand side is a volume integral over the volume V and ∂v is the differential change in the volume. The right hand side is the surface integral over the boundary of the volume V. The surface is shown by S and $\hat{n}$ is the outward pointing unit normal field of the boundary. The left-hand side of the equation represents the total of the sources in the volume V, and the right-hand side represents the total flow across the boundary S. For a point source in spherical coordinates, the normal vector $\hat{n}$ is equal to e_R, where e_R is the radial unit vector.

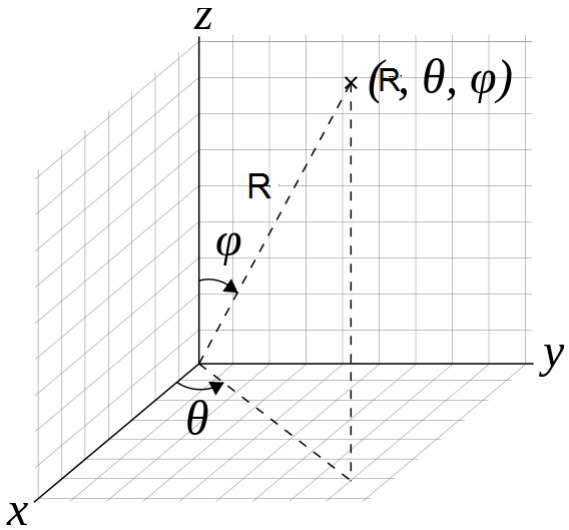

Figure A.1: Spherical coordinates.

Therefore,

$$\oint_S \mathbf{J} \cdot e_R ds = \int_{-\infty}^{\infty}\int_{-\infty}^{\infty}\int_{-\infty}^{\infty} \iota(t)\delta(x)\delta(y)\delta(z)dxdydz = \iota(t), \tag{A.6}$$

Substituting equation (A.1) in the above equation,

$$\oint_S \nabla V_\mathrm{e} \cdot e_R ds = -\frac{\iota(t)}{\sigma}, \tag{A.7}$$

Since only the radial component is nonzero, equation (A.7) will be

$$\int_0^{2\pi}\int_0^{\pi} \frac{\partial V_\mathrm{e}}{\partial R} R^2 \sin\phi d\phi d\theta = -\frac{\iota(t)}{\sigma}, \tag{A.8}$$

where (R, ϕ, θ) is the spherical coordinates components. R is radial distance, ϕ is the polar angle and θ is the azimuthal angle Figure A.1. The result of the above calculations is

$$\frac{\partial V_\mathrm{e}}{\partial R}\mathbf{R}^2 4\pi = -\frac{\iota(t)}{\sigma}, \tag{A.9}$$

Reorganising the above equation

$$dV_\mathrm{e} = -\frac{\iota(t)}{4\pi\sigma\mathbf{R}^2}dR, \tag{A.10}$$

and integrating both sides the voltage due to the point source stimulation is given as

$$V_{\mathrm{e}} = \frac{\iota(t)}{4\pi\sigma\mathbf{R}}. \tag{A.11}$$

On the other hand, from the Divergence theorem, the right hand side of equation (A.6), is equal to Laplace's equation

$$\int_V \nabla^2 V_{\mathrm{e}} dv = \oint_S \nabla V_{\mathrm{e}}.e_R ds \tag{A.12}$$

This shows that at the point $(x, y, z) = 0$ the voltage due to the point source is equal to equation (A.11) which completes the proof.

A.2 Calculation of the point source potential in Fourier domain

For the Poisson's equation in (A.3), another way to calculate the potential is via Fourier transform.

Taking the Fourier transform from both sides of equation (A.3)

$$\hat{\check{V}}_{\mathrm{e}} = \frac{\hat{\iota}(w)}{(2\pi)^2\sigma\mathbf{k}^2}, \tag{A.13}$$

where $\hat{f}(.)$ is the time Fourier transform and $\check{f}(.)$ is the spatial Fourier transform. $k = [k_x, k_y, k_z]^T$ is the three-dimensional Fourier transform of a point in the space and σ is the conductivity of the tissue and is constant.

To begin with, we write down the inverse Fourier transform definition and start the calculation from there.

$$V_{\mathrm{e}} = \frac{1}{(2\pi)^{(\frac{3}{2})}} \iiint \frac{\hat{\iota}(w)}{(2\pi)^2\sigma\mathbf{k}^2} e^{j(k_x,k_y,k_z).(x,y,z)} dk_x dk_y dk_z, \tag{A.14}$$

The above integral can be done in spherical coordinates. However, we made a small change in the definition of one of the angles in spherical coordinate, i.e., as shown in Figure A.2, instead of defining the angle between k_z axis and the vector $\mathbf{k}$ as ϕ, we defined that to be the angle between $\mathbf{k}$ and $\mathbf{R}$ which are the Fourier transform pairs. To calculate

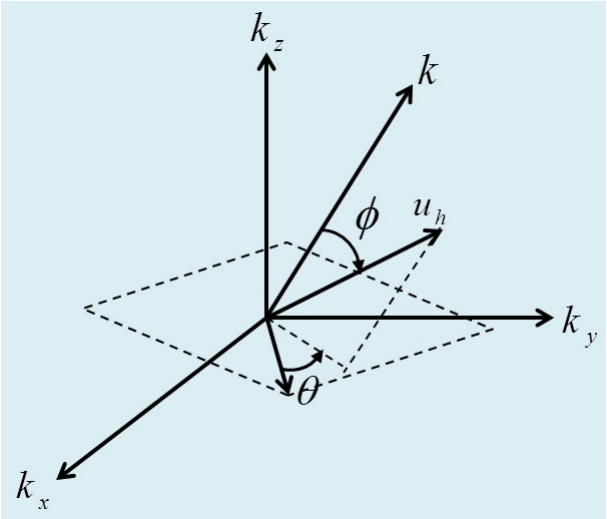

Figure A.2: A modified spherical coordinates.

this integral the following steps should be taken

Step 1

$$
\begin{aligned}
V_{\mathrm{e}} =& \frac{1}{(2\pi)^{(\frac{3}{2})}} \iiint \frac{\iota(t)}{(2\pi)^{(\frac{3}{2})}\sigma \mathbf{k}^2} e^{jKR\cos\phi} \mathbf{k}^2 \sin\phi \; dK d\theta d\phi \\
=& \frac{\iota(t)}{(2\pi)^2\sigma} \int_0^{\infty} \int_0^{\pi} e^{jKR\cos\phi} \sin\phi \; dK d\phi \\
=& \frac{\iota(t)}{(2\pi)^2\sigma} \int_0^{\infty} -\frac{1}{jKR}(e^{-jKR} - e^{+jKR}) \; dK \\
=& \frac{\iota(t)}{(2\pi)^2\sigma} \int_0^{\infty} -\frac{1}{jKR}(e^{-jKR} - e^{+jKR}) \; dK \\
=& \frac{\iota(t)}{(2\pi)^2\sigma} \int_0^{\infty} -\frac{2\sin(KR)}{KR} \; dK \\
=& \frac{\iota(t)}{4\pi\sigma \mathbf{R}}.
\end{aligned}
\tag{A.15}
$$

In the last step, we used the fact that

$$\int_0^\infty \frac{sin(p)}{p} dp = Rect(0) = \frac{\pi}{2}, \tag{A.16}$$

A.3 Laplace's equation in an anisotropic medium due to a point source electrode

The equations describing the extracellular potential and current density for an anisotropic volume conductor models are

$$\begin{aligned} \mathbf{J}_\mathrm{e} &= -\left[\sigma_x,\, \sigma_y,\, \sigma_z\right] \begin{bmatrix} \frac{\partial}{\partial x}\hat{a}_x \\ \frac{\partial}{\partial y}\hat{a}_y \\ \frac{\partial}{\partial z}\hat{a}_z \end{bmatrix} V_\mathrm{e}, \\ \nabla \cdot \mathbf{J}_\mathrm{e} &= 0, \end{aligned} \tag{A.17}$$

where $\mathbf{J}_\mathrm{e}$ is the extracellular current density, σ_x, σ_y, σ_z are the conductivities of the tissue in x, y and z directions respectively, and V_e is the extracellular potential in the tissue.

By combining the equations in (A.17)

$$\sigma_x \frac{\partial^2 V_\mathrm{e}}{\partial x^2} + \sigma_y \frac{\partial^2 V_\mathrm{e}}{\partial y^2} + \sigma_z \frac{\partial^2 V_\mathrm{e}}{\partial z^2} \quad = \quad -\iota(t)\delta(x)\delta(y)\delta(z), \tag{A.18}$$

To convert this equation into a form similar to the isotropic case in the previous section, the following transformation of variables are used

$$\begin{aligned} X &= \frac{x}{\sqrt{\sigma_x}}, \\ Y &= \frac{y}{\sqrt{\sigma_y}}, \\ Z &= \frac{z}{\sqrt{\sigma_z}}. \end{aligned}$$

Therefore,

$$\frac{\partial^2 V_e}{\partial X^2} + \frac{\partial^2 V_e}{\partial Y^2} + \frac{\partial^2 V_e}{\partial Z^2} = -\iota(t)\delta(\sqrt{\sigma_x}X)\delta(\sqrt{\sigma_y}Y)\delta(\sqrt{\sigma_z}Z), \tag{A.19}$$

which is equivalent to

$$\frac{\partial^2 V_e}{\partial X^2} + \frac{\partial^2 V_e}{\partial Y^2} + \frac{\partial^2 V_e}{\partial Z^2} = -\frac{\iota(t)}{\sqrt{\sigma_x\sigma_y\sigma_z}}\delta(X)\delta(Y)\delta(Z), \tag{A.20}$$

where we used the fact that $\delta(\alpha p) = \delta(p)/|\alpha|$.

This equation is quite similar to equation (A.3) with slightly different coefficients. Hence, applying the Divergence theorem results in

$$V_e = \frac{\iota(t)}{4\pi\sqrt{\sigma_x\sigma_y\sigma_z}\sqrt{\frac{x^2}{\sigma_x} + \frac{y^2}{\sigma_y} + \frac{z^2}{\sigma_z}}} \tag{A.21}$$

$$= \frac{\iota(t)}{4\pi\sqrt{\sigma_y\sigma_z x^2 + \sigma_x\sigma_z y^2 + \sigma_x\sigma_y z^2}}. \tag{A.22}$$

In particular case of planar distribution i.e., $\sigma_x = \sigma_y = \sigma_r$, this equation will simplify to

$$V_e = \frac{\iota(t)}{4\pi\sqrt{\sigma_r\sigma_z(x^2 + y^2) + \sigma_r^2 z^2}}. \tag{A.23}$$

Appendix B

Fourier Series Model of the Current Input

To be more computationally effective and handle the problem of memory usage we perform the spatial and temporal calculations separately.

The extracellular and membrane potential for planar distribution of fibers are defined as

$$\begin{aligned} \hat{\mathring{V}}_{\mathrm{e}} &= \frac{\hat{\imath}(\omega)}{4\pi\sqrt{2\pi}\sqrt{c_1 c_2}}\left(e^{-\sqrt{\frac{c_2}{c_1}}|z|}\right), \\ \hat{\mathring{V}}_{\mathrm{m}} &= -\frac{(\mathbf{k}\cdot\mathbf{u}_h)^2\lambda_V^2(w)}{1+(\mathbf{k}\cdot\mathbf{u}_h)^2\lambda_V^2(w)}\hat{\mathring{V}}_{\mathrm{e}}(\mathbf{k}), \end{aligned} \tag{B.1}$$

where

$$c_1 = \hat{\mathring{\xi}}_{\mathrm{e,T}}, \tag{B.2a}$$

$$\begin{aligned} c_2 =& \frac{1}{2}\left(\hat{\mathring{\xi}}_{\mathrm{e,T}} + \frac{1}{\rho_i}\frac{\lambda_{0J}^2}{\lambda_{0V}^2}\right)(k_x^2+k_y^2) \\ &+ \frac{1}{\rho_i}\frac{(1+jw\tau_m)(1-\frac{\lambda_{0J}^2}{\lambda_{0V}^2})}{\lambda_{0V}^2} \\ &- \frac{(1+jw\tau_m)^{3/2}(1-\frac{\lambda_{0J}^2}{\lambda_{0V}^2})}{\rho_i\lambda_{0V}^2\sqrt{1+jw\tau_m+\lambda_{0V}^2(k_x^2+k_y^2)}}. \end{aligned} \tag{B.2b}$$

Next, we assume $\hat{\imath}(w)/\sqrt{2\pi}$ can be written in terms of Fourier series. To be able to find

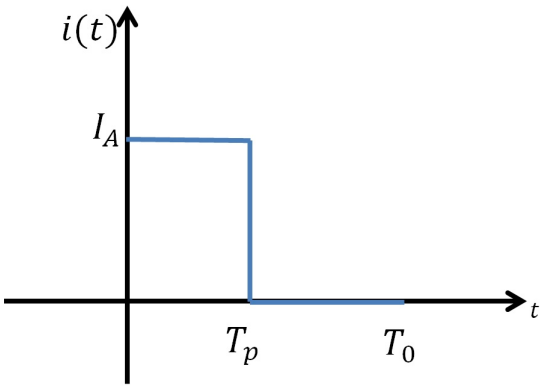

Figure B.1: Pulse input with pulse-width of T_p, period T_0 and amplitude I_A.

$\hat{\hat{V}}_e$ for any different current input, we assume

$$\hat{\hat{V}}_e = \frac{1}{4\pi\sqrt{c_1 c_2}}\left(e^{-\sqrt{\frac{c_2}{c_1}}|z|}\right), \tag{B.3}$$

We calculate the spatial inverse Fourier transform of this function and then insert the Fourier series of a pulse (or any other signal) instead of the term $\hat{\imath}(w)/\sqrt{2\pi}$ at different frequencies.

Assume the current input is a pulse signal with the properties as shown in Figure B.1. The equations for the Fourier transform are written as

$$\begin{aligned} \imath(t) &= \sum_{\nu=-\infty}^{\infty} c_\nu e^{j\nu wt}, \\ c_\nu &= \frac{1}{T_0}\int_{T_0} \imath(t) e^{-j\nu wt} dt, \end{aligned} \tag{B.4}$$

where $w = 2\pi/T_0$ and T_0 is the period of signal.

Assuming $T_0 = 2T_p$, c_k can be calculated as

$$\begin{aligned} c_k &= \frac{1}{2T_p}\int_0^{T_p} \iota(t)e^{-j\nu\omega t}dt, \\ &= \frac{I_A}{2T_p}\frac{-1}{j\nu w}e^{-j\nu w T_p}|_0^{T_p} \\ &= \frac{I_A e^{-j\nu w T_p/2}}{\nu w T_p}\sin\frac{\nu w T_p}{2} \\ &= \frac{I_A e^{-j\nu\pi/2}}{\nu\pi}\sin\frac{\nu\pi}{2}, \end{aligned} \tag{B.5}$$

Therefore,

$$\iota(t) = \frac{I_A}{2}\sum_{\nu=-\infty}^{\infty}\mathrm{sinc}(\frac{\nu\pi}{2})e^{-j\nu\pi/2}e^{j\nu w t}. \tag{B.6}$$

Consider $t = T_p$ is the point of interest to calculate the coefficients, therefore

$$\iota(T_p) = \frac{I_A}{2}\sum_{\nu=-\infty}^{\infty}\mathrm{sinc}(\frac{\nu\pi}{2})e^{j\nu\pi/2}. \tag{B.7}$$

Replacing $\iota(T_p)$ in the inverse Fourier transform of V_e results in

$$V_\mathrm{e} = \frac{1}{4\pi}\sum_{\nu=-\infty}^{\infty}\mathcal{F}^{-1}\{\frac{e^{-\sqrt{\frac{c_2}{c_1}}|z|}}{\sqrt{c_1 c_2}}\}\frac{I_A}{2}\mathrm{sinc}(\frac{\nu}{2})e^{j\nu\pi/2}. \tag{B.8}$$

This result has already been performed in Victorian Life Science computers for a finite number of frequencies. In the next stage we need to collect all the data at different frequencies and multiply them by an appropriate coefficient to find the change in the spatial and temporal profile of the extracellular and similarly membrane potential.

Appendix C
Sampling Method

In order to retrieve the correct spatial signal out of a DFT function, there are some parameters that play critical roles.

The relation between these parameters is determined via reciprocity relations:

$$\begin{aligned} A\Omega &= N, \\ \Delta x \Delta w &= \frac{1}{N} \end{aligned} \tag{C.1}$$

Function $f(\cdot)$ in spatial domain has the following properties:

- Domain of $f(\cdot)$: $\left[\frac{-A}{2}, \frac{A}{2}\right]$,
- Δx: Sampling interval (grid sampling) in spatial domain,
- $x_n = n\Delta x$,
- N: Number of samples.

Function $\hat{f}(\cdot)$ in Fourier domain has the following properties:

- Domain of $\hat{f}(\cdot)$: $\left[\frac{-\Omega}{2}, \frac{\Omega}{2}\right]$,
- Δw: Sampling interval (grid sampling) in Fourier domain,
- $w_k = k\Delta w$,
- N: Number of samples.

From reciprocity relations it is clear that the four important parameters are Δx, Δw, A, Ω.

C.0.1 How to obtain reciprocity relations

The fundamental unit of frequency is defined as

$$\Delta w = \frac{1}{A}. \tag{C.2}$$

This is the lowest frequency which corresponds to the largest period A. All other frequencies in DFT are an integer multiple of Δw.

As we can only have N grid points, Ω can be determined as $\Omega = \Delta w N$.

To obtain the first reciprocity relation we have

$$\Omega = N\Delta w = \frac{N}{A} \rightarrow A\Omega = N. \tag{C.3}$$

This equation shows that the length of spatial and frequency domain vary inversely with each other.

Remarks

1. If the number of samples, N, is held fixed, then an increase in the length of spatial domain comes at the expense of a decrease in the length of the frequency domain.
2. If N is fixed, then halving Δx, halves the length of the spatial domain.
3. Even if the input is real, the output might contain imaginary components.

Refine the frequency grid

Referring back to the spatial sample equation,

$$x_n = n\Delta x = n\frac{A}{N} \rightarrow \frac{x_n}{A} = \frac{n}{A}. \tag{C.4}$$

Remarks

1. If A and $k = -\frac{N}{2} + 1 : \frac{N}{2}$ are held fixed and $N \rightarrow \infty$, then DFT sum approaches an integral and $\Delta x = \frac{A}{N} \rightarrow 0$.

2. If within a function domain $[-\frac{A}{2}, \frac{A}{2}]$, a change is needed to approximate the spatial function at other points within the same domain, then the new sampling grid should also satisfy the reciprocity relations.

   Example:
   Assume $[-\frac{A}{2}, \frac{A}{2}]$ is held fixed and $\mathcal{F}\{f_n\}_k$ approximated the Fourier transform at $w_k = \frac{k}{A}$.

   If it is required to approximate the Fourier transform at points other than $w_k = \frac{k}{A}$, we proceed as follows

   - Define a new sampling grid: $\Delta w^{new} = \frac{1}{2A}$
   - From reciprocity relation we have $\Delta w^{new} \Delta x^{new} = \frac{1}{N}$
   - Therefore, $\Delta x^{new} = \frac{2A}{N}$

   In any case, if we want to double the number of grid point then it is possible to refine the frequency grid without increasing Δx^{new} or reducing the length of the frequency domain Ω. However, the new grid length must also obey the reciprocity relations.

C.0.2 Case 1: Band-limited function case

Steps that are needed to find the number of samples such that the DFT approximates Fourier transform are summarized in the following

(a) Assume the Fourier domain function is zero outside a certain frequency $w \geq \frac{\Omega}{2}$

(b) Find Ω and based on w, find the highest frequency equivalent period

(c) Use the definitions: $x_n = n\Delta x = n\frac{A}{N}$ and $w_n = k\Delta w$

(d) Maximum frequency $\frac{\Omega}{2}$ corosponds to a minimum period (wavelength) of $\lambda = \frac{2}{\Omega}$. Therefore, the above condition may also be written $\Delta x = \frac{A}{N} \leq \frac{1}{\Omega}$

   This means that f needs to be sampled with at least two grid points per period in order for DFT to exactly reproduce the non-zero Fourier coefficients of f.

C.0.3 Case 2: Find number of samples when Ω is known

Assume we have a signal in Fourier domain and we know that the signal for $w \geq \frac{\Omega}{2}$ is very small and can be considered zero. The question is how to find the approximate number of samples to ensure the DFT approximates the Fourier transform coefficients correctly.

Answering to this question is straightforward. According to the explanation in the previous subsection we have $\Delta x \leq \frac{1}{\Omega}$. If we know some information on the upper limit of the spatial function A, then the number of samples should satisfy $N \geq A\Omega$.

Hence, the easiest way to find the number of samples is to find the upper band in Fourier domain and based on that choose sampling grid in spatial (temporal) domain.

Appendix D

Removing Singularity in Numerical Calculations

In this appendix we show how to use a Laurent series to remove the singularity at the origin in equations such as

$$\hat{\mathring{V}}_{\mathrm{e}}(k_r, w, z) = \frac{-\hat{\imath}(w)}{4\pi\sqrt{2\pi}\sqrt{k_r^T \hat{\mathring{\xi}}_{\mathrm{e},z} \hat{\mathring{\xi}}_{\mathrm{e},r} k_r}} \left(e^{-\hat{\mathring{\chi}}(k_r, w)|z|} \right). \tag{D.1}$$

The Laurent series are generalization of a Taylor series, that take into account negative degree in power series expansion.

The Laurent series of a complex function, $f(z)$, around a point c is defined as

$$f(z) = \sum_{n=-\infty}^{\infty} a_n (z-c)^n, \tag{D.2}$$

where the a_n and c are constants, defined by a line integral which is a generalization of Cauchy's integral formula:

$$a_n = \frac{1}{2\pi j} \oint_\gamma \frac{f(z)dz}{(z-c)^{n+1}}. \tag{D.3}$$

The path of integration γ is counterclockwise around a closed, rectifiable path containing no self-intersections, enclosing c and lying in an annulus A in which $f(z)$ is analytic. The expansion for $f(z)$ will then be valid anywhere inside the annulus. The annulus is shown in red in figure D.1, along with an example of a suitable path of integration labeled γ.

In equation (D.1) we are dealing with a removable singularity at the origin for which the analytic solution is known.

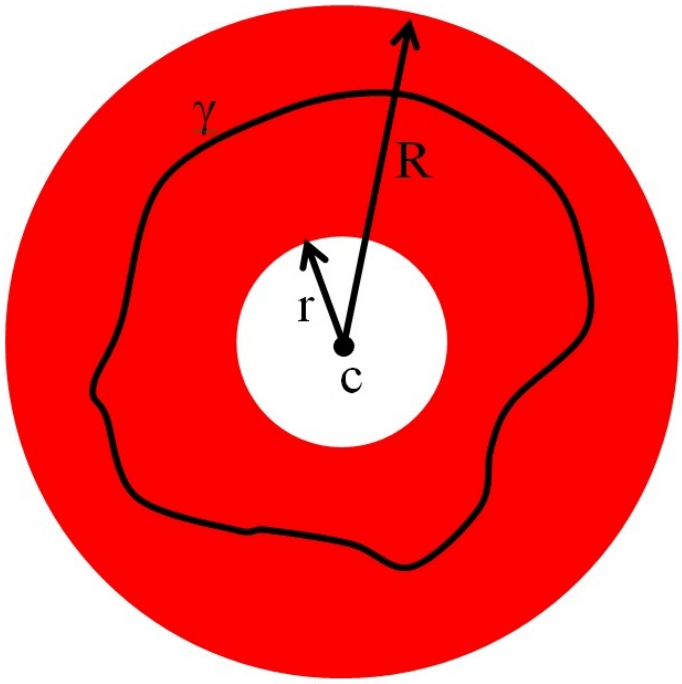

Figure D.1: Integral path for a Laurent series.

We rewrite equation as

$$\check{V}_{\mathrm{e}} = \frac{\alpha_1}{\sqrt{c_2}} \left(e^{-\sqrt{\frac{c_2}{c_1}}|z|} \right), \tag{D.4}$$

where $\alpha_1 = \dfrac{-\iota(t)}{4\pi\sqrt{c_1}}$.

Neglecting α_1 and writing the first 3 terms of the Laurent series in K results in

$$\begin{aligned} \check{V}_{\mathrm{e}} \approx & \frac{1}{\sqrt{\frac{1}{2}\hat{\hat{\xi}}_{\mathrm{e,T}} + \frac{1}{2\rho_i}}\sqrt{k_x^2 + k_y^2}} \\ & - \frac{|z|}{\sqrt{c_1}} + \left[\frac{3\lambda_V^2 (1 - \frac{\lambda_{0I}^2}{\lambda_{0V}^2})}{16\rho_i (\frac{1}{2}\hat{\hat{\xi}}_{\mathrm{e,T}} + \frac{1}{2\rho_i})} + \frac{z^2}{2c_1} \right] \sqrt{k_x^2 + k_y^2}. \end{aligned} \tag{D.5}$$

The far-field (near-field) solution can also be approximated by the Laurent series as

$$\check{V}_{\mathrm{e}}^{\mathrm{ff}} = \frac{\alpha_1}{\sqrt{\left(\frac{1}{2}\hat{\hat{\xi}}_{\mathrm{e,T}} + \frac{1}{2\rho_i}\right)(k_x^2 + k_y^2)}} e^{-\sqrt{\frac{c_2}{c_1}}|z|}. \tag{D.6}$$

The Laurent series for this function will be (disregarding α_1)

$$\begin{aligned}\check{V}_{\mathrm{e}}^{\mathrm{ff}} \approx & \frac{1}{\sqrt{\left(\frac{1}{2}\hat{\hat{\xi}}_{\mathrm{e,T}}+\frac{1}{2\rho_i}\right)\left(k_x^2+k_y^2\right)}}-\frac{|z|}{\sqrt{c_1}} \\ & +\frac{\sqrt{\left(\frac{1}{2}\hat{\hat{\xi}}_{\mathrm{e,T}}+\frac{1}{2\rho_i}\right)\left(k_x^2+k_y^2\right)}}{2c_1}.\end{aligned} \tag{D.7}$$

To remove the singularity at $K=0$, the following function is defined

$$\begin{aligned}\check{V}_{\mathrm{e}}^{\mathrm{rem}} = & \check{V}_e-\check{V}_{\mathrm{e}}^{\mathrm{ff}} \\ = & \frac{3\lambda_V^2\left(1-\frac{\lambda_I^2}{\lambda_V^2}\right)}{4\sqrt{(2)}\rho_i\left(\hat{\hat{\xi}}_{\mathrm{e,T}}+\frac{1}{\rho_i}\right)}\left(k_x^2+k_y^2\right).\end{aligned} \tag{D.8}$$

As we can see, the pole at $K=0$ is now removed in $\check{V}_e^{rem}$. Once we calculate the result of this function numerically, the analytic solution for the far-field region, which is already know, will be added to it to obtain the full solution.

Therefore,

$$V_{\mathrm{e}}(r,t)=\mathcal{F}^{-1}\{\check{V}_{\mathrm{e}}^{\mathrm{rem}}\}-V_{\mathrm{e}}^{\mathrm{ff}}(r,t). \tag{D.9}$$

Appendix E

Gaussian Distribution Calculations

E.1 Three-Dimensional Case

E.1.1 Transformation of equation (3.23) into spherical coordinates

To transform equation (3.23) to spherical coordinates with (r, θ, ϕ) as the radial distance, azimuth and polar angle, we choose

$$x = r \sin\phi \cos\theta, \tag{E.1}$$

$$y = r \sin\phi \sin\theta, \tag{E.2}$$

$$z = r \cos\phi. \tag{E.3}$$

Hence, equation (3.23) is rewritten in spherical coordinates as

$$p(r, \theta, \phi) = \frac{1}{(2\pi)^{\frac{3}{2}} \gamma_r^2 \gamma_z} e^{-r^2 \left(\frac{\sin^2(\phi)}{2\gamma_r^2} - \frac{\cos^2(\phi)}{2\gamma_z^2} \right)}. \tag{E.4}$$

. To map this equation into an ellipsoid an integration over r and θ should be performed

$$p_p(r, \theta, \phi) = \frac{1}{(2\pi)^{\frac{3}{2}} \gamma_r^2 \gamma_z} \int_0^{2\pi} \int_0^{\infty} e^{-r^2 \left(\frac{\sin^2\phi}{2\gamma_r^2} - \frac{\cos^2(\phi)}{2\gamma_z^2} \right)} \sin\phi \, dr \, d\theta. \tag{E.5}$$

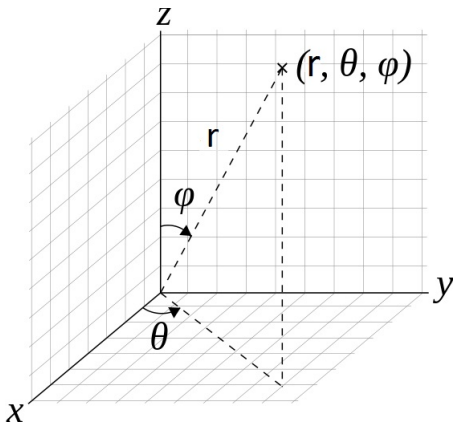

Figure E.1: Spherical coordinates.

Since this function does not have any dependence on θ, we can rewrite it as

$$p_p(r,\phi) = \frac{1}{\sqrt{(2\pi)}\gamma_r^2\gamma_z} \int_0^\infty e^{-r^2\left(\frac{\cos^2(\phi)}{2\gamma_r^2} - \frac{\sin^2(\phi)}{2\gamma_z^2}\right)} \sin\phi \, dr. \tag{E.6}$$

By solving this integration equation (E.7) is given

$$p_p(\phi) = \frac{\eta \sin\phi}{2\varrho^{\frac{3}{2}}(\phi)}, 0 \leq \phi \leq \pi, \tag{E.7}$$

where

$$\begin{aligned} \varrho(\phi) &= \cos^2\phi + \eta^2 \sin^2\phi, \\ \eta &= \frac{\gamma_r}{\gamma_z}. \end{aligned} \tag{E.8}$$

E.1.2 Calculation of the integral in equation (3.30)

To calculate the admittivity kernel in equation (3.30), we expand the integral further and replace the appropriate values from equation (3.11) as follows

$$\begin{aligned} \iint_{\theta,\phi} p_p(\phi) \hat{\nabla}^T \hat{\check{\xi}}_e \hat{\nabla} \, d\theta \, d\phi = &\int_0^\pi \int_0^{2\pi} p_p(\phi) \check{\xi}_{e,T} (K^2 - (\mathbf{k}\cdot\mathbf{u})^2) \, d\theta \, d\phi \\ &- \int_0^\pi \int_0^{2\pi} p_p(\phi) \check{\xi}_{e,L} (\mathbf{k}\cdot\mathbf{u}))^2) \, d\theta \, d\phi, \end{aligned} \tag{E.9}$$

where $\mathring{\hat{\nabla}} = j(\mathbf{k}\cdot\mathbf{u}) = j[k_x, k_y, k_z]^T$, $K = |\mathbf{k}|$, and $\mathbf{u} = [\cos\phi\cos\theta, \cos\phi\sin\theta, \sin\phi]^T$. To simplify the calculations we divide the equation into three different terms c_I , c_{II} and c_{III} which are calculated as follows

$$\begin{aligned} c_I &= \int_0^{\pi}\int_0^{2\pi} p_p(\phi)\check{\xi}_{e,T}K^2\, d\theta\, d\phi \\ &= \check{\xi}_{e,T}K^2\frac{\gamma_z}{\gamma_r}. \end{aligned} \tag{E.10}$$

$$\begin{aligned} c_{II} &= \int_0^{\pi}\int_0^{2\pi} p_p(\phi)\check{\xi}_{e,T}(\mathbf{k}\cdot\mathbf{u}))^2\, d\theta\, d\phi \\ &= \frac{-\xi_{e,T}}{\sqrt{2}\pi\gamma_r^2\gamma_z}\int_0^{\pi}\frac{2\sqrt{2}\pi\sin\phi(\cos^2\phi(k_x^2+k_y^2)+2\sin^2\phi k_z^2)}{(\frac{\cos^2\phi}{\gamma_r^2}+\frac{\sin^2\phi}{\gamma_z^2})^{\frac{3}{2}}}\, d\phi \\ &= \frac{\xi_{e,T}\gamma_z}{2\gamma_r}\times \\ &\left(\frac{\gamma_r^2\gamma_z\tanh^{-1}\left(\frac{\sqrt{\gamma_z^2-\gamma_r^2}}{\gamma_z}\right)\left(2k_z^2-k_x^2-k_y^2\right)+\left((k_x^2+k_y^2)\gamma_r^2-2k_z^2\gamma_z^2\right)\sqrt{\gamma_z^2-\gamma_r^2}}{(\gamma_z^2-\gamma_r^2)^{\frac{3}{2}}}\right). \end{aligned} \tag{E.11}$$

To calculate c_{III} we perform a division first

$$\begin{aligned} c_{III} &= \int_0^{\pi}\int_0^{2\pi} p_p(\phi)\frac{1+jw\tau_m+\lambda_{0J}^2(\mathbf{k}\cdot\mathbf{u})^2}{1+jw\tau_m+\lambda_{0V}^2(\mathbf{k}\cdot\mathbf{u})^2}(\mathbf{k}\cdot\mathbf{u})^2\, d\theta\, d\phi \\ &= \int_0^{\pi}\int_0^{2\pi} p_p(\phi)\times \\ &\left(\frac{\lambda_{0J}^2}{\lambda_{0V}^2}(\mathbf{k}\cdot\mathbf{u})^2+\frac{(1+jw\tau_m)(1-\frac{\lambda_{0J}^2}{\lambda_{0V}^2})}{\lambda_{0V}^2}-\frac{(1+jw\tau_m)^2(1-\frac{\lambda_{0J}^2}{\lambda_{0V}^2})}{\lambda_{0V}^2(1+jw\tau_m+\lambda_{0V}^2(\mathbf{k}\cdot\mathbf{u}))^2)}\right) d\theta\, d\phi, \end{aligned} \tag{E.12}$$

and then calculate the three different terms individually.

$$
\begin{aligned}
c^a_{III} =& \int_0^{\pi}\int_0^{2\pi} p_p(\phi)\left(\frac{\lambda^2_{0J}}{\lambda^2_{0V}}(\mathbf{k}\cdot\mathbf{u}))^2\right) d\theta\, d\phi \\
=& \frac{-\lambda^2_{0J}\gamma_z}{2\lambda^2_{0V}\gamma_r}\times \\
& \left(\frac{\gamma_r^2\gamma_z \tanh^{-1}\left(\frac{\sqrt{\gamma_z^2-\gamma_r^2}}{\gamma_z}\right)\left(2k_z^2-k_x^2-k_y^2\right)+\left((k_x^2+k_y^2)\gamma_r^2-2k_z^2\gamma_z^2\right)\sqrt{\gamma_z^2-\gamma_r^2}}{(\gamma_z^2-\gamma_r^2)^{\frac{3}{2}}}\right),
\end{aligned}
\tag{E.13}
$$

and

$$
\begin{aligned}
c^b_{III} =& \int_0^{\pi}\int_0^{2\pi} p_p(\phi)\left(\frac{(1+jw\tau_m)(1-\frac{\lambda^2_{0J}}{\lambda^2_{0V}})}{\lambda^2_{0V}}\right) d\theta\, d\phi \\
=& \frac{(1+jw\tau_m)(\lambda^2_{0V}-\lambda^2_{0J})\gamma_z}{\lambda^4_{0V}\gamma_r}.
\end{aligned}
\tag{E.14}
$$

The last term in c_{III}

$$
c^{\mathrm{N}}_{III} = \int_0^{\pi}\int_0^{2\pi} p_p(\phi)\left(\frac{(1+jw\tau_m)^2(1-\frac{\lambda^2_{0J}}{\lambda^2_{0V}})}{\lambda^2_{0V}(1+jw\tau_m+\lambda^2_{0V}(\mathbf{k}\cdot\mathbf{u})^2)}\right) d\theta\, d\phi, \tag{E.15}
$$

is a positive function of (θ,ϕ), however the analytical solution cannot be derived using the currently existing tools, methods, and software. Therefore, to continue with the calculations, numerical analysis for this term is used to approximate the value for this function. The numerical results from this function are then combined with the analytical solutions to perform the inverse Fourier transform and obtain the admittivity kernel in the spatial domain. A numerical routine calculates this function numerically along all different combinations of k_x, k_y, and k_z.

Therefore, the resulting full coefficients will be

$$
c_{\mathrm{T}} = c_I + c_{II} + c^a_{III} + c^b_{III} - c^{\mathrm{N}}_{III}. \tag{E.16}
$$

Next we need to compare the relative magnitude of c^{N}_{III} compared to c_{T}. The goal is to find if at any points in k space, the numerical value is larger than the total value. To do this an error array is define as

$$\text{error} = \frac{|c_{\mathrm{N}}|}{|c^{\mathrm{T}}_{III}|}. \tag{E.17}$$

we use the following syntax in Matlab to find the index which might cause problem

$$[D1, D2, D3] = ind2sub(size(error), find(error < 0.1)).$$

The calculations shows that the error is smaller than 0.1 everywhere except at the origin which is around 1.80.

Bibliography

[Altman and Plonsey, 1988] Altman, K. and Plonsey, R. (1988). Development of a model for point source electrical fibre bundle stimulation. *Medical and Biological Engineering and Computing*, 26(5):466–475.

[Alvarez-Maubecin et al., 2000] Alvarez-Maubecin, V., García-Hernández, F., Williams, J. T., and Van Bockstaele, E. J. (2000). Functional coupling between neurons and glia. *The Journal of Neuroscience*, 20(11):4091–4098.

[Anastassiou et al., 2010] Anastassiou, C. A., Montgomery, S. M., Barahona, M., Buzsáki, G., and Koch, C. (2010). The effect of spatially inhomogeneous extracellular electric fields on neurons. *Journal of Neuroscience*, 30(5):1925–1936.

[Bakiri et al., 2011] Bakiri, Y., Káradóttir, R., Cossell, L., and Attwell, D. (2011). Morphological and electrical properties of oligodendrocytes in the white matter of the corpus callosum and cerebellum. *The Journal of physiology*, 589(3):559–573.

[Bear et al., 2015] Bear, M. F., Connors, B. W., and Paradiso, M. A. (2015). *Neuroscience: exploring the brain*, volume 4.

[Benabid, 2003] Benabid, A. L. (2003). Deep brain stimulation for parkinsons disease. *Current opinion in neurobiology*, 13(6):696–706.

[Boinagrov et al., 2010] Boinagrov, D., Loudin, J., and Palanker, D. (2010). Strength–duration relationship for extracellular neural stimulation: numerical and analytical models. *Journal of neurophysiology*, 104(4):2236–2248.

[Borcea, 2002] Borcea, L. (2002). Electrical impedance tomography. *Inverse problems*, 18(6):R99.

[Bossetti et al., 2007] Bossetti, C. A., Birdno, M. J., and Grill, W. M. (2007). Analysis of the quasi-static approximation for calculating potentials generated by neural stimulation. *Journal of neural engineering*, 5(1):44.

[Cartee and Plonsey, 1992] Cartee, L. A. and Plonsey, R. (1992). The transient subthreshold response of spherical and cylindrical cell models to extracellular stimulation. *Biomedical Engineering, IEEE Transactions on*, 39(1):76–85.

[Clark, 2006] Clark, G. (2006). *Cochlear implants: fundamentals and applications*. Springer Science & Business Media.

[Coburn, 1988] Coburn, B. (1988). Neural modeling in electrical stimulation. *Critical reviews in biomedical engineering*, 17(2):133–178.

[Einziger et al., 2005] Einziger, P. D., Livshitz, L. M., and Mizrahi, J. (2005). Generalized cable equation model for myelinated nerve fiber. *IEEE transactions on biomedical engineering*, 52(10):1632–1642.

[Emertrout and Terman, 2009] Emertrout, G. B. and Terman, D. (2009). Mathematical foundations of neuroscience. interdisciplinary applied mathematics, vol. 35.

[Ganapathy and Clark, 1987] Ganapathy, N. and Clark, J. (1987). Extracellular currents and potentials of the active myelinated nerve fiber. *Biophysical journal*, 52(5):749–761.

[Greenberg et al., 1999] Greenberg, R. J., Velte, T. J., Humayun, M. S., Scarlatis, G. N., and De Juan, E. (1999). A computational model of electrical stimulation of the retinal ganglion cell. *IEEE Transactions on Biomedical Engineering*, 46(5):505–514.

[Herculano-Houzel, 2014] Herculano-Houzel, S. (2014). The glia/neuron ratio: how it varies uniformly across brain structures and species and what that means for brain physiology and evolution. *Glia*, 62(9):1377–1391.

[Histed et al., 2009] Histed, M. H., Bonin, V., and Reid, R. C. (2009). Direct activation of sparse, distributed populations of cortical neurons by electrical microstimulation. *Neuron*, 63(4):508–522.

[Hodgkin and Huxley, 1952] Hodgkin, A. L. and Huxley, A. F. (1952). A quantitative description of membrane current and its application to conduction and excitation in nerve. *The Journal of physiology*, 117(4):500.

[Irnich, 1980] Irnich, W. (1980). The chronaxie time and its practical importance. *Pacing and Clinical Electrophysiology*, 3(3):292–301.

[Irnich, 2010] Irnich, W. (2010). The terms chronaxie and rheobase are 100 years old. *Pacing and clinical electrophysiology*, 33(4):491–496.

[Jansen and Rit, 1995] Jansen, B. and Rit, V. (1995). Electroencephalogram and visual evoked potential generation in a mathematical model of coupled cortical columns. *Biological Cybernetics*, 73(4):357–366.

[Joucla et al., 2014] Joucla, S., Glière, A., and Yvert, B. (2014). Current approaches to model extracellular electrical neural microstimulation. *Frontiers in computational neuroscience*, 8:13.

[Joucla and Yvert, 2009] Joucla, S. and Yvert, B. (2009). The mirror estimate: an intuitive predictor of membrane polarization during extracellular stimulation. *Biophysical journal*, 96(9):3495–3508.

[Joucla and Yvert, 2012] Joucla, S. and Yvert, B. (2012). Modeling extracellular electrical neural stimulation: from basic understanding to mea-based applications. *Journal of Physiology-Paris*, 106(3):146–158.

[Kandel et al., 2000] Kandel, E. R., Schwartz, J. H., Jessell, T. M., et al. (2000). *Principles of neural science*, volume 4. McGraw-Hill New York.

[Kasi et al., 2011] Kasi, H., Hasenkamp, W., Cosendai, G., Bertsch, A., and Renaud, P. (2011). Simulation of epiretinal prostheses-evaluation of geometrical factors affecting stimulation thresholds. *Journal of neuroengineering and rehabilitation*, 8(1):1.

[Krassowska and Neu, 1994] Krassowska, W. and Neu, J. C. (1994). Response of a single cell to an external electric field. *Biophysical journal*, 66(6):1768.

[Leuze et al., 2014] Leuze, C. W., Anwander, A., Bazin, P.-L., Dhital, B., Stüber, C., Reimann, K., Geyer, S., and Turner, R. (2014). Layer-specific intracortical connectivity revealed with diffusion mri. *Cerebral Cortex*, 24(2):328–339.

[Loddenkemper et al., 2001] Loddenkemper, T., Pan, A., Neme, S., Baker, K. B., Rezai, A. R., Dinner, D. S., Montgomery Jr, E. B., and Lüders, H. O. (2001). Deep brain stimulation in epilepsy. *Journal of Clinical Neurophysiology*, 18(6):514–532.

[Logothetis et al., 2007] Logothetis, N. K., Kayser, C., and Oeltermann, A. (2007). In vivo measurement of cortical impedance spectrum in monkeys: implications for signal propagation. *Neuron*, 55(5):809–823.

[Martins and Sousa, 2009] Martins, J. C. and Sousa, L. A. (2009). *Bioelectronic vision: retina models, evaluation metrics, and system design*. World Scientific New Jersey.

[McNeal, 1976] McNeal, D. R. (1976). Analysis of a model for excitation of myelinated nerve. *Biomedical Engineering, IEEE Transactions on*, (4):329–337.

[Meffin and Kameneva, 2011] Meffin, H. and Kameneva, T. (2011). The electrotonic length constant: a theoretical estimate for neuroprosthetic electrical stimulation. *Biomedical Signal Processing and Control*, 6(2):105–111.

[Meffin et al., 2012] Meffin, H., Tahayori, B., Grayden, D., and Burkitt, A. (2012). Modeling extracellular electrical stimulation: I. Derivation and interpretation of neurite equations. *Journal of Neural Engineering*, 9(6):065005.

[Meffin et al., 2014] Meffin, H., Tahayori, B., Sergeev, E., Mareels, I., Grayden, D., and Burkitt, A. (2014). Modelling extracellular electrical stimulation: III. derivation and interpretation of neural tissue equations. *Journal of Neural Engineering*, 11(6):065004.

[Milligan and Watkins, 2009] Milligan, E. D. and Watkins, L. R. (2009). Pathological and protective roles of glia in chronic pain. *Nature Reviews Neuroscience*, 10(1):23–36.

[Montgomery Jr, 2010] Montgomery Jr, E. B. (2010). *Deep brain stimulation programming: principles and practice*. Oxford University Press.

[Nelson et al., 2011] Nelson, T. S., Suhr, C. L., Freestone, D. R., Lai, A., Halliday, A. J., McLean, K. J., Burkitt, A. N., and Cook, M. J. (2011). Closed-loop seizure control with very high frequency electrical stimulation at seizure onset in the gaers model of absence epilepsy. *International journal of neural systems*, 21(02):163–173.

[Niparko, 2009] Niparko, J. K. (2009). *Cochlear implants: Principles & practices*. Lippincott Williams & Wilkins.

[Nowak and Bullier, 1996] Nowak, L. G. and Bullier, J. (1996). Spread of stimulating current in the cortical grey matter of rat visual cortex studied on a new in vitro slice preparation. *Journal of neuroscience methods*, 67(2):237–248.

[Okun, 2012] Okun, M. S. (2012). Deep-brain stimulation for parkinson's disease. *New England Journal of Medicine*, 367(16):1529–1538.

[Ozen et al., 2010] Ozen, S., Sirota, A., Belluscio, M. A., Anastassiou, C. A., Stark, E., Koch, C., and Buzsáki, G. (2010). Transcranial electric stimulation entrains cortical neuronal populations in rats. *Journal of Neuroscience*, 30(34):11476–11485.

[Palanker et al., 2005] Palanker, D., Vankov, A., Huie, P., and Baccus, S. (2005). Design of a high-resolution optoelectronic retinal prosthesis. *Journal of neural engineering*, 2(1):S105.

[Pavlin et al., 2002] Pavlin, M., Pavšelj, N., and Miklavčič, D. (2002). Dependence of induced transmembrane potential on cell density, arrangement, and cell position inside a cell system. *Biomedical Engineering, IEEE Transactions on*, 49(6):605–612.

[Pourtaheri et al., 2009] Pourtaheri, N., Ying, W., Kim, J. M., and Henriquez, C. S. (2009). Thresholds for transverse stimulation: fiber bundles in a uniform field. *IEEE Transactions on Neural Systems and Rehabilitation Engineering*, 17(5):478–486.

[Rattay, 1986] Rattay, F. (1986). Analysis of models for external stimulation of axons. *Biomedical Engineering, IEEE Transactions on*, (10):974–977.

[Rattay, 1989] Rattay, F. (1989). Analysis of models for extracellular fiber stimulation. *Biomedical Engineering, IEEE Transactions on*, 36(7):676–682.

[Rattay, 1999] Rattay, F. (1999). The basic mechanism for the electrical stimulation of the nervous system. *Neuroscience*, 89(2):335–346.

[Reilly and Diamant, 2011] Reilly, J. P. and Diamant, A. M. (2011). *Electrostimulation: theory, applications, and computational model*. Artech House.

[Roth, 1991] Roth, B. J. (1991). Action potential propagation in a thick strand of cardiac muscle. *Circulation research*, 68(1):162–173.

[Roth and Wikswo, 1994] Roth, B. J. and Wikswo, J. (1994). Electrical stimulation of cardiac tissue: a bidomain model with active membrane properties. *IEEE Transactions on Biomedical Engineering*, 41(3):232–240.

[Rubinstein and Spelman, 1988] Rubinstein, J. and Spelman, F. (1988). Analytical theory for extracellular electrical stimulation of nerve with focal electrodes. i. passive unmyelinated axon. *Biophysical journal*, 54(6):975.

[Schiff, 2012] Schiff, S. J. (2012). Neural control engineering.

[Schnabel and Struijk, 2001] Schnabel, V. and Struijk, J. J. (2001). Evaluation of the cable model for electrical stimulation of unmyelinated nerve fibers. *Biomedical Engineering, IEEE Transactions on*, 48(9):1027–1033.

[Shepherd et al., 2013] Shepherd, R. K., Shivdasani, M. N., Nayagam, D. A., Williams, C. E., and Blamey, P. J. (2013). Visual prostheses for the blind. *Trends in biotechnology*, 31(10):562–571.

[Tahayori et al., 2012] Tahayori, B., Meffin, H., Dokos, S., Burkitt, A., and Grayden, D. (2012). Modeling extracellular electrical stimulation: II. Computational validation and numerical results. *Journal of Neural Engineering*, 9(6):065006.

[Tahayori et al., 2014] Tahayori, B., Meffin, H., Sergeev, E., Mareels, I., Burkitt, A., and Grayden, D. (2014). Modelling extracellular electrical stimulation: part 4. effect of the

cellular composition of neural tissue on its spatio-temporal filtering properties. *Journal of neural engineering*, 11(6):065005.

[Theodore and Fisher, 2004] Theodore, W. H. and Fisher, R. S. (2004). Brain stimulation for epilepsy. *The Lancet Neurology*, 3(2):111–118.

[Tombran-Tink et al., 2007] Tombran-Tink, J., Barnstable, C. J., and Rizzo, J. F. (2007). *Visual prosthesis and ophthalmic devices: new hope in sight*. Springer Science & Business Media.

[Trachtenberg and Pollen, 1970] Trachtenberg, M. C. and Pollen, D. A. (1970). Neuroglia: biophysical properties and physiologic function. *Science*, 167(3922):1248–1252.

[Tuckwell, 1988] Tuckwell, H. (1988). Introduction to theoretical neurobiology: Linear cable theory and dendritic structure, vol. i of cambridge studies in mathematical biology.

[Tung, 1978] Tung, L. (1978). *A bi-domain model for describing ischemic myocardial dc potentials.* PhD thesis, Massachusetts Institute of Technology.

[Wenger et al., 2011] Wenger, C., Paredes, L., and Rattay, F. (2011). Current-distance relations for microelectrode stimulation of pyramidal cells. *Artificial organs*, 35(3):263–266.

[White and Keller, 1989] White, E. L. and Keller, A. (1989). *Cortical circuits: synaptic organization of the cerebral cortex: structure, function, and theory*. Birkhäuser Boston.

[Wilson and Cowan, 1972] Wilson, H. and Cowan, J. (1972). Excitatory and inhibitory interactions in localized populations of model neurons. *Biophysical Journal*, 12(1):1–24.

[Wongsarnpigoon and Grill, 2012] Wongsarnpigoon, A. and Grill, W. M. (2012). Computer-based model of epidural motor cortex stimulation: effects of electrode position and geometry on activation of cortical neurons. *Clinical Neurophysiology*, 123(1):160–172.

[Ying and Henriquez, 2007] Ying, W. and Henriquez, C. S. (2007). Hybrid finite element method for describing the electrical response of biological cells to applied fields. *IEEE Transactions on Biomedical Engineering*, 54(4):611–620.

[Zetterberg, 1973] Zetterberg, L. (1973). Stochastic activity in a population of neurons. a systems analysis approach.